

Retrospective Theses and Dissertations

1998

Numerical, Image, and Signal Processing Algorithms Applied to Radar Rainfall Estimation

John Eugene Lane
University of Central Florida, john.e.lane@nasa.gov

 Part of the [Electrical and Computer Engineering Commons](#)
Find similar works at: <https://stars.library.ucf.edu/rtd>
University of Central Florida Libraries <http://library.ucf.edu>

This Doctoral Dissertation (Open Access) is brought to you for free and open access by STARS. It has been accepted for inclusion in Retrospective Theses and Dissertations by an authorized administrator of STARS. For more information, please contact STARS@ucf.edu.

STARS Citation

Lane, John Eugene, "Numerical, Image, and Signal Processing Algorithms Applied to Radar Rainfall Estimation" (1998). *Retrospective Theses and Dissertations*. 2439.
<https://stars.library.ucf.edu/rtd/2439>

UNIVERSITY OF CENTRAL FLORIDA LIBRARIES



3 2103 00880 8283

NUMERICAL, IMAGE, AND SIGNAL PROCESSING ALGORITHMS
APPLIED TO RADAR RAINFALL ESTIMATION

By
John Eugene Lane

1998

UCF



NUMERICAL, IMAGE, AND SIGNAL PROCESSING ALGORITHMS APPLIED TO
RADAR RAINFALL ESTIMATION

by

JOHN EUGENE LANE

B.S. Florida Atlantic University, 1975

M.S. Florida Atlantic University, 1977

A dissertation submitted in partial fulfillment of the requirements
for the degree of Doctor of Philosophy in Engineering
in the Department of Electrical and Computer Engineering
in the College of Engineering
at the University of Central Florida
Orlando, Florida

Summer Term
1998

Major Professor: Takis Kasparis

ABSTRACT

Since the advent of radar in the 1940s, it has been well known that water drops composing precipitation scatter microwaves in a predictable manner. This characteristic of early radar has led to the present day Weather Surveillance Radar (WSR-88D) or NEXRAD systems, operated by the National Weather Service (NWS). In parallel to the evolution of weather radar for measuring precipitation over large areas, remote networks of rain gauges have been deployed and managed by agencies such as the Florida Water Management Districts. Since the recent deployment of the NWS network of WSR-88D, as well as the recent launch of the NASA Tropical Rainfall Measurement Mission (TRMM) satellite, significant attention has been placed upon the merging of these diverse sources of rainfall measurement. The main focus of this dissertation research has been to develop and analyze methods of rain gauge and radar correlation for the purpose of optimizing rainfall estimates. The techniques presented in this dissertation observe that the physical link between rain gauge and radar reflectivity data is the drop size distribution (DSD). Using various numerical algorithms, as well as methods common to image and signal processing such as median filtering, two-dimensional cross-correlation, and adaptive signal processing, methods of analysis are presented which attempt to correlate radar reflectivity, rain gauge, and disdrometer data. Particular attention is given to the subjects of rain gauge and radar interpolation; disdrometer calibration; microscale radar rainfall estimation; and a convolution model of DSD evolution, which attempts to model the convective-like properties of rainfall.

ACKNOWLEDGMENTS

Since this dissertation project has relied upon guidance from a number of researchers from agencies at various geographical locations, there are many for which to express gratitude. First of all, I wish to thank my advisor and chairman of my supervisory committee, Dr. Takis Kasparis, for his leadership and encouragement to pursue this project and see it through to completion. Also, I would like to express sincere gratitude to the TRMM/GV PI, Dr. Linwood Jones for providing the resources necessary to conduct this research; Dr. Francis Merceret of NASA/KSC/AMU for contributing invaluable guidance throughout this project; Dr. Greg McFarquhar of NCAR/MMM for his dependable assistance; Dr. James McGuire of the FAU Physics Department for advice and encouragement; Dr. Rick Chapman of APL/JHU for many lengthy discussions; Dr. Garth Hillman of Motorola for providing the means to maintain my employment during this undertaking; and especially to my wife Judy for her remarkable talent at proof-reading. There are many others for which thanks is owed, such as: Peggy Glitto and David Sharp of the Melbourne NWS and Brad Fisher at the NASA TRMM Office, just to name a few.

TABLE OF CONTENTS

1. INTRODUCTION	1
1.1 Adaptive Signal Processing	1
1.1.1 LMS Algorithm	2
1.1.2 Gradient Search Algorithm	3
1.2 Motion Detection in Image Processing	5
1.2.1 Subtraction Method	5
1.2.2 Cross-Correlation Method	6
1.3 Linear Filtering - Convolution	7
1.3.1 Discrete Spatial Convolution	7
1.3.2 Discrete Temporal Convolution	9
1.4 Non-Linear Filtering - Median Filter	10
1.4.1 Conditional Median Filter	12
1.4.2 Gated Median Filter	13
1.5 Spatial Interpolation	14
1.5.1 Bilinear Method	14
1.5.2 The Gravity Formula	15
2. RAINFALL MEASUREMENT INSTRUMENTATION	23
2.1 Background	23
2.2 Rain Gauges	23
2.2.1 Accumulation Gauge	24
2.2.2 Tipping Bucket	24
2.2.3 Optical Rain Gauge	25
2.3 Disdrometer	25
2.3.1 Impact Disdrometer	26
2.3.1.1 Joss Disdrometer	26
2.3.1.2 APL Disdrometer	26
2.3.1.3 UCF Disdrometer	27
2.3.2 Video Disdrometer	28
2.4 Weather Surveillance Radar (WSR-88D)	28
2.4.1 Scan Strategy	29
2.4.2 Z-R Relation	29
2.4.3 Radar Refraction	30

3. RAINDROP DYNAMICS	36
3.1 Background	36
3.2 Drop Size Distribution	36
3.2.1 Exponential Distribution	37
3.2.2 Gamma Distribution	38
3.2.3 Marshall-Palmer Distribution	38
3.3 Raindrop Terminal Velocity	39
3.3.1 Approximation by Gunn (1948)	40
3.3.2 Approximation by Best (1950)	41
3.3.3 Approximation by Atlas (1973)	41
3.4 Moments of the DSD	42
3.4.1 Liquid Water Content	42
3.4.2 Rainfall Rate	43
3.4.3 Radar Reflectivity	43
3.4.4 Z-R Relation	44
4. INTERPOLATION OF RAIN GAUGE AND RADAR DATA	49
4.1 Background	49
4.2 Mathematical Development	50
4.2.1 Conservation Equation	51
4.2.2 Measurement of Advection	52
4.2.2.1 Cross-Correlation of Radar Data	53
4.2.2.2 Triangulation of Rain Gauge Data	55
4.2.3 Interpolation of Radar Data	56
4.2.4 Interpolation of Rain Gauge Data	57
4.2.5 RMS Gauge to Radar Error	58
4.2.6 Gauge Spacing Considerations	59
4.3 Experimental Results	60
4.3.1 Interpolation of Gauge and Radar Rainfall Rates	60
4.3.2 Gauge to Radar Comparisons	61
4.3.2.1 Linear Regression	61
4.3.2.2 RMS Error	64
4.4 Applications and Discussion	66
5. ALGORITHMS FOR PROCESSING DISDROMETER DATA	81
5.1 Background	81

5.2	UCF Acoustic Disdrometer	83
5.3	Calibration	84
5.3.1	Single Drop Calibration	84
5.3.2	Tipping Bucket as a Reference Signal	85
5.3.3	In Situ Calibration of UCF Disdrometer	90
5.4	Suppression of Environmental Noise	93
5.4.1	Impulse Detection Using a Non-Linear Filter	94
5.4.2	Noise Suppression of Thunder Using a Median Filter	98
6.	CONVOLUTION RAINFALL MODEL	113
6.1	Background	113
6.2	Mathematical Development	113
6.2.1	Rainfall Rate Model	116
6.2.2	Radar Reflectivity Model	119
6.3	Simulation of Z Versus R	119
6.3.1	Point Z at Gauge Location	121
6.3.2	Volume Z Over Gauge Location	121
7.	MICROSCALE Z-R ANALYSIS	129
7.1	Background	129
7.2	Mathematical Development	130
7.2.1	The \dot{Z} Model	131
7.2.2	The \dot{z} Model	133
7.3	Experimental Results	136
7.3.1	Predicted Vertical Velocity	136
7.3.2	Measurement of \dot{z}	137
7.4	Discussion of Results	139
7.5	Interpolation of Z and R	141
8.	CONCLUSIONS	151
7.	REFERENCES	156

TABLE OF FIGURES

1-1	Network diagram of the LMS algorithm	16
1-2	Example mean squared error (MSE) surface	16
1-3	Motion detection by subtraction	17
1-4	Motion detection by cross-correlation	18
1-5	Two-dimensional spatial convolution	19
1-6	Spatial convolution filter masks	20
1-7	Second-order temporal convolution filter network	21
1-8	Magnitude response of IIR filters	21
1-9	Common median filter windows	22
1-10	Image restoration with median filter	22
2-1	Accumulation rain gauge	31
2-2	Tipping bucket rain gauge	31
2-3	Schematic diagram of the RD69 (Distromet, Ltd)	32
2-4	Schematic diagram of the APL disdrometer	33
2-5	Four UCF low-cost acoustic disdrometers (ARGA sensors)	34
2-6	NWS NEXRAD hybrid scan strategy for rainfall estimation	34
2-7	Example Melbourne NEXRAD derived product reflectivity data	35
3-1	Solid lines are plots of the MP DSD	45
3-2	Symbols are experimental data of drop velocity versus fall height	46
3-3	High-speed photographs of falling raindrops	47
3-4	Wind tunnel simulations of falling raindrops at terminal velocity	48
4-1	Determination of advection velocity u from adjacent gauges	68
4-2	Three adjacent gauges showing delay time	68
4-3	Map of TRMM/KSC gauge test site	69
4-4	TRMM/KSC rain gauge and Melbourne NEXRAD interpolated data	70
4-5a	Interpolated radar rainfall, based on Melbourne NEXRAD data	71
4-5b	Interpolated gauge rainfall, based on TRMM rain gauge data	72
4-6	Linear regression of $\log Z$ versus $\log R$ of interpolated data	73
4-7	TRMM/KSC gauge site 017, June 4, 1997	74
4-8	TRMM/KSC gauge site 018, June 4, 1997	75
4-9	TRMM/KSC gauge site 020, June 4, 1997	76
4-10	RMS error functions and corresponding Z - R parameter solutions	77

4-11	Comparisons of RMS error minimums	78
4-12a	Spatially interpolated rainfall rate from a single gauge	79
4-12b	Spatially interpolated rainfall rate from a single gauge	80
5-1	Schematic diagram of acoustic sensor	100
5-2	Sampled output of acoustic sensor	100
5-3	Block diagram of acoustic sensor's digital signal processing section	101
5-4a	Synthetic drop production apparatus	102
5-4b	Small drop generator actively knocks drops off the tip	102
5-5a	Relationship between inner diameter tube size and drop diameter	103
5-5b	Relationship between audio speaker frequency and drop diameter	103
5-6	Block diagram of adaptive DSP calibration algorithm	104
5-7	$V(n)$ (open circles) and $\hat{V}(n)$ (solid squares) versus $t(n)$	105
5-8	Calibration curves for three acoustic	106
5-9	D/t plots for (a) sensor B, (b) sensor C, and (c) sensor D	107
5-10	Rainfall rate versus $t(n)$ with $\Delta t = 6$ s	108
5-11	Various rainfall rate drop size distributions $N(D)$	109
5-12	Block diagram of adaptive scratch filter	110
5-13	Processing of ARGA disdrometer data by adaptive scratch filter	110
5-14	ARGA disdrometer data processed by previous linear filter	111
5-15	Same data shown in Figures 5-14, but processed by non-linear filter	112
6-1	Calculated rainfall at gauge site x_G based on convolution of DSD	123
6-2	Volume integration for radar reflectivity calculation	124
6-3	Simulated point Z-R at $x_G = 4$ km	125
6-4	Simulated point Z-R at $x_G = 6$ km	125
6-5	Simulated point Z-R at $x_G = 8$ km	126
6-6	Simulated point Z-R at $x_G = 10$ km	126
6-7	Simulated volume Z-R at $x_G = 4$ km	127
6-8	Simulated volume Z-R at $x_G = 6$ km	127
6-9	Simulated volume Z-R at $x_G = 8$ km	128
6-10	Simulated volume Z-R at $x_G = 10$ km	128
7-1	\dot{Z} model, $R = R(Z, \dot{Z})$, with $H=3000$ m	143
7-2	\dot{z} model, $R = R(Z, f(\dot{z}))$	144
7-3	Map of rain gauge test site and Melbourne radar	145

7-4	Melbourne NEXRAD base scan reflectivity over rain gauge test site	146
7-5	Dotted line is spatially interpolated radar rainfall	147
7-6	Predicted average vertical velocity W over rain gauge test site	147
7-7	Interpolated reflectivity as a function of time above gauge array	148
7-8a	Height of 30 dBZ level as a function of time for \vec{r}^- and \vec{r}^+	149
7-8b	Re-sampled and smoothed height, filling in missing points	149
7-9	Vertical velocity of 30 dBz level above local gauge point	150
7-10	Dotted line is average vertical velocity of 30 dBZ level	150

LIST OF TABLES

1-1	Convolution coefficients for IIR filter network	10
4-1	Z-R parameters based on standard linear regression	63
4-2	Z-R parameters based on linear regression	63
4-3	Z-R parameters based on RMS error surfaces	64
4-4	Z-R parameters based on RMS error surface minimums	65
4-5	Comparison of RMS error surface minimum values and Z-R parameters ...	65
5-1	Parameters using Equations (5.3) and (5.4), as shown in Figure 5-8	92
6-1	Convolution model (CR) example simulation parameters	120
7-1	NEXRAD beam center height at S = 21 km	139

CHAPTER 1

INTRODUCTION

The field of image and digital signal processing (DSP) has evolved at an exponential rate over the last few decades, primarily due to advances in computer technology. However, without advances in numerical and computational algorithms, topics which are fundamentally mathematical in nature, this relatively new field of electronics might not exist today. Many DSP and image processing algorithms were borrowed from other unrelated fields of engineering, as well as science, economics, and business. Since the field of DSP and image processing has had several decades to evolve independently, it is now useful to explore how some of these algorithms and numerical techniques can be utilized in other unrelated endeavors of engineering and science.

It is the goal of this dissertation research to borrow some of the common, as well as uncommon, DSP and image processing algorithms and to apply them, with appropriate modification, to selected problems involving radar meteorology, hydrology, and atmospheric science. The general problem that will be considered is rainfall estimation by means of weather surveillance radar. Several signal processing algorithms and techniques will be considered, adapted, and applied to this problem. The results of this work will be presented in the sections to follow.

1.1 Adaptive Signal Processing

Algorithms which recursively transform one state of a system into another state, such that after some length of time, a specific final state is reached regardless of the initial

state, can usually be designated as adaptive algorithms. These algorithms are closely related to *optimization* or *function minimization*^[1] problems where the goal is to find a function's global minimum in multi-dimensional parameter space. Adaptive algorithms are usually associated with *real-time* processing, as opposed to general optimization methods which are usually performed by means of *off-line* processing. However, even though this distinction may be a common characteristic, it does not necessarily suffice as a true definition. A better definition perhaps is to simply say that adaptive algorithms are a subset of general numerical optimization methods and are usually processed in real-time. The concepts discussed in this section will be utilized in Chapter 5 for developing an algorithm for calibrating a disdrometer.

1.1.1 LMS Algorithm

The *least mean square* (LMS) class of algorithms used in digital signal processing, are among the most commonly used DSP algorithms in existence today. Proposed in the mid 1970's by Bernard Widrow and associates^[2], this computationally intensive numerical technique became practical and affordable with the recent advent of low-cost programmable DSP devices such as the Motorola DSP56303.

A typical application of the LMS algorithm for system identification (system modeling), as shown in Figure 1-1, adapts a *finite response filter* (FIR) whose output $y(n)$ is subtracted from the input signal $d(n)$ to create an output error signal $e(n)$:

$$e(n) = d(n) - \sum_{k=0}^{N-1} w_k(n) x(n-k) \quad (1.1)$$

where $x(n)$ is the reference signal, $x(n-k)$ are the N filter states, and $w_k(n)$ are the N filter coefficients. If $d(n)$ is correlated to $x(n)$, then the error signal $e(n)$ should tend towards zero. This situation describes, for example, a speakerphone where $x(n)$ is the signal received from the telephone network (receive signal from the remote party); $d(n)$

is the local acoustic signal reflected from the speakerphone's amplifier/speaker, through the room and back to the microphone; and $e(n)$ is the outgoing transmitted telephone signal. In this case, $d(n)$ is correlated to $x(n)$ since $d(n)$ is a linear time-invariant (LTI) version of $x(n)$ formed by the acoustic transfer function of the speaker-room-microphone system. The LMS algorithm adapts the FIR filter coefficients in a recursive manner so that the filter output $y(n)$ approximates the input signal $d(n)$. The algorithm which updates the FIR coefficients so that $y(n)$ closely follows $d(n)$, is the LMS algorithm:

$$w_k(n+1) = w_k(n) + 2\mu e(n) x(n-k) \quad (1.2)$$

where $w_k(n)$ are the coefficients at the k th tap of the FIR filter at the current sample time n and μ is the convergence constant or gain factor. The new k th coefficients $w_k(n+1)$, will be used during the next sample time by the FIR filter. The $x(n-k)$ are the input values at the tap outputs as shown in Figure 1-1. The LMS algorithm is a special case, using the delayed tap-line configuration and real-time recursive tap updates, of the general *gradient search* method.

1.1.2 Gradient Search Algorithm

Determining the coefficients w_0 and w_1 of a straight line fit $y = w_0 + w_1 x$ to a set of N data points (x_k, y_k) , is referred to as *linear regression*. This curve fitting procedure is the result of minimizing the χ^2 error defined as:

$$\chi^2(w_0, w_1) = \sum_{k=1}^N (y_k - w_0 - w_1 x_k)^2 \quad (1.3a)$$

or the corresponding RMS error, as shown in Figure 1-2:

$$RMS = \sqrt{\frac{\chi^2(w_0, w_1)}{N}} \quad (1.3b)$$

An exact solution W^* for the minimum of Equation (1.3a) or (1.3b) can be found by evaluating the gradient of χ^2 and setting it to zero.

In parameter space of dimensions higher than two, a similar procedure can be used to find an exact solution W^* for the RMS minimum, as long as the fitting function is a polynomial in x . Otherwise, the issue involves finding the solution to a non-linear problem for which an exact analytical solution will probably not exist. Again in this case, the minimum of an RMS error surface W^* is the solution to the problem (finding the solution will require an iterative search procedure):

$$\chi^2(\mathbf{w}) = \sum_{k=1}^N (y_k - y(\mathbf{w}))^2 \quad (1.4)$$

where $\mathbf{w} \equiv [w_0, w_1, \dots, w_N]$. The N parameters w_0, w_1, \dots, w_N are the coordinates of an N -dimensional error surface defined by Equations (1.4). Using a gradient search algorithm, such as the *steepest descent* method, an approximately optimized set of parameters can be found by recursively evaluating Equation (1.5):

$$\mathbf{w}(n+1) = \mathbf{w}(n) - \mu \nabla \chi^2(\mathbf{w}) \quad (1.5)$$

$$\nabla \equiv \begin{bmatrix} \frac{\partial}{\partial w_0} \\ \frac{\partial}{\partial w_1} \\ \vdots \\ \frac{\partial}{\partial w_N} \end{bmatrix} \quad (1.6)$$

where μ is the convergence constant. Comparing Equation (1.5) with the LMS algorithm of Equation (1.2), it can be seen that in the LMS problem, the product term $2e(n)x(n-k)$ is comparable to the k th component of the gradient as defined by Equation (1.6).

1.2 Motion Detection in Image Processing

A digital gray-scale image is an array of *pixel* values which may be denoted by $x_k(n_1, n_2)$, where n_1 and n_2 are the pixel (array) indices in the horizontal and vertical directions, respectively, usually starting from the bottom left corner of the frame. In most gray-scale images, the value of $x_k(n_1, n_2)$ is quantized to 8 bits with 256 shades of gray, where a value of 0 represents black and a value of 255 is equal to white. In order to estimate the motion velocity vector \mathbf{u} of an object in the image, the displacement vector between consecutive k and $k+1$ image frames, divided by the time interval between frames, must be measured. (For simplicity of general discussion in the following sections, the time period between consecutive frames are assumed to be one so that the displacement vector is always equal to the velocity vector \mathbf{u}). Applications of motion detection and estimation will be utilized in Chapter 4 for measuring the advection velocity of a cell or cluster of precipitation cells contained in a weather radar image.

1.2.1 Subtraction Method

The simplest method of detecting and measuring the direction of motion of objects within consecutive gray-scale image frames $x_k(n_1, n_2)$ and $x_{k+1}(n_1, n_2)$, is to simply subtract the two frames (see Figure 1-3) forming a *difference* image:

$$d_y(n_1, n_2) \equiv |x_{k+1}(n_1 - i, n_2 - j) - x_k(n_1, n_2)| \quad (1.7a)$$

where i and j are displacements which attempt to *minimize* the sum of all pixels in the difference image:

$$D_y \equiv \sum_{n_1} \sum_{n_2} d_y(n_1, n_2) \quad (1.7b)$$

Figure 1-3a shows an example of motion detection. In Figure 1-3b, the direction of motion is estimated by searching for a minimum in D_{ij} corresponding to the displacement vector $\mathbf{u} \equiv (i, j) = (1, 0)$ for this particular example.

It should be noted that in order for motion detection algorithms to perform properly, the total time derivative of change of objects within the image must be relatively small between consecutive image frames. For applications in radar meteorology, this would correspond to the relation between rate of change (growth and decay) of precipitation cells as compared to the scan time (sampling period) between radar images. Since the National Weather Service radar scan time is fixed to about 5 min, some convective storm cells can evolve at very fast rates, making it difficult to estimate the spatial displacement and advection velocity (displacement divided by scan time).

1.2.2 Cross-Correlation Method

One problem with the difference method described in the previous section, is that a difference is essentially a derivative and it is well known that derivatives can be adversely sensitive to noise. The *cross-correlation* method, as shown in Figure 1-4, alleviates some of these problems at the expense of an increased number of numerical computations:

$$r_{ij}(n_1, n_2) \equiv x_{k+1}(n_1 - i, n_2 - j) \cdot x_k(n_1, n_2) \quad (1.8a)$$

where i and j are displacements which attempt to *maximize* the sum of all pixels in the product image:

$$R_{ij} \equiv \sum_{n_1} \sum_{n_2} r_{ij}(n_1, n_2) \quad (1.8b)$$

Figures 1-4 show an example of motion estimation, where the direction of motion is found by searching for a maximum in R_{ij} , again corresponding to the displacement vector $\mathbf{u} \equiv (i, j) = (1, 0)$ for this example.

1.3 Linear Filtering - Convolution

If $f_1(x)$ and $f_2(x)$ are two arbitrary functions, the continuous domain (as opposed to discrete domain) *convolution* of these two functions is defined as:

$$g(x) = \int_{-\infty}^{\infty} f_1(y) f_2(x - y) dy \quad (1.9a)$$

The Fourier transform of the convolution is:

$$F[g(x)] = F[f_1(x)] F[f_2(x)] \quad (1.9b)$$

Equations 1.9 state that the Fourier transform of a convolution is equivalent to the product of the Fourier transforms of the factors of the convolution. The discrete version of convolution has a profound impact on practical applications of image and digital signal processing. Using the concepts presented in this section, a *convolution model of rainfall*, based on spatial and temporal convolution and atmospheric advection, will be discussed in Chapter 6.

1.3.1 Discrete Spatial Convolution

A common type of two-dimensional spatial filtering is defined where each pixel is replaced by a linear combination of its surrounding pixels. As shown in Figure 1-5^[3] masks of certain size and shape define the region from which pixels are used in this linear combination. Since this operation is essentially a convolution, these masks are often referred to as *convolution masks*. Since the convolution mask is essentially the impulse

response of the filter, it is apparent that this corresponds to a linear FIR type of filtering. Spatial linear filters are equivalent to transform domain filters. In the case of convolution masks, the frequency response can be obtained from the two-dimensional Fourier transform of the mask given by:

$$H(\omega_x, \omega_y) = \sum_{n=-N}^N \sum_{m=-M}^M h(n, m) e^{-i(n\omega_x + m\omega_y)} \quad (1.10)$$

where $2N+1$ is the length of the mask in the x direction, $2M+1$ is the length in the y direction, and $h(n, m)$ are the mask coefficients.

One popular image processing filter for noise suppression is the averaging or *lowpass* filter. This filter replaces each pixel with the average (or mean) value of the pixels in the filter mask. The left side of Figure 1-6a shows the 3×3 convolution mask of a mean or lowpass filter, where the averaging operation smoothes an image. The right side of Figure 1-6a displays the equivalent frequency response of the 3×3 lowpass filter. The DC gain of the filter is unity, which means that the average brightness of a filtered image will be preserved. The mean filter is also effective in suppressing Gaussian noise (grainy appearance) from images, but the blurring introduced by the filter can be a problem.

Figure 1-6b shows the mask and equivalent frequency response of a 3×3 *highpass* filter formed by subtracting the mean filter mask from an identity (unity) mask. Highpass filters are useful for sharpening edges of an object in an image. In the extreme case, highpass filters can be used to suppress most of the image information except for the edges, which is useful in applications where object outlines are important such as robotic vision applications.

1.3.2 Discrete Temporal Convolution

As an example of temporal convolution, a filter network based on a second-order infinite impulse response (IIR) structure, is shown in Figure 1-7. The filter control parameters are represented by f_c and d (or f_o and Q), which are the *cutoff frequency* and *damping factor* for a lowpass or highpass filter (or *center frequency* and *quality factor* for a bandpass or bandstop filter). The discrete time convolution filter from the network of Figure 1-7 is implemented using the recursive difference equation:

$$y(n) = 2 [\alpha x(n) + \alpha_1 x(n-1) + \alpha_2 x(n-2) + \gamma y(n-1) - \beta y(n-2)] \quad (1.11)$$

where the parametric form of the filter coefficients^[4,5], as shown in Table 1-1, are given as a function of the filter control parameters f_c and d (or f_o and Q), and the normalized center frequency is $\theta_0 = 2\pi f_0 / f_s$. Note that in the lowpass and highpass cases, the damping factor d is typically set equal to $\sqrt{2}$ for a *maximally flat* response.

The filter input states are $x(n-k)$ and the $y(n-k)$ are the filter output states. The frequency response of the difference formula of Equation (1.11) is:

$$H(\theta) = \frac{\alpha + \alpha_1 e^{-i\theta} + \alpha_2 e^{-i2\theta}}{\frac{1}{2} - \gamma e^{-i\theta} + \beta e^{-i2\theta}} \quad (1.12)$$

where $\theta = 2\pi f / f_s$ is the normalized frequency and f_s is the sample frequency. Frequency response plots of the bandpass and bandstop configurations are shown in Figures 1-8, using the magnitude of the frequency response $|H(\theta)|$ from Equation (1.12).

Table 1-1. Convolution coefficients for IIR filter network of Figure 1-7.

coefficient	Lowpass	Highpass	Bandpass	Bandstop
α	$\frac{1}{4}(\frac{1}{2} + \beta - \gamma)$	$\frac{1}{4}(\frac{1}{2} + \beta + \gamma)$	$\frac{1}{2}(\frac{1}{2} - \beta)$	$\frac{1}{2}(\frac{1}{2} + \beta)$
α_1	2α	-2α	0	$-\gamma$
α_2	α	α	$-\alpha$	α
β	$\frac{1}{2} \cdot \frac{1 - \frac{d}{2} \sin \theta_c}{1 + \frac{d}{2} \sin \theta_c}$	$\frac{1}{2} \cdot \frac{1 - \frac{d}{2} \sin \theta_c}{1 + \frac{d}{2} \sin \theta_c}$	$\frac{1}{2} \cdot \frac{1 - \tan\left(\frac{\theta_0}{2Q}\right)}{1 + \tan\left(\frac{\theta_0}{2Q}\right)}$	$\frac{1}{2} \cdot \frac{1 - \tan\left(\frac{\theta_0}{2Q}\right)}{1 + \tan\left(\frac{\theta_0}{2Q}\right)}$
γ	$(\frac{1}{2} + \beta)\cos\theta_c$	$(\frac{1}{2} + \beta)\cos\theta_c$	$(\frac{1}{2} + \beta)\cos\theta_0$	$(\frac{1}{2} + \beta)\cos\theta_0$

1.4 Non-Linear Filtering - Median Filter

Among the many types of non-linear filters, *rank* or *order statistics* filters are among the most popular, and of these, the *median filter* is probably the most common. A very desirable property of these filters in image processing applications, not achievable by conventional linear filters, is the ability to suppress *impulsive* (salt and pepper) noise while preserving sharp signal transitions. In radar meteorology, median filters can be used to efficiently suppress anomalous propagation (AP) noise^[6]. AP is impulsive in nature and can significantly degrade rainfall estimation from weather radar images contaminated by this kind of noise.

If N variables x_1, x_2, \dots, x_N are arranged in ascending order of magnitude $x_{(1)} \leq x_{(2)}, \dots, \leq x_{(N)}$, then $x_{(k)}$ is the *order statistic* of rank k . If $N = 2n + 1$, then the order statistic of rank n (at the center of the sorted list) is the median value of the list:

$$\text{med}\{x_i\} \equiv x_{(n)} \quad (1.13)$$

A *rank filter* scans the input signal with a window and replaces the central sample with an order statistic of the enclosed samples. In the special case, when the order statistic is the median, then this rank filter is called the median filter (MF). Among rank filters, the MF is the only type that will not distort monotonically increasing or decreasing signal slopes. Since a sharp edge (step) is monotonic in a region around the edge, it will be preserved as well. Other rank filters generally preserve edges, but shift the location of the transition. The two extremes of rank filters, namely the *minimum* and *maximum* filters, are important in the implementation of another major class of non-linear filters, referred to as *morphological filters*. Another important property of the MF is that any impulse (positive or negative) in the input signal that is narrower than $(N-1)/2$ samples, will be suppressed and replaced by the median of the window. This property makes the MF an ideal filter for the suppression of impulsive noise. However, the MF is not very effective in suppressing other types of non-impulsive noise such as Gaussian noise, in which case the conventional linear filters are better suited.

Median filtering can be performed on both one-dimensional or two-dimensional signals. In two-dimensional filtering, the filter window has a specific size and shape. Among the numerous useful shapes, the most popular are the *square* and *cross* shaped windows, shown in Figures 1-9. Theoretically it can be proven that if the two-dimensional median window shape is symmetric around a central point, and the central point is also included in the median computation, then the filter will preserve edges. The edge preservation property is valuable in image processing applications since edges are predominant image characteristics. As discussed previously, a mean filter will always smear edges due to the attenuation of the high frequency components. Depending on the window shape, certain other image features may or may not be preserved by the MF. For example, thin lines in the image can be mistaken as impulses and be suppressed. Also,

rectangular windows are known to clip corners, whereas cross shaped windows preserve them. However, cross shaped windows cannot suppress as much noise as the rectangular, unless the size of the cross is rather large. Using large crosses, on the other hand, has the disadvantage that pixels distant to the central pixel will be used in the median computation, and therefore the strong local correlation of pixel values is not fully utilized. In general, the best choice of the window shape for a particular application is somewhat ad-hoc. Concepts of median filtering discussed in this section, will be utilized in suppressing environmental noise from the acoustic signal of the UCF impact disdrometer, to be discussed in Chapter 5.

1.4.1 Conditional Median Filter

When filtering of *salt and pepper* noise is desired, the *conditional median filter*^[7] (CMF) developed at the University of Central Florida, offers a much better solution by adaptively varying the amount of filtering depending on the amount of impulsive noise. The primary advantage of the CMF is that it can suppress impulsive noise while preserving most of the image detail. Since it will minimally degrade noise-free images, the CMF is suitable in applications where the amount of impulsive noise in the image is not known, such as AP noise in weather radar images. The CMF is based on the condition that noise impulses should differ significantly from the local background. At each pixel, this condition is checked to determine whether the pixel should be replaced by the median. With the window centered at the pixel $x(i, j)$, the CMF output $y(i, j)$ is either the median $m(i, j)$ or the input sample $x(i, j)$, according to the following equation (assuming 8 bits/pixel):

$$y(i, j) = \begin{cases} x(i, j) & \frac{m(i, j)}{2} < x(i, j) < \frac{m(i, j) + 255}{2} \\ m(i, j) & \text{otherwise} \end{cases} \quad (1.14)$$

The CMF will selectively eliminate impulses based on both the relative width as compared to the window size, and the relative amplitude as compared to the local background. Figure 1-10b presents the output of a CMF with a 5 x 5 window, applied on the noisy image of Figure 1-10a. The CMF performs best at suppressing salt and pepper noise, while maintaining the fine image detail.

1.4.2 Gated Median Filter

The *gated median filter*^[8] (GMF) is a modification of the CMF algorithm where an independent detector first locates impulses, then gates a conventional MF on and off. The MF is normally disabled (bypassed), except in those signal regions where impulses have been detected:

$$y(n) = \begin{cases} m(n) & g(n) > 0 \\ x(n) & \text{otherwise} \end{cases} \quad (1.15a)$$

where:

$$m(n) = \text{med}\{x(n-k), \dots, x(n), \dots, x(n+k)\} \quad (1.15b)$$

is the median value over a window of length $N = 2k + 1$ samples. $x(n)$ and $y(n)$ are the input and output sequences and $g(n)$ is a gating signal which is provided with the correct timing so that the MF is activated when impulses are within the filter window. This type of MF preserves the signal, except where impulses are detected. The disadvantage of the GMF over other types of median filters is that two separate steps are required, detection and filtering. However, in one-dimensional signal processing applications, such as suppression of environmental noise associated with the impact disdrometer, the GMF may be the best choice.

1.5 Spatial Interpolation

The topic of this section deviates somewhat from the previously discussed image and signal processing algorithms. In general, interpolation may encompass a variety of applications, including some main stream DSP topics such as sample rate conversion, linear prediction, and other related subjects. The application to be discussed in this section is more closely related to mapping and associated numerical algorithms for performing spatial interpolation of data over a two-dimensional surface. Two types of interpolation methods will be considered: the *bilinear* method, which requires that data be on a uniform rectangular grid; and the *gravity*^[9] method which does not require a grid. These techniques will be utilized in Chapter 4 for creating rainfall rate maps from rain gauge and weather radar data.

1.5.1 Bilinear Method

The bilinear method is the two-dimensional extension of simple one-dimensional linear interpolation. The basic bilinear method requires that the original data is on a uniform rectangular grid of spacing Δx in the x direction and Δy in the y direction. Every grid point consists of a set of data points, $\{x_j, y_k, z(j,k)\}$, where $z(j,k) \equiv z(x_j, y_k)$ is the functional value (for example, radar reflectivity) at the (j,k) grid point. For every rectangle consisting of the four adjacent grid points $\{x_j, y_k, z(j,k)\}$, $\{x_{j+1}, y_k, z(j+1,k)\}$, $\{x_j, y_{k+1}, z(j,k+1)\}$, and $\{x_{j+1}, y_{k+1}, z(j+1,k+1)\}$, a two-dimensional linear interpolation for an arbitrary point $z(x,y)$ bounded by the grid is given by the bilinear formula:

$$\begin{aligned}
z(x, y) = & \left[(x_{j+1} - x)(y_{k+1} - y) z(j, k) \right. \\
& + (x - x_j)(y_{k+1} - y) z(j+1, k) \\
& + (x_{j+1} - x)(y - y_k) z(j, k+1) \\
& \left. + (x - x_j)(y - y_k) z(j+1, k+1) \right] (\Delta x \Delta y)^{-1}
\end{aligned} \tag{1.16}$$

for $x_j \leq x \leq x_{j+1}$ and $y_k \leq y \leq y_{k+1}$, where $\Delta x = x_{j+1} - x_j$ and $\Delta y = y_{k+1} - y_k$.

1.5.2 The Gravity Formula

In Shepard's formula (or gravity formula), the requirement of the rectangular grid spacing is eliminated. For N set of data points $\{x_i, y_i, z_i\}$, the interpolation for an arbitrary point $z(x, y)$ is:

$$z(x, y) = \frac{\sum_{i=1}^N z_i \left((x - x_i)^2 + (y - y_i)^2 \right)^{-q}}{\sum_{i=1}^N \left((x - x_i)^2 + (y - y_i)^2 \right)^{-q}} \tag{1.17}$$

where q is a free parameter. For $q = 1$, each term of the denominator $[(x - x_i)^2 + (y - y_i)^2]^{-1}$ is equivalent to the inverse of the distance from the interpolation point (x, y) to the data point (x_i, y_i) .

Equation (1.17) is an extremely simple method of two-dimensional interpolation, and has continuous derivatives through out the interpolation region. However, one disadvantage of this method is that the derivatives are zero at all data points (x_i, y_i) . The parameter q controls how fast the derivative goes to zero when approaching the (x_i, y_i) data point. Shepard devised methods^[9] for avoiding some of the disadvantages of Equation (1.17) at the expense of added complexity.

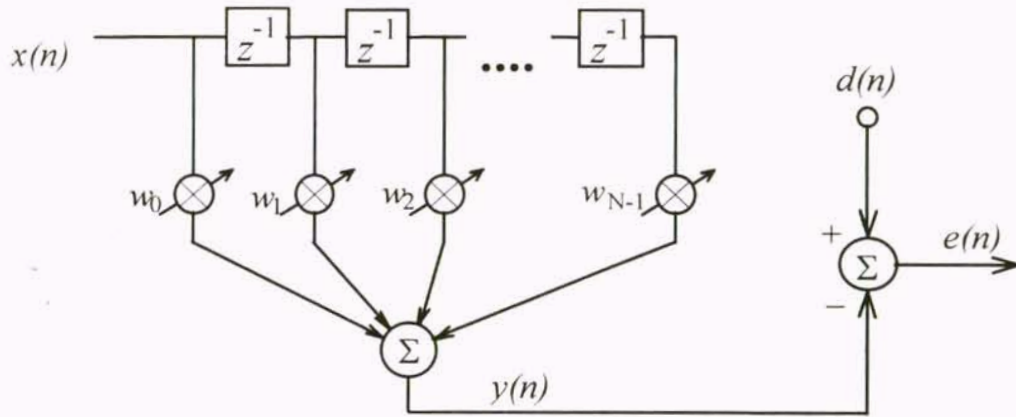


Figure 1-1. Network diagram of the *LMS algorithm*, for one-dimensional signals. $x(n)$ is the reference signal, $d(n)$ is the input signal, $e(n)$ is the error output signal, and $y(n)$ is the LMS approximation of $x(n)$. The filter coefficients are $w(k)$, while the filter states are $x(n-k)$.

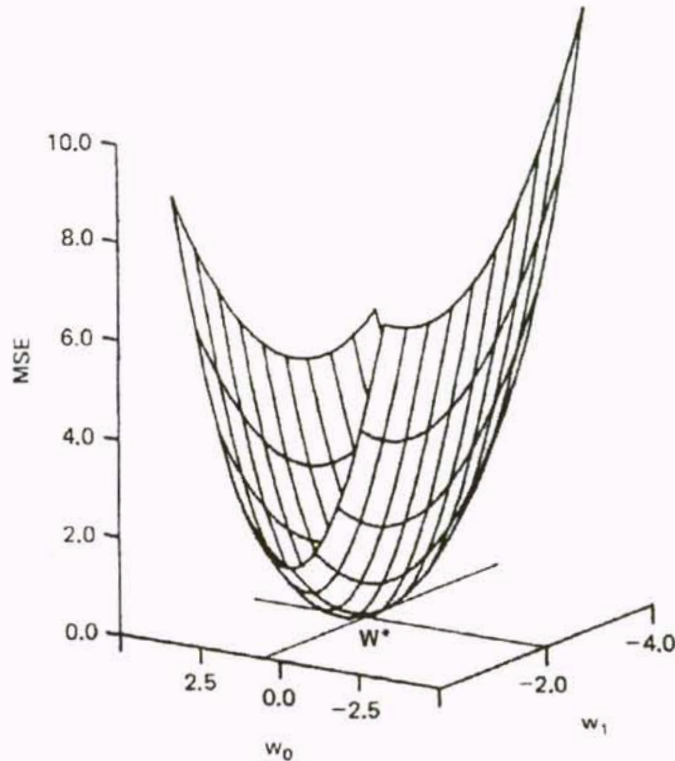


Figure 1-2. Example mean squared error (MSE) surface traversed by *gradient search algorithm*. Solution is the surface minimum at W^* . Figure from Widrow (1985).

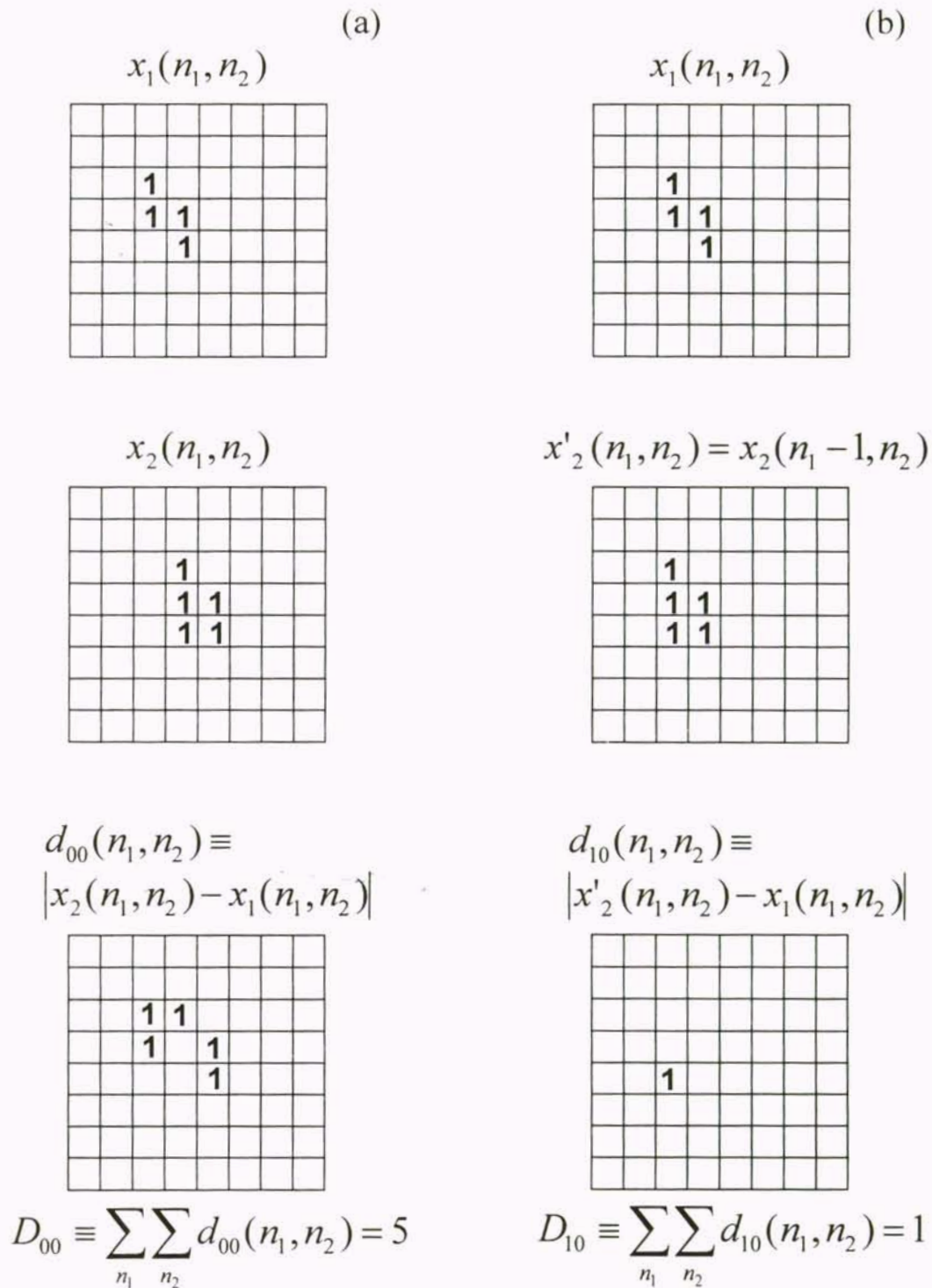


Figure 1-3. Motion detection by subtraction where a *minimum* in D_{ij} determines the value of displacement $\mathbf{u} \equiv (i, j)$ between consecutive images $x_1(n_1, n_2)$ and $x_2(n_1, n_2)$; (a) $\mathbf{u} = (0, 0)$ where $D_{00} = 5$, (b) $\mathbf{u} = (1, 0)$ where $D_{10} = 1$.

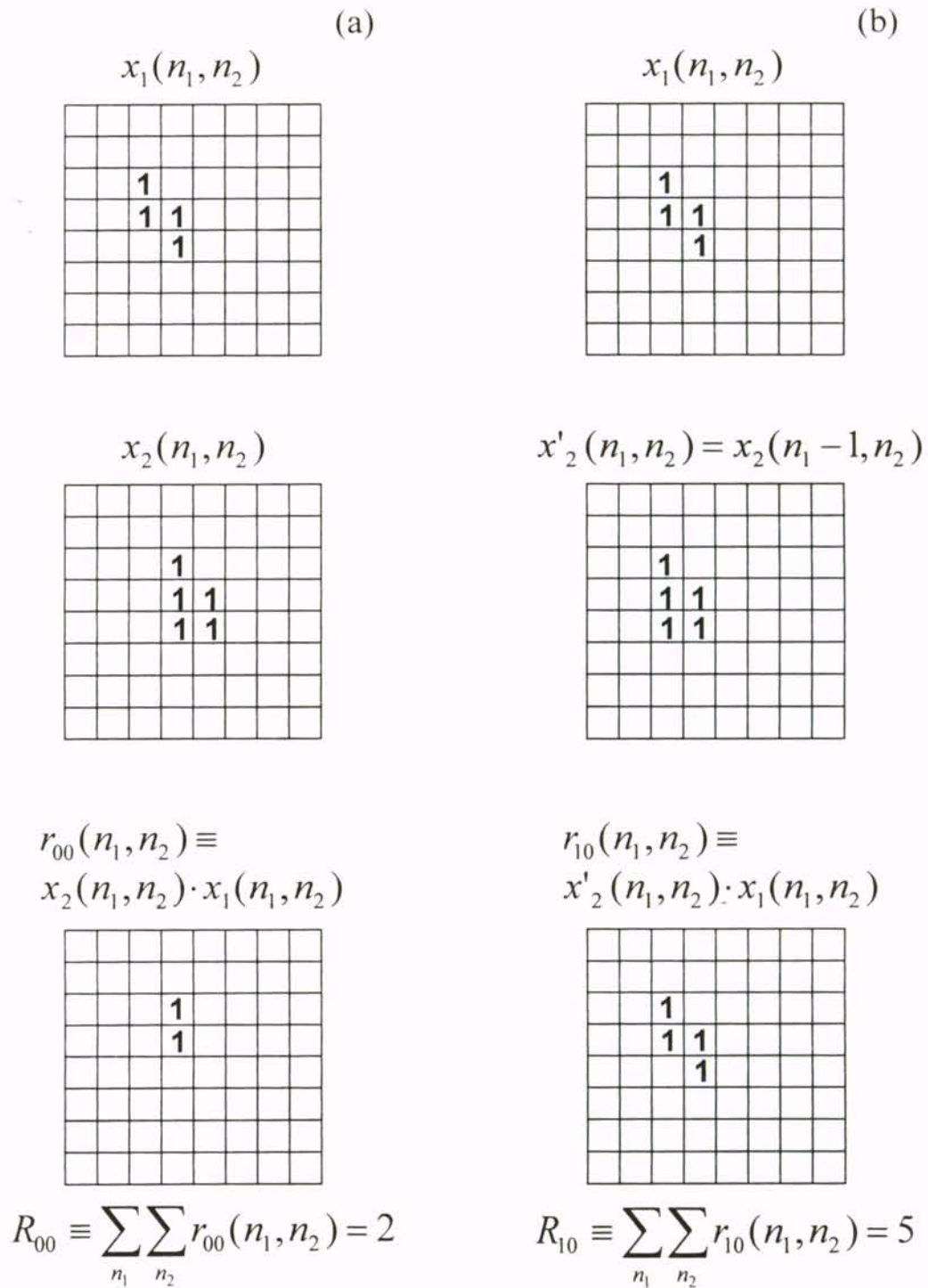


Figure 1-4. Motion detection by cross-correlation where a *maximum* in R_{ij} determines the value of displacement $\mathbf{u} \equiv (i, j)$ between consecutive images $x_1(n_1, n_2)$ and $x_2(n_1, n_2)$; (a) $\mathbf{u} = (0, 0)$ and $R_{00} = 2$, (b) $\mathbf{u} = (1, 0)$ and $R_{10} = 5$.

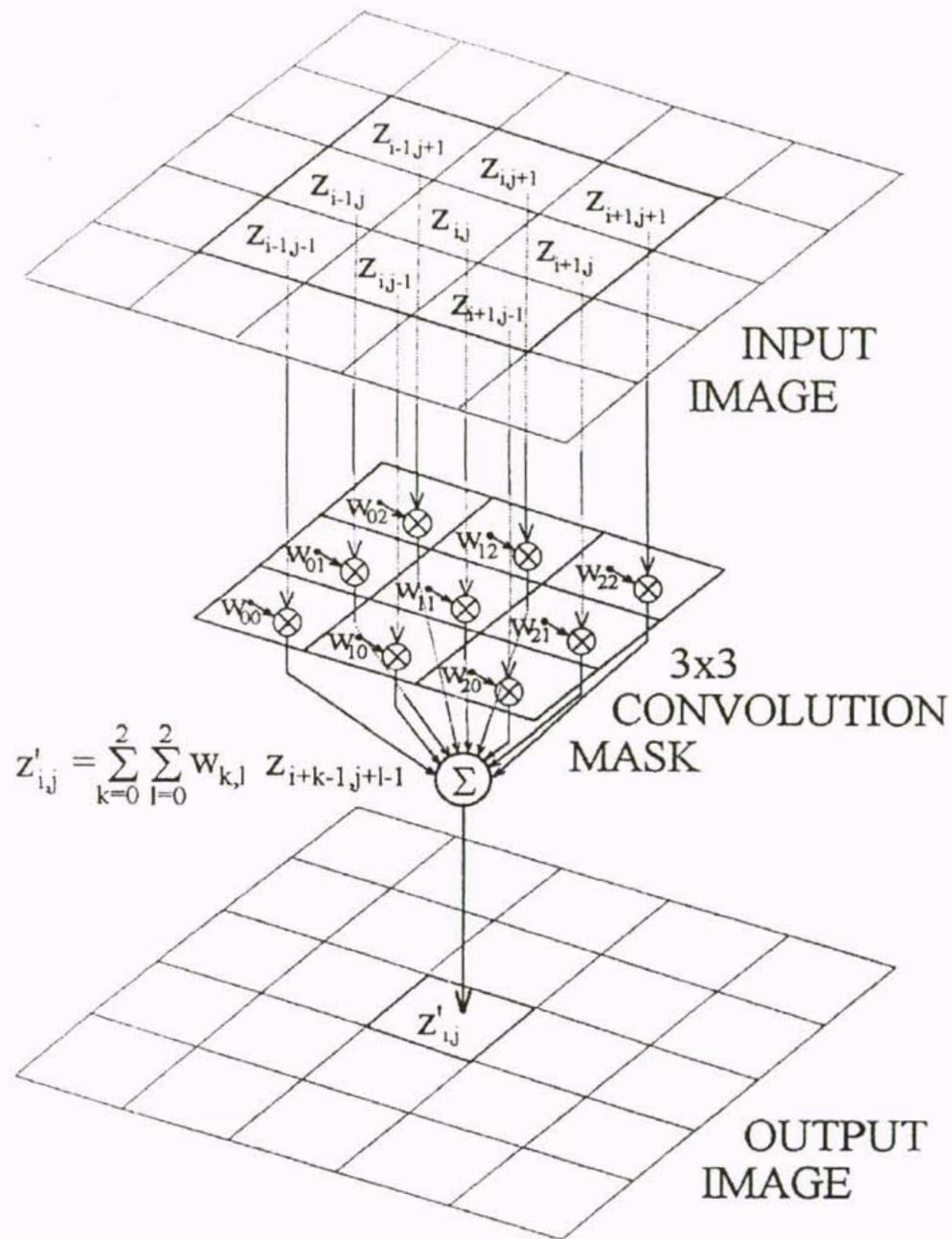


Figure 1-5. Two-dimensional spatial convolution. Figure from Weeks (1993).

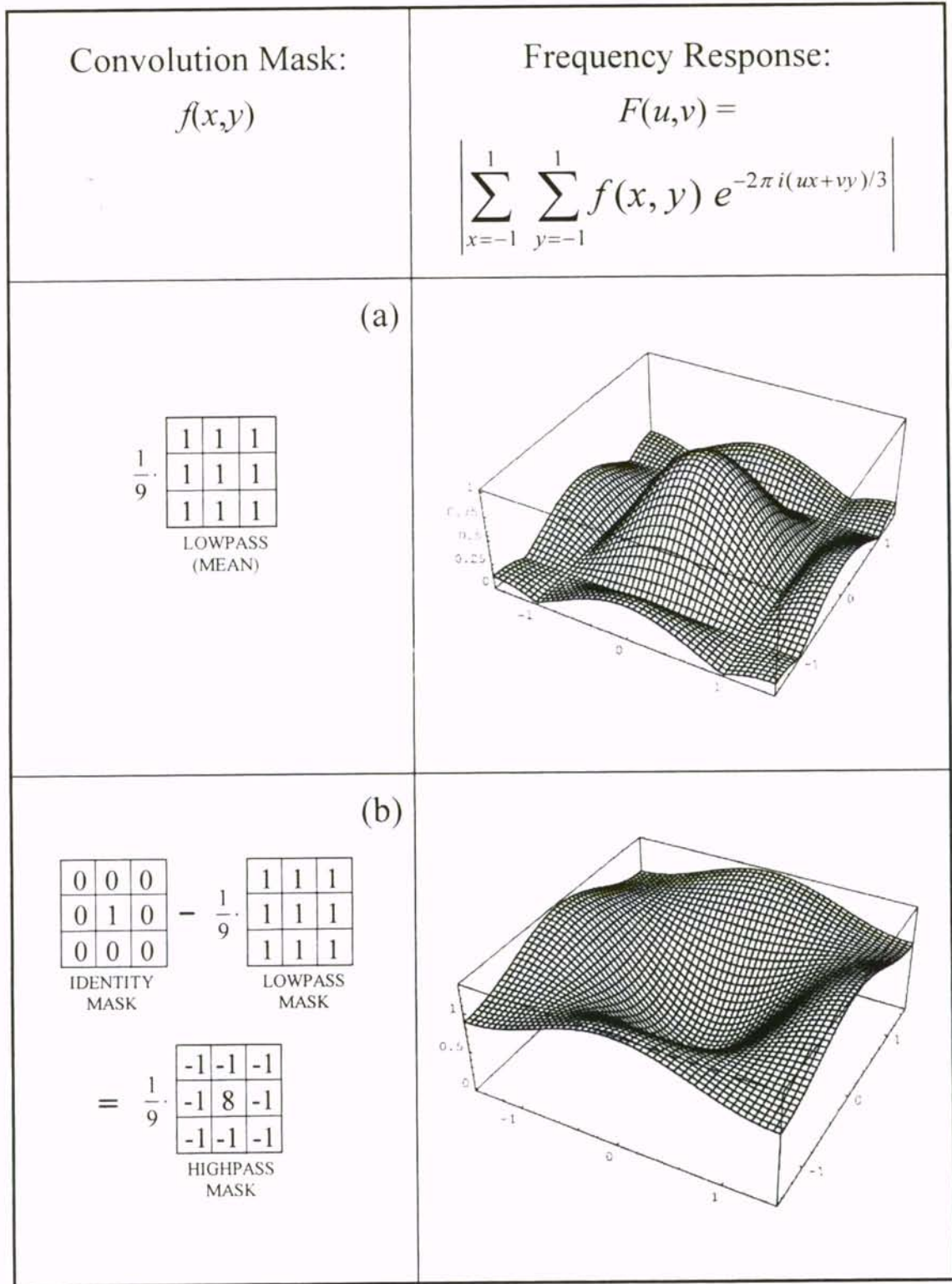


Figure 1-6. Spatial convolution filter masks; (a) 3 x 3 lowpass, (b) 3 x 3 highpass.

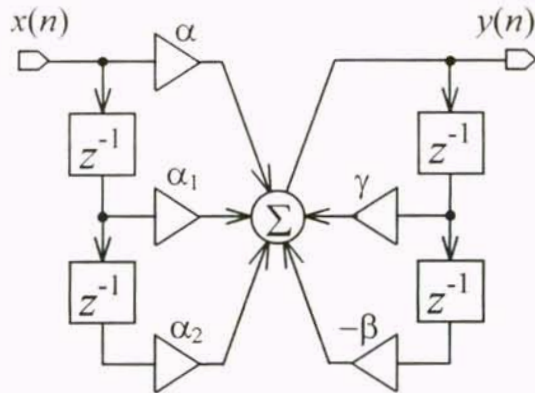


Figure 1-7. Second-order temporal convolution filter network, based on infinite impulse response (IIR) structure. See Table 1-1 for definition of coefficients.

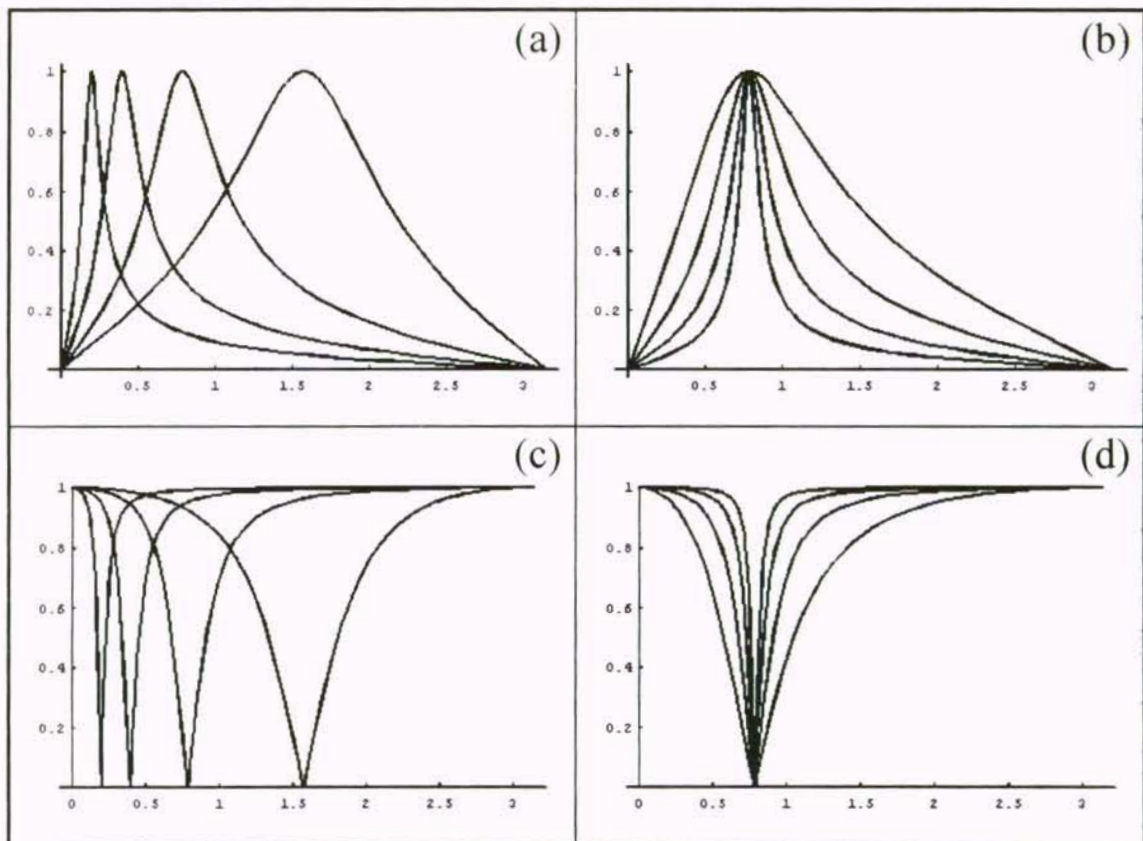


Figure 1-8. Magnitude response of IIR filters from Figure 1-7; (a) bandpass with $Q = 2$ and $\theta_0 = \pi/16, \pi/8, \pi/4, \pi/2$, (b) bandpass with $\theta_0 = \pi/4$ and $Q = 1, 2, 4, 8$, (c) bandstop with $Q = 2$ and $\theta_0 = \pi/16, \pi/8, \pi/4, \pi/2$, (d) bandstop with $\theta_0 = \pi/4$ and $Q = 1, 2, 4, 8$.

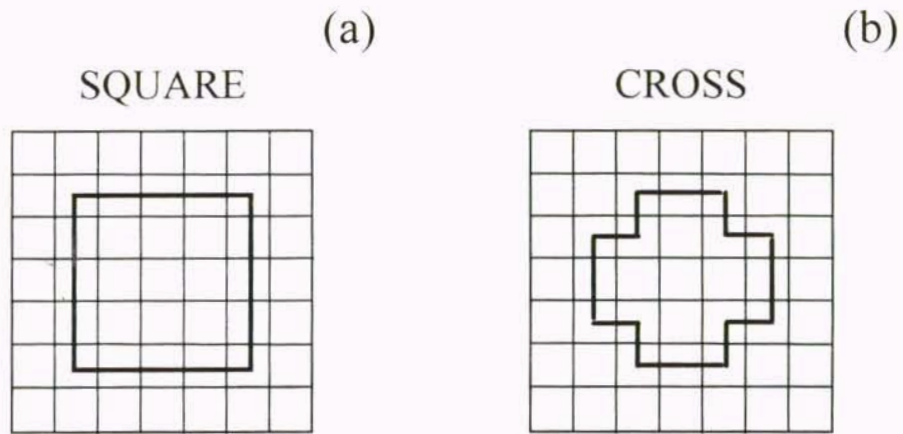


Figure 1-9. Common MF windows; (a) *square* filter window, (b) *cross* filter window.

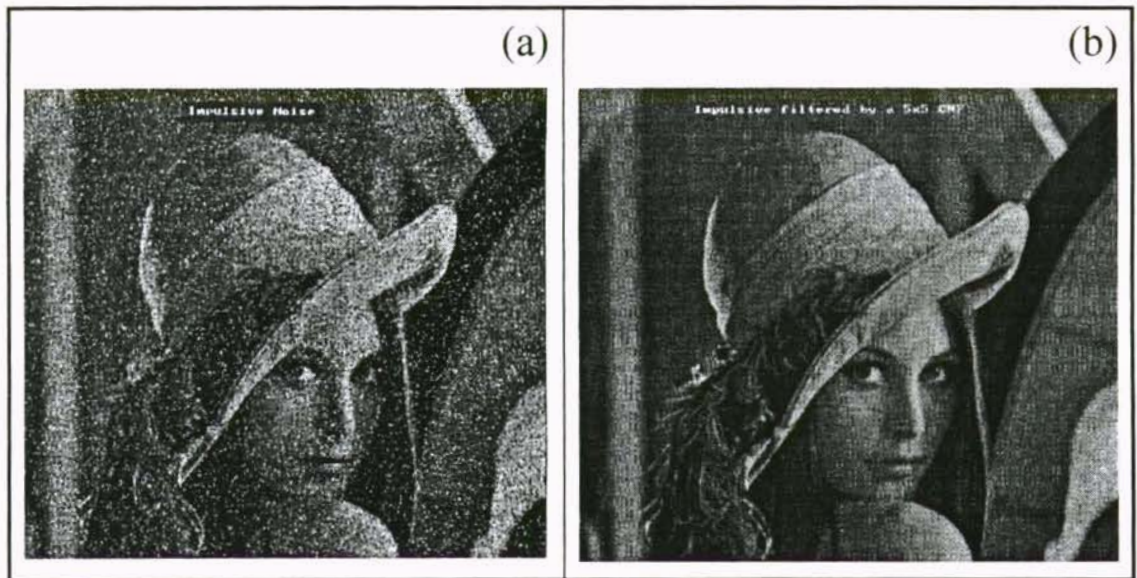


Figure 1-10. Image restoration with MF; (a) Image corrupted by impulse noise (salt and pepper noise), (b) image on left filtered by a 5 x 5 square CMF.

CHAPTER 2

RAINFALL MEASUREMENT INSTRUMENTATION

2.1 Background

Various types of rainfall measurement apparatus include: those which directly measure single drops, such as *disdrometers*; instruments that measure an averaged ensemble of single drops, such as *radar*; those which measure the volume of water collecting on the ground, such as the *accumulation rain gauge*; and instruments that measure the rate at which water is accumulating, such as the *tipping bucket* and *optical rain gauge*. In addition to these type of measurement classifications, there are also the spatial and temporal characteristics of the measurement to consider. Rain gauges and disdrometers measure rainfall at a single location or *gauge site*, whereas, radar measures a spatial average of rainfall in a three-dimensional volume, referred to as a *radar bin*.

2.2 Rain Gauges

All rain gauges measure rainfall at a single location where the measurement area or volume is much smaller than the scale of spatial variation of rainfall. All rain gauges also measure the volume of water accumulating at the gauge site. The sampling period of measurement may be very large, as in the case of an accumulation gauge, or on the order of a second or less, as in the case of the optical rain gauge.

2.2.1 Accumulation Gauge

Figure 2-1 shows a typical accumulation rain gauge. These type of gauges are frequently used in applications where long time averages of rainfall are of interest. A typical measurement from the National Weather Service (NWS) is the daily rainfall amount. After the accumulation gauge is read, it must be emptied in order to start a new measurement cycle. Typical measurement scales are in inches, with 0.1 in. resolution, or in metric units with 1 mm resolution.

2.2.2 Tipping Bucket

Figure 2-2 shows a tipping bucket rain gauge. This type of gauge is used in applications where hourly rainfall averages are of interest, such as in agricultural applications and flood forecasting. The resolution is usually 0.01 in., or in metric versions, 0.1 mm. Rainfall rates are easily computed from the tipping bucket rain gauge by dividing the measurement resolution by the time between tips. The tip of the bucket (see Figure 2-2b) triggers a momentary switch, creating an electrical pulse, thus activating a recording of the tip time.

The rainfall rate measurement accuracy and resolution of a tipping bucket is also dependent on the resolution of the time clock used to record tip times. In many tipping buckets with associated recording electronics, such as data loggers, the number of tips using a constant sample time (for example, 1 min) is recorded. The rainfall rate in this case is the number of tips multiplied by the tip bucket resolution, divided by the constant sample time. In research applications, the measurement accuracy of a tipping bucket can be increased an order of magnitude by placing a funnel over the collection area (see Figure 2-2a). The ratio of the funnel opening area to the area of the tipping bucket collector determines the increase in measurement resolution. Most tipping buckets have

an 8.0 in. diameter collection area. A 16 in. diameter funnel increases a gauge resolution of 0.01 in. to 0.0025 in. per tip, for example. However, under conditions favoring evaporation, the extra surface area of the funnel may lead to increased gauge error in the case of light rain.

2.2.3 Optical Rain Gauge

The optical rain gauge (ORG) measures rainfall by detecting the optical variations induced within the sample measurement volume by raindrops passing through a beam of semi-coherent infrared light. By measuring the transmitted light intensity using a photodetector, the voltage output of the detector represents the rainfall rate. A typical ORG (Scientific Technology, Inc. model ORG-105) output voltage V_{out} approximates rainfall rate R mm h⁻¹ with the following empirical relation:

$$R = 20 V_{out}^2 - 0.05 \quad (2.1)$$

where the output voltage is typically sampled by an analog to digital converter (ADC) for subsequent recording by data logger or computer.

One significant advantage of the ORG over mechanical systems such as the tipping bucket, is that they are less susceptible to errors induced by motion, making it a better choice for shipboard or buoy applications. However, since the calibration of the ORG is very critical and the ADC can drift with time, the tipping bucket is considered to be a more reliable and accurate measure of rainfall rate.

2.3 Disdrometer

Disdrometers measure and count single hydrometeors within a sample area, for the impact disdrometer; or within a sample volume, for the video disdrometer. Rainfall rate is computed by integrating (summing) the accumulation of single drop events. In

some sense, the disdrometer is a common link between the rain gauge and weather radar in that the disdrometer, like any other rain gauge, measures rainfall at essentially a single point. On the other hand, disdrometers like radar, indirectly estimate rainfall by means of a measurement of the drop size distribution (DSD). (Radar is measurement of the 6th moment of the DSD averaged over a volume of space, or *bin*, corresponding to the radar range increment and beam width).

2.3.1 Impact Disdrometer

Impact disdrometers measure individual raindrop impacts on a diaphragm, converting the collision of a single raindrop at terminal velocity to an electrical impulse. The disdrometer's processing electronics is responsible for converting the impulse amplitude to an equivalent drop diameter. The relationship between electrical signal amplitude and drop diameter is dependent on the various physical mechanisms which couple the drop collision to the mechanical portion of the sensing element.

2.3.1.1 Joss Disdrometer

Figure 2-3 shows a cross sectional view of the receiving body of the RD69 active Styrofoam disdrometer^[10,11]. The sensing element is a Styrofoam cone, approximately 10 cm in diameter, attached to a movable coil surrounded by a permanent magnet (much like a hi-fi speaker). A secondary coil is used to rapidly dampen the cone movement caused by a drop impact, utilizing the signal from the first coil as negative feedback. The electronics include an analog analyzer which converts the voltage pulse from a drop impact to a digital code for output to a computer. The digital code represents 20 drop diameter categories from 0.3 mm to 5.0 mm. This particular system has been used world wide since its introduction in 1969 and is still considered the standard impact disdrometer for which all others are compared.

2.3.1.2 APL Disdrometer

A cross sectional view of the APL disdrometer, built by the Applied Physics Laboratory, Johns Hopkins University, is shown in Figure 2-4. The receiving body consists of a solid Plexiglas cylinder with a beveled top upon which raindrops collide. A piezoelectric transducer is bonded to the cylinder which is bonded to a brass plate. The resonant frequency and damping factor is strongly dependent upon the size of the brass plate. As with the RD69, the peak voltage pulse represents the drop diameter size. The output of the sensor is applied to signal conditioning electronics which compresses the signal and determines its peak value. This value is digitized to a resolution of 8 bits and is output to an audio tape (older versions) or computer interface. The new *low-cost* version of the APL disdrometer is self-contained and records data in non-volatile memory for up to several months before it fills memory. Periodically, the data is downloaded to a portable computer.

2.3.1.3 UCF Disdrometer

The University of Central Florida (UCF) disdrometer, otherwise known as the *Acoustic Rain Gauge Array*^[12] (ARGA), is similar to other impact disdrometers (see Figure 2-5), except that in this case the drop impulse is acoustically coupled to the sensing element, consisting of a low-cost *electret condenser* microphone. The output signal of an individual disdrometer is connected to one channel of a stereo digital audio tape (DAT) recorder. The second channel of the DAT is connected to a tipping bucket rain gauge for reference. DATs have a distinct advantage over conventional analog recorders due to the increased capacity of DAT tapes (up to 4 hours at the lower sample rate of 32 kHz). In addition, the DAT automatically records a time stamp once per

second, making it ideal for correlating measurements to other disdrometers in different locations and correlating to NWS radar.

2.3.2 Video Disdrometer

The *2D-Video-Distrometer*^[13] measures numerous properties of single rainfall hydrometeors using commercial video camera technology, essentially taking detailed pictures of drops as they pass through the measurement sample volume. The instrument records the front and side view of each drop reaching the measuring volume, with a digitizing grid resolution on the order of 0.25 mm. This type of data permits the detailed study of the shape and terminal velocity of raindrops, as well as the corresponding drop size distribution. The Video-Distrometer may soon become the new base-line DSD measurement instrument from which all others are compared.

2.4 Weather Surveillance Radar (WSR-88D)

The Next Generation Weather Radar (NEXRAD), also known as WSR-88D, has replaced the previous National Weather Service WSR-57, WSR-74C, and WSR-74S systems. The deployment of a national network of WSR-88D radars officially began in February 28, 1994 with the commissioning of the first installation in Norman, OK. One month later, the Melbourne, FL WSR-88D system was commissioned. Nearly all of the planned NEXRAD systems have been installed and are now operational.

The WSR-88D utilizes Doppler radar technology to observe the presence and calculate the speed and direction of motion of severe weather conditions such as tornadoes and violent thunderstorms. The motion detection capabilities of NEXRAD are important characteristics of this new system which results in earlier and more reliable warnings of severe weather conditions, thus improving the NWS's capacity in public safety warnings and alerts.

2.4.1 Scan Strategy

NEXRAD operates in a *volume scan* configuration, repeating every five to six minutes when the radar is in precipitation detection mode, and approximately every ten minutes when the radar is in clear-air mode. The radar *base product* data consists of three independent measurement quantities: *reflectivity* which is the strength of the precipitation returns caused by scattering of the microwave radiation from the hydrometeors; *velocity* which is the direction and speed of the air motion (Doppler radar actually measures only the *radial* component of the wind vector); and *spectrum width* which is a measure of the range of velocity returns. These measurements are taken at several elevation angles between the base scan angle (about 0.5°) and the highest scan angle around 20° above the surface. The base products are processed by numerous algorithms, resulting in *derived products*. Both base and derived products are generated each volume scan.

The WSR-88D estimates rainfall by processing base reflectivity data taken from a 1.0 km x 1.0 km sample volume at an altitude of approximately 1.0 km. In order to maintain a somewhat constant height, a hybrid scan strategy is employed, as shown in Figure 2-6, where only four of the volume scan elevations are used for rainfall estimation. Beyond 50 km, the largest of the two reflectivity values contained in the lowest two scans is used for rainfall estimation. Figure 2-7 is an example of Melbourne NEXRAD derived product reflectivity data (15 min image updates), downloaded from the internet service *American Weather Concepts*.

2.4.2 Z-R Relation

WSR-88D data is processed through a series of algorithms and output is available after the completion of each volume scan. From the output base reflectivity Z , rainfall rates R are computed using the system default equation:

$$Z = 300R^{1.4} \quad (2.2)$$

where Z is in units of $\text{mm}^6 \text{m}^{-3}$. Typically, reflectivity is expressed in units of $\text{dBZ} = 10 \log_{10}(Z)$. Light rain corresponds to 35 dBZ, whereas, 55 dBZ reflectivity indicates very heavy downpours. Most measured rainfall occurs within this 20 dBZ range. The exact form of the Z - R relation is the topic of much research. One particularly popular variation of the NWS Z - R relation is the *dual regime*^[14] Z - R relation which uses one set of coefficients for *convective* rainfall and another set for *stratiform* rainfall. Convective rain is usually associated with thunderstorms, but in general, is rainfall which exhibits a large spatial gradient. Stratiform rainfall is usually lighter rain and is by definition, anything that is not convective.

2.4.3 Radar Refraction

The distance from the radar site to the point of interest on the ground S , the scan elevation angle λ , and radar range ρ , determine the height h of the beam center above the ground:

$$S = R_e \sin^{-1} \left(\frac{\rho \cos \lambda}{R_e + h} \right) \quad (2.3a)$$

$$h = R_e \left[\frac{\cos \lambda}{\cos(\lambda + S/R_e)} - 1 \right] \quad (2.3b)$$

where $R_e \approx 8500 \text{ km}$ is $4/3$ average earth radius. This model^[15] assumes that the index of refraction of the atmosphere is linearly dependent on h . Equations (2.3) can be simplified since $h \ll R_e$ and $S/R_e \ll \lambda$:

$$S \approx \rho \cos \lambda \quad (2.4a)$$

$$h \approx S \tan \lambda + \frac{S^2}{2R_e} \quad (2.4b)$$

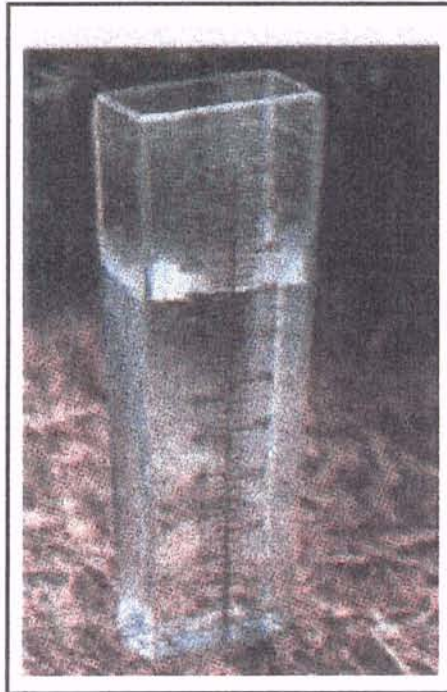


Figure 2-1. Accumulation rain gauge.

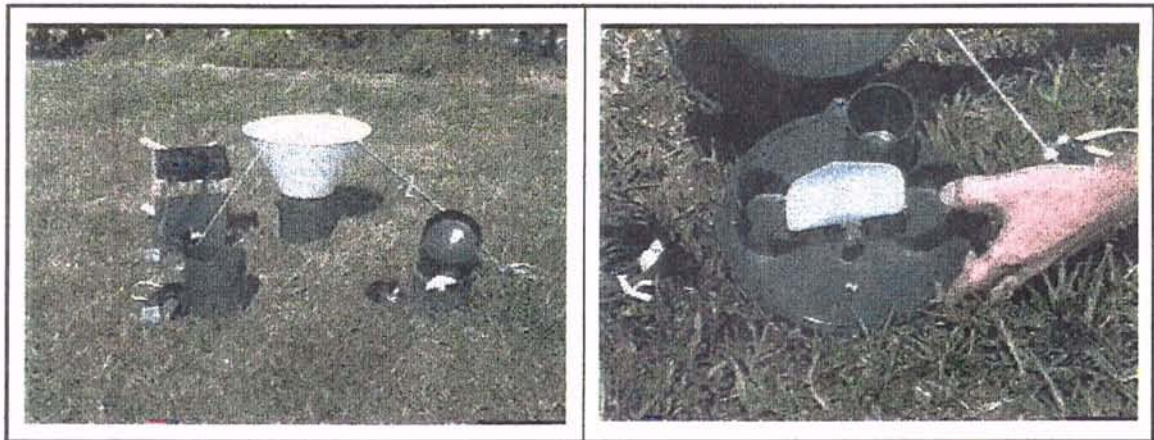


Figure 2-2. Tipping bucket rain gauge. Left, showing funnel used to increase sensitivity; right, showing close-up of tipping bucket mechanism.

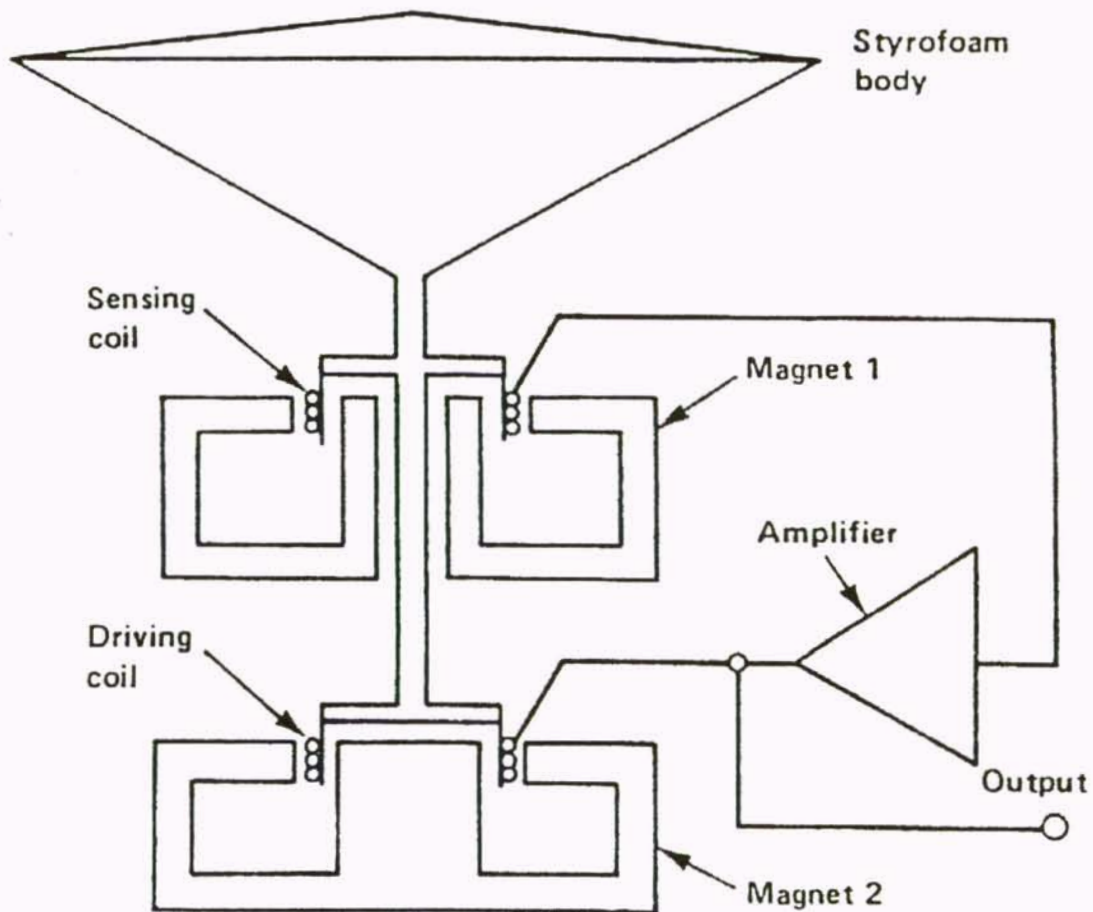


Figure 2-3. Schematic diagram of the RD69 (Distromet, Ltd.), commonly referred to as the *Joss disdrometer*. Note feedback amplifier used to rapidly dampen cone movement, thus decreasing instrument dead-time. Figure from Rowland (1976).

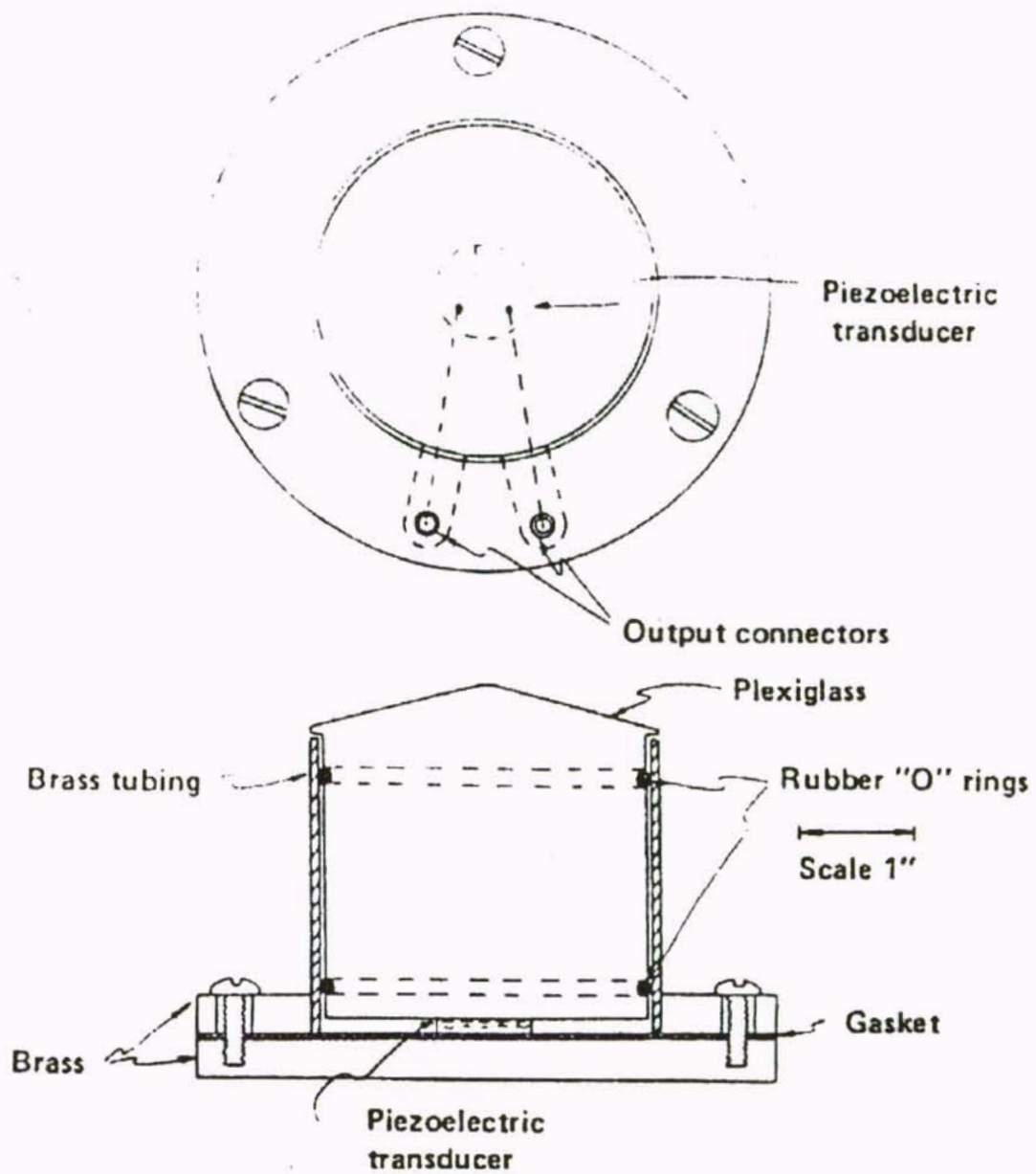


Figure 2-4. Schematic diagram of the APL disdrometer, built by the Applied Physics Laboratory, Johns Hopkins University. Figure from Rowland (1976).



Figure 2-5. Four UCF low-cost acoustic disdrometers (ARGA sensors).

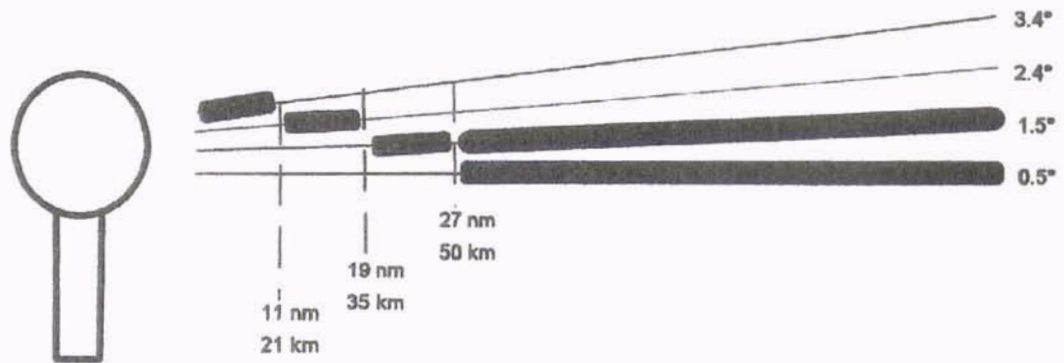


Figure 2-6. NWS NEXRAD hybrid scan strategy for rainfall estimation.

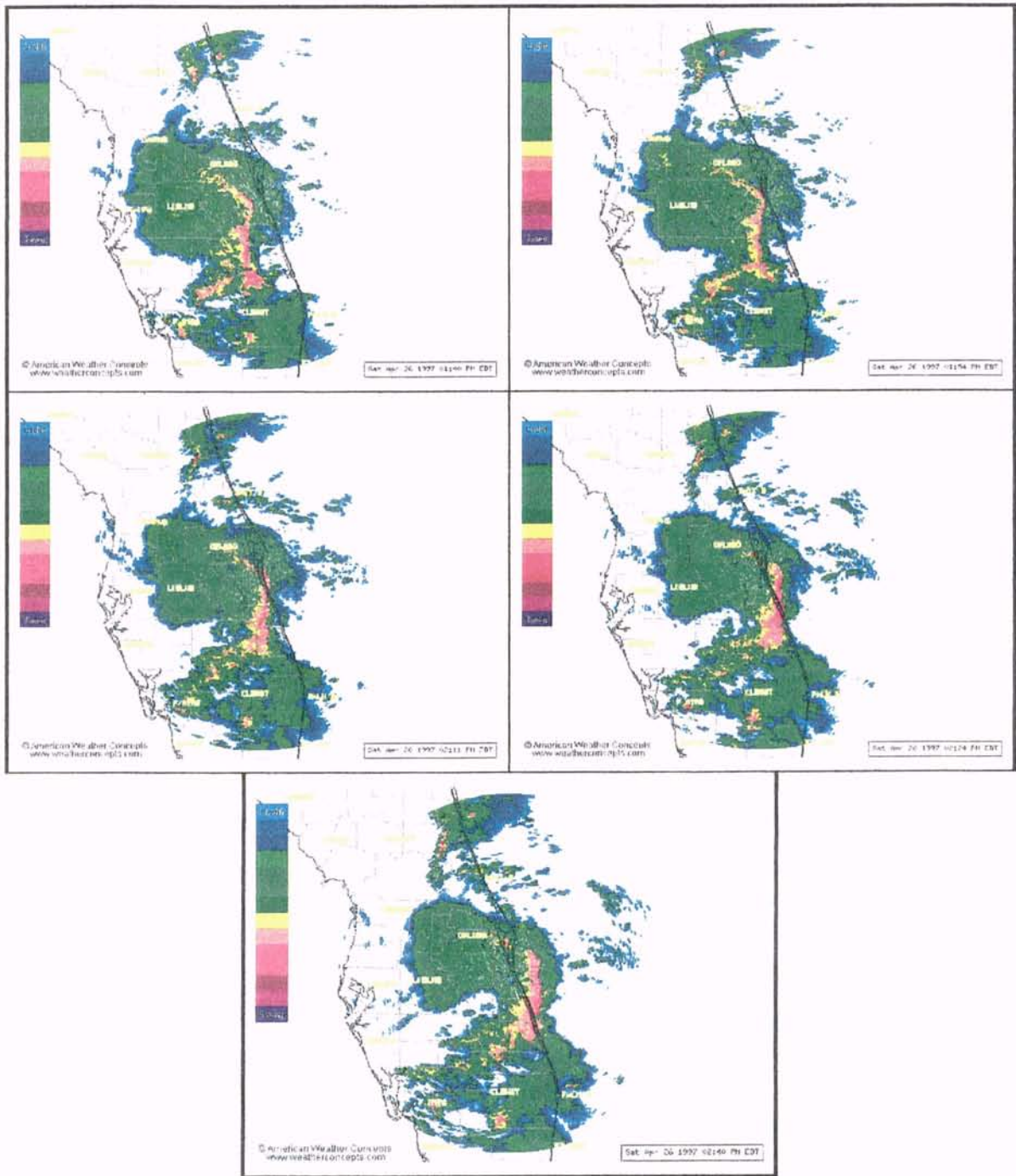


Figure 2-7. Example Melbourne NEXRAD derived product reflectivity data (from *American Weather Concepts*), April 26, 1997, 1:40P. Images are updated at approximately every 15 min.

CHAPTER 3 RAINDROP DYNAMICS

3.1 Background

- Most precipitation reaching the ground in the tropics does so in the form of raindrops. From a very simplistic point of view, these hydrometeors can be viewed as non-interacting and falling at a constant terminal velocity. Even though this assumption is not true, because of the many physical processes such as break-up, evaporation, and coalescence, it is nevertheless a safe assumption for the purpose of analyzing many useful properties of rainfall.

3.2 Drop Size Distribution

The drop size distribution is the number of raindrop hydrometeors per unit volume per drop size diameter D . Usually the DSD is denoted by $N(D)$ and is expressed in units of $\text{m}^{-3} \text{mm}^{-1}$ or cm^{-4} . The total number of drops N_T in a volume of air is equal to the integral of $N(D)$ over all drop diameters:

$$N_T = \int_0^{\infty} N(D) dD \quad (3.1)$$

where $N(D)dD$ is the number of drops per unit volume with diameters between D and $D + dD$.

Since the largest raindrop sizes found in nature do not exceed 6 to 7 mm, the DSD is often defined as:

$$DSD = \begin{cases} N(D) & D \leq D_{MAX} \\ 0 & D > D_{MAX} \end{cases} \quad (3.2)$$

Quantities involving the DSD, such as N_T , are then found from the truncated integral:

$$N_T = \int_0^{D_{MAX}} N(D) dD \approx \int_0^{\infty} N(D) dD \quad (3.3)$$

For most quantities involving integrals of $N(D)$, the error associated with the choice of large drop size cutoff is insignificant as compared to errors from other sources. A practical strategy, which will be used in this work, is to limit large drop sizes to 6 mm when performing data analysis. When performing analytical calculations on integrals involving $N(D)$, it is more convenient to use infinity as the upper bound for drop size since in this case, the integrals often reduce to the form of a simple *gamma function*.

3.2.1 Exponential Distribution

The simplest and probably most commonly used DSD is the *exponential distribution*^[16]:

$$N(D) = N_0 e^{-\Lambda D} \quad (3.4)$$

where N_0 and Λ are fitting parameters. In this case, the total number of drops per unit volume reduces to:

$$\begin{aligned} N_T &= \int_0^{\infty} N_0 e^{-\Lambda D} dD \\ &= N_0 \Lambda^{-1} \end{aligned} \quad (3.5)$$

3.2.2 Gamma Distribution

The *gamma distribution*^[17] was proposed in order to alleviate a problem at small drop diameters seen by researchers, which suggested that $N(D) \rightarrow 0$ as $D \rightarrow 0$:

$$N(D) = N_0 D^\nu e^{-\Lambda D} \quad (3.6)$$

The gamma distribution also allowed for a three parameter fit, where ν , as well as N_0 and Λ are the fitting parameters. In this case, the total number of drops per unit volume reduces to:

$$\begin{aligned} N_T &= \int_0^{\infty} N_0 D^\nu e^{-\Lambda D} dD \\ &= \frac{N_0}{\Lambda^{1+\nu}} \Gamma(1+\nu) \end{aligned} \quad (3.7)$$

Comparing Equations (3.4) and (3.5) to Equations (3.6) and (3.7), it can be seen that the exponential distribution is a special case of the gamma distribution where $\nu = 0$.

3.2.3 Marshall-Palmer Distribution

The *Marshall-Palmer*^[16] (MP) DSD is a special case of the exponential distribution, described by Equation (3.4), where historically the exponential DSD may have resulted as a generalization of the MP DSD. The MP DSD is characterized by its explicit definition of the fitting parameters, N_0 and Λ :

$$\begin{aligned} N_0 &= 8000 \text{ m}^{-3} \text{ mm}^{-1} \\ \Lambda &= 4.1 R^{-0.21} \text{ mm}^{-1} \end{aligned} \quad (3.8)$$

with R in units of mm h^{-1} . The original DSD data by Marshall and Palmer is shown in Figure 3-1.

The total number of drops for the MP DSD, based on Equation (3.5), is:

$$\begin{aligned}
 N_T &= N_0 \Lambda^{-1} \\
 &= (N_0 / 4.1) R^{0.21} \\
 &= (1951.2) R^{0.21} \text{ m}^{-3}
 \end{aligned} \tag{3.9}$$

According to the MP DSD and Equation (3.9), the total number of drops per unit volume increase as the 0.21 power of R .

3.3 Raindrop Terminal Velocity

The equation of motion for a raindrop of mass m_D in a uniform gravitational field of acceleration g , falling in the z direction (defined positive from cloud to ground, where $z = 0$ at the initial starting point in the cloud), is:

$$m_D \ddot{z} = m_D g - \mu_D \dot{z}^2 \tag{3.10}$$

where the first term on the right-hand-side (RHS) is the gravitational force and the second term on the RHS is the force due to frictional drag through air. Approximations for the quantities in Equation (3.10) can be estimated by assuming a spherical drop shape of diameter D and by neglecting the change in atmospheric density with altitude:

$$m_D \approx \frac{\pi D^3 \rho_w}{6} \tag{3.11a}$$

$$\mu_D \approx \frac{\pi D^2 \rho C_d}{8} \tag{3.11b}$$

where ρ_w is the density of water, ρ is the density of air (neglecting altitude dependence), and C_d is the drag coefficient of a spherical drop. By substituting $v = \dot{z}$ in the equation of motion, Equation (3.10) becomes:

$$v \frac{dv}{dz} = g - \frac{\mu_D}{m_D} v^2 \quad (3.12)$$

$$= g \left(1 - v^2 / v_D^2 \right)$$

where $v_D \equiv \sqrt{m_D g / \mu_D}$. The solution to the differential equation of Equation (3.12) is:

$$v = v_D \left(1 - e^{-2gz/v_D^2} \right)^{1/2} \quad (3.13)$$

As $z \rightarrow \infty$ in Equation (3.13), $v \rightarrow v_D$, thus implying that v_D is the terminal velocity of a drop of diameter D . Experimental data^[18] for drop velocities versus fall height for several drop sizes, is shown in Figure 3-2, along with the velocities predicted by Equation (3.13). Note that Equation (3.13) also correctly predicts that as z goes to zero:

$$v \xrightarrow{z \rightarrow 0} (2gz)^{1/2} \quad (3.14)$$

which is the free fall solution in a vacuum, where the drag force vanishes.

One of the primary problems with the former arguments is the assumption that the raindrop shape is spherical. Figures 3-3 and 3-4 show high-speed photographs^[19,20] of drops at terminal velocity. For drop diameters larger than about 3 mm, the shape becomes more flattened as the diameter increases. For this reason, terminal velocity formulas are usually empirical and are not usually based on the spherical drop shape assumption of Equation (3.11b).

3.3.1 Approximation by Gunn (1948)

A simple form of drop terminal velocity v_D is described by a simple power-law^[21]:

$$v_D \approx K_G D^{1/2} \quad (3.15)$$

where $K_G = 4.5$ when drop diameter D is expressed in mm and terminal velocity is in units of m s^{-1} . This particular form of v_D is particularly useful when evaluating integrals over drop size, involving drop size distribution functions. Specific examples of this will be presented in sections to follow.

3.3.2 Approximation by Best (1950)

An improved approximation for terminal velocity^[22], which takes into account the variation of velocity with altitude, due to atmospheric density, is:

$$v_D \approx A e^{bz} \left\{ 1 - e^{-(D/a)^n} \right\} \quad (3.16)$$

where $A = 9.58 \text{ m s}^{-1}$, $b = 0.0854 \text{ km}^{-1}$, z is the elevation at the ground (or at the point of measurement), D is the drop diameter measured in mm, $a = 1.77 \text{ mm}$, $n = 1.147$, and v_D is expressed in units of m s^{-1} .

3.3.3 Approximation by Atlas (1973)

Another approximation for terminal velocity^[23], which is also an improvement over the power-law form of Gunn, is:

$$v_D \approx v_0 (1 - K e^{-cD}) \quad (3.17)$$

where $v_0 = 9.65 \text{ m s}^{-1}$, $K = 1.067$, $c = 0.6 \text{ mm}^{-1}$, and D is expressed in mm. Even though this form of v_D is not as simple as Gunn's approximation, it nevertheless results in a form which is relatively easy to manage when evaluating integrals involving DSD functions.

3.4 Moments of the DSD

Many useful atmospheric and meteorological quantities can be calculated simply by evaluating the x th moment of the DSD:

$$M_x = \int_0^{\infty} D^x N(D) dD \quad (3.18)$$

For example, the total number of drops N_T in a volume of air is equal to M_0 , the zeroth moment of the DSD, as verified by Equation (3.1).

3.4.1 Liquid Water Content

The third moment M_3 of the DSD is proportional to the amount of water in a unit volume of air:

$$\begin{aligned} V &= \frac{\pi}{6} \rho_w \int_0^{\infty} D^3 N(D) dD \\ &= \frac{\pi}{6} \rho_w M_3 \end{aligned} \quad (3.19)$$

If the exponential DSD described by Equation (3.5) is used to evaluate M_3 , the result is:

$$\begin{aligned} V &= \frac{\pi}{6} \rho_w N_0 \int_0^{\infty} D^3 e^{-\Lambda D} dD \\ &= \pi \rho_w N_0 \Lambda^{-4} \end{aligned} \quad (3.20)$$

where ρ_w is the density of water.

3.4.2 Rainfall Rate

The integral over D of the product of terminal velocity and DSD is equal to the rainfall rate. If the terminal velocity v_D is described by Gunn's approximation, Equation (3.15), rainfall rate R becomes the 7/2 moment of the DSD:

$$\begin{aligned} R &= \frac{\pi}{6} K_G \int_0^{\infty} D^{7/2} N(D) dD \\ &= \frac{\pi}{6} K_G M_{7/2} \end{aligned} \quad (3.21)$$

where $K_G = 4.5$ (drop diameter D is expressed in mm and terminal velocity in units of m s^{-1}). If the exponential DSD of Equation (3.5) is used, R then evaluates to:

$$\begin{aligned} R &= (0.0036) \frac{\pi}{6} K_G N_0 \int_0^{\infty} D^{7/2} e^{-\Lambda D} dD \\ &= (0.0036) \frac{35}{32} \pi^{3/2} K_G N_0 \Lambda^{-9/2} \end{aligned} \quad (3.22)$$

where the scale factor 0.0036 places R in standard unit of mm h^{-1} .

3.4.3 Radar Reflectivity

The sixth moment M_6 of the DSD is approximately equal to the radar reflectivity:

$$\begin{aligned} Z &= \int_0^{\infty} D^6 N(D) dD \\ &= M_6 \end{aligned} \quad (3.23)$$

If the exponential DSD of Equation (3.5) is used, Z then evaluates to:

$$\begin{aligned} Z &= N_0 \int_0^{\infty} D^6 e^{-\Lambda D} dD \\ &= 720 N_0 \Lambda^{-7} \end{aligned} \quad (3.24)$$

where Z is in standard units of $\text{mm}^6 \text{m}^{-3}$. Note that a commonly used measure of Z is $\text{dBZ} = 10 \log_{10}(Z)$.

3.4.4 Z-R Relation

The rainfall rate R described by Equation (3.22) can be combined with the radar reflectivity Z given by Equation (3.24), by eliminating Λ :

$$Z = \left(\frac{274211}{K_G^{14/9} N_0^{5/9}} \right) R^{14/9} \quad (3.25)$$

Using $K_G = 4.5$ and $N_0 = 8000$, Z becomes:

$$Z = a R^b \quad (3.26)$$

where $a \approx 179.3$ and $b = 14/9 \approx 1.56$. Equation (3.26) is a Z-R relation derived from Gunn's terminal velocity and the exponential DSD. Equation (3.26) is the well known Z-R power law used to convert weather surveillance radar (WSR) data to estimations of rainfall amounts. However, it should be noted that the National Weather Service (NWS) has adopted the modified values of $a = 300$ and $b = 1.4$ for use with its WSR-88D radar network.

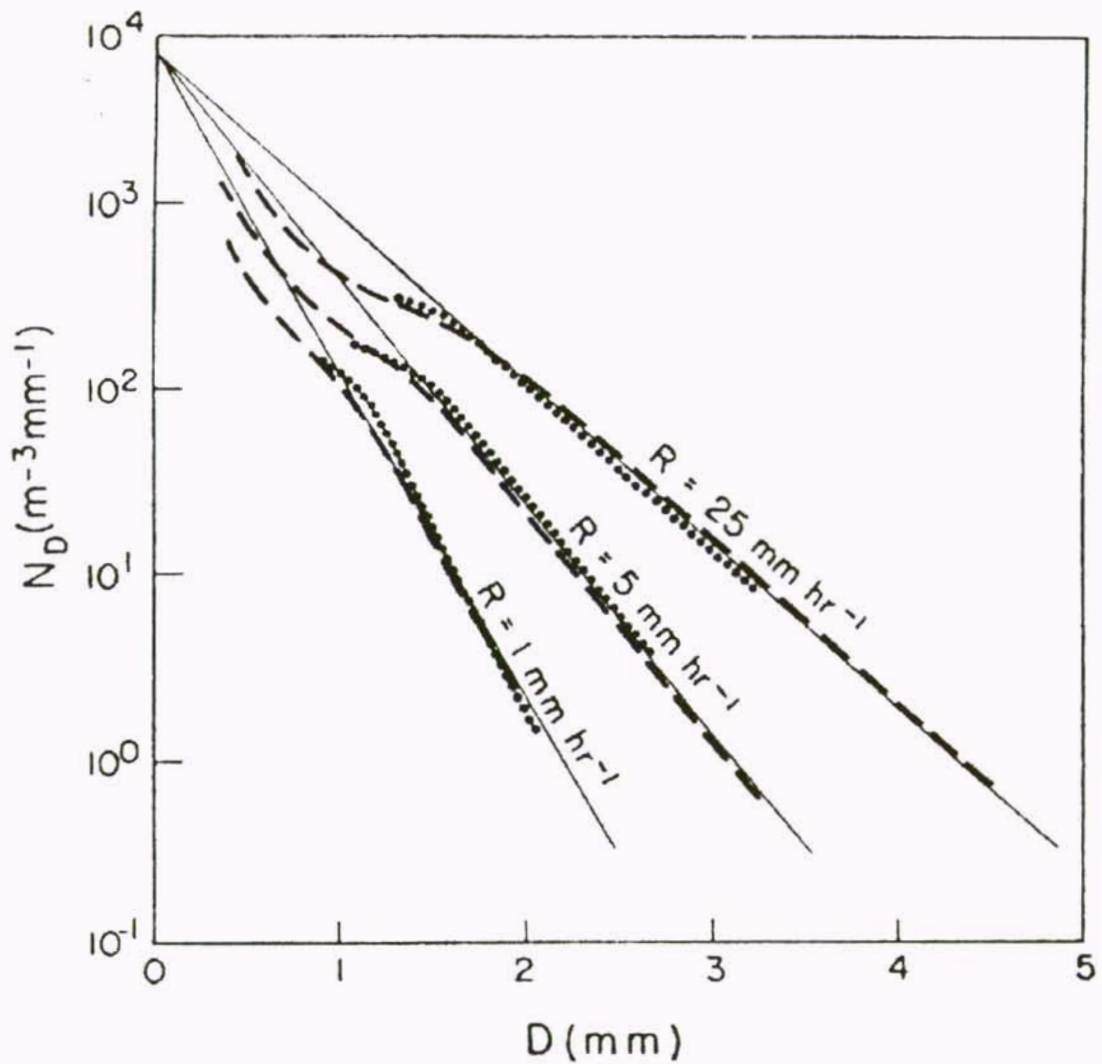


Figure 3-1. Solid lines are plots of the MP DSD, Equation (3.4) with parameters defined by Equations (3.8), for the three rainfall rates shown, $R = 1$, $R = 5$, and $R = 25$ mm h^{-1} . Dotted and dashed lines are rainfall rate data averaged from many measurements.

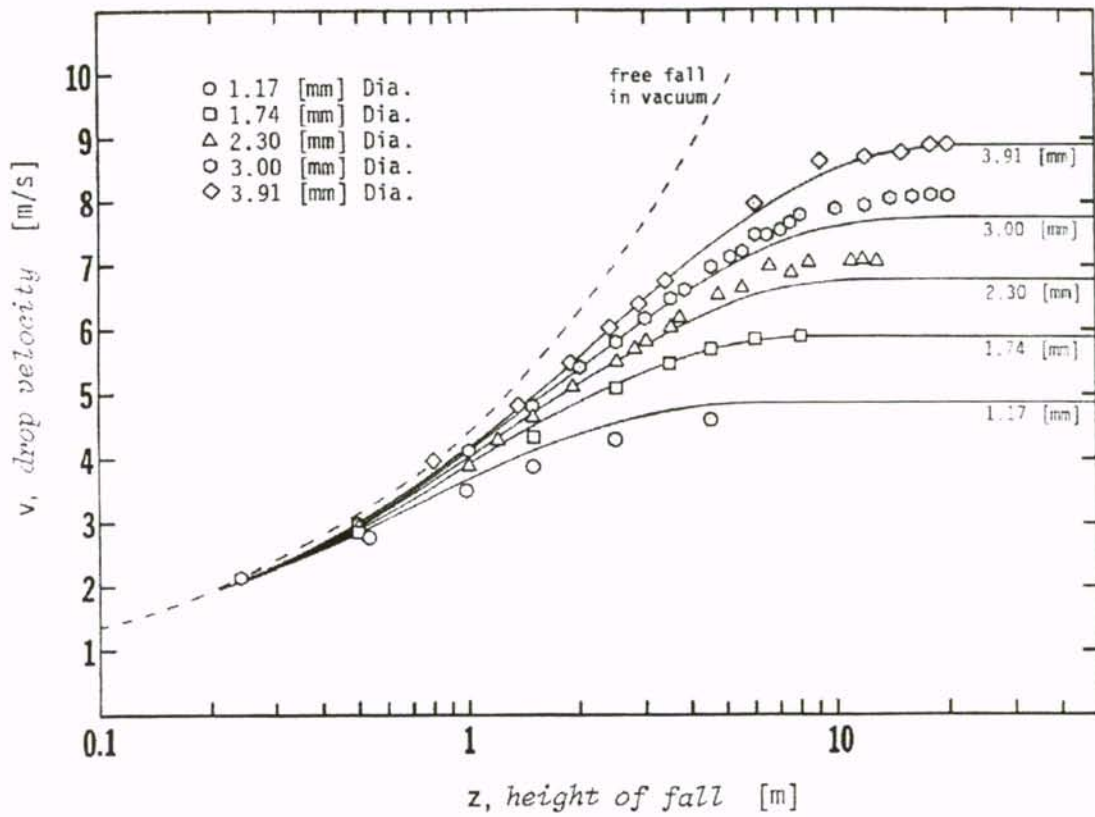


Figure 3-2. Symbols are experimental data of drop velocity versus fall height by Laws (1941). Solid lines are the velocities predicted by Equation (3.13) using terminal velocity v_D by Gunn (1948), Equation (3.15).

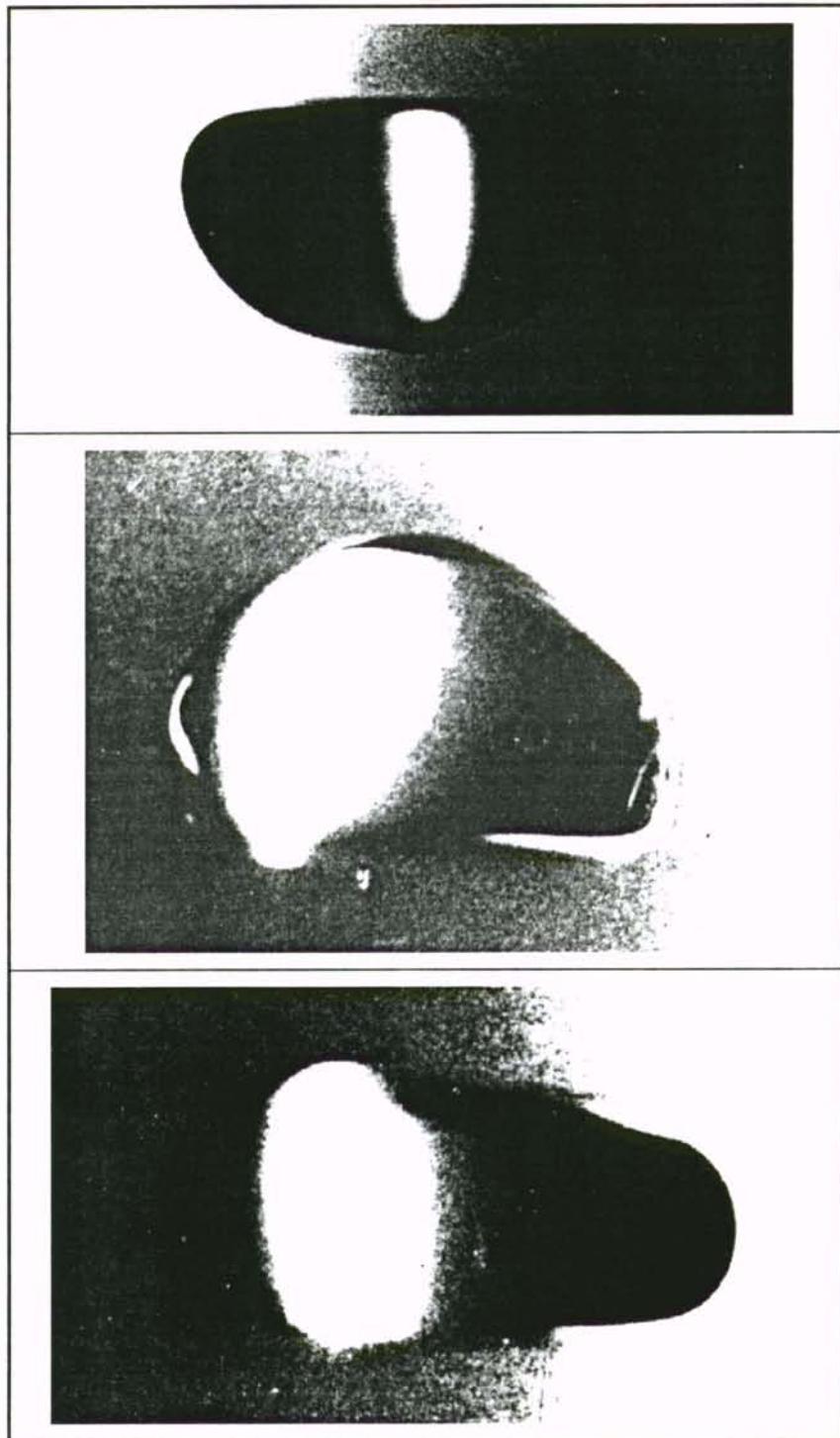


Figure 3-3. High-speed photographs of falling raindrops, at or near terminal velocity. Figure from Edgerton (1939).

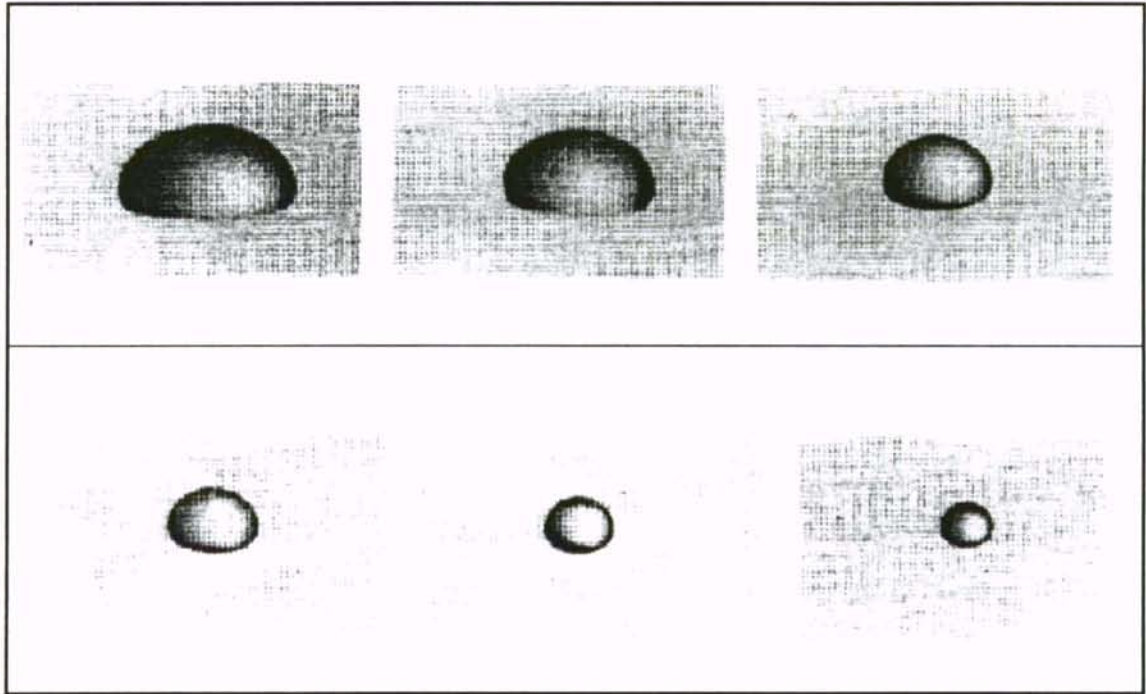


Figure 3-4. Wind tunnel simulations of falling raindrops at terminal velocity. Drop diameters, from large to small, are: 8.00, 7.35, 5.80, 5.30, 3.45, and 2.70 mm. Figure from Pruppacher (1970).

CHAPTER 4

INTERPOLATION OF RAIN GAUGE AND RADAR DATA

4.1 Background

In many applications of water resources management, such as in agriculture and forestry, it is desirable to accurately determine areal rainfall amounts with high temporal and spatial resolution. A microscale network (separations on the order of 1 to 3 km) of rain gauges provides a reliable solution to detailed rainfall mapping for city size areas, farms, or park lands. However, dense rain gauge networks are not cost effective or practical for larger geographical areas such as counties, states, or regions due to the sheer number of gauges required. After all, one of the primary justifications for the development of the National Weather Service network of NEXRAD radars was that it would provide improved rainfall information by filling in estimates over areas where large gaps in gauges exist.

There are two issues associated with weather radar rainfall estimation; scan strategy and calibration of the rainfall estimation algorithm. Since the primary aim of the NWS is public safety, the chosen radar scanning technique is optimized for surveillance and warning of severe weather conditions. The resulting volume scan strategy, beam width, and range resolution are therefore not optimized for rainfall estimation. The issue of radar rainfall algorithm calibration is a more complex problem. In the early days of weather radar, it was believed that a simple Z - R relation (Z is radar reflectivity and R is rainfall rate) would suffice to accurately estimate rainfall amounts from radar measurements. Previously, most research focused on finding the “best” Z - R relation.

However, it is now common knowledge that this approach is a gross over simplification of the problem^[24]. Recent work in this area has split into three directions: (1) a comprehensive data analysis based on the complete volume scan and time series of radar images; (2) the assumption that only a statistical approach will yield useful results, based on long time averages and large areas of measurement; and (3) the application of other measurement techniques and instruments such as polarimetric radar^[25] and ground based disdrometers^[13] to enhance present capabilities.

The primary motivation of the work presented in this dissertation was to develop a useful method of combining and interpolating rain gauge data for the purpose of real-time rainfall mapping. For any geographical area larger than a few hundred square kilometers, the network of NWS radar provides the best available solution for rainfall mapping. In this case, clusters of densely spaced rain gauges, as well as single isolated gauges in the radar service area^[26], may be used to improve radar rainfall algorithm calibration and subsequent real-time rainfall estimation accuracy.

For global coverage (macro or synoptic scale), NASA's Tropical Rainfall Measurement Mission (TRMM) satellite radar provides the best rainfall mapping solution. Calibration and verification of the satellite radar measurements are performed by specific Ground Validation (GV) sites consisting of rain gauge networks and NWS WSR-88D radar. A robust gauge interpolation algorithm is essential to the successful implementation of reliable ground truth for calibration of the NWS rainfall algorithm and subsequent calibration of the TRMM satellite radar.

4.2 Mathematical Development

Atmospheric dynamics are controlled by four fundamental laws of physics: conservation of mass, conservation of momentum, conservation of energy, and conservation of angular momentum (also referred to as *vorticity*). Two types of

coordinate systems are commonly used to describe the mathematical laws of atmospheric fluid motion in a control volume. In the *Eulerian* frame of reference, the control volume consists of an infinitesimal parallelepiped whose position is fixed relative to the coordinate axes. Mass, momentum, and energy conservation will depend on fluxes caused by fluid flow through the boundaries of the control volume. In the *Lagrangian* frame, the control volume consists of an infinitesimal mass of fluid particles which move about following the motion of the fluid, always containing the same fluid particles.

The difference in these two descriptions of atmospheric fluid motion is exemplified by a convective thunderstorm which is moving rapidly due to wind motion (advection velocity). An observer on the ground next to a rain gauge, is in the Eulerian coordinate system and will most likely witness a large time rate of change in rainfall rate, as measured by the rain gauge. Most of the time dependence of the observed (and measured) gauge rainfall is due to the passing of the convective storm system over the gauge site due to advection. An observer in a balloon whose speed matches the advection velocity, is in the Lagrangian coordinate system. This observer may notice a much smaller time rate of change of rainfall rate since he is observing the total time derivative of rainfall.

4.2.1 Conservation Equation

The general differential equation for conservation of a meteorological field variable is:

$$\dot{f}(\mathbf{r}, t) = \frac{\partial f(\mathbf{r}, t)}{\partial t} + \mathbf{u}(\mathbf{r}, t) \cdot \nabla f(\mathbf{r}, t) = \text{source terms} \quad (4.1)$$

where $f(\mathbf{r}, t)$ may be a meteorological quantity such as radar reflectivity Z or rainfall rate R , at a point in space defined by the location vector \mathbf{r} and time t , defined by an *Eulerian* coordinate system (an *inertial* coordinate system, neglecting the effects of the earth's rotation). $f(\mathbf{r}, t)$ is moving with an advection velocity $\mathbf{u}(\mathbf{r}, t)$ which is in general

also a function of the location vector \mathbf{r} and time t . Note that the term on the left hand side of Equation (4.1) is zero in the absence of *source* terms.

In order to evaluate the total time derivative term, $\dot{f}(\mathbf{r}, t)$, it is often convenient to transform to a *Lagrangian* frame of reference which is traveling with the advection velocity $\mathbf{u}(\mathbf{r}, t)$. (The Lagrangian system is not generally an inertial system since it may be accelerating). If at $t = 0$, the origin of the earth coordinate system, or Eulerian frame of reference, and Lagrangian system coincide, then the location vector \mathbf{r}' in the Lagrangian frame is related to \mathbf{r} in the Eulerian frame by $\mathbf{r}' = \mathbf{r}(t) - \mathbf{u} t$ in the case of constant advection velocity (space and time independent). Since by definition the advection velocity is zero in the Lagrangian frame, Equation (4.1) reduces to:

$$\frac{\partial f(\mathbf{r}', t)}{\partial t} = \dot{f}(\mathbf{r}', t) \quad (4.2)$$

According to Equation (4.2), determination of the total time derivative of an atmospheric quantity such as Z or R is most easily accomplished in a Lagrangian coordinate system.

A useful approximation, which will lead to a spatial and temporal interpolation method for radar and rain gauge data, is to assume that the total time derivative term in Equation (4.1) is small compared to the advective term:

$$\frac{\partial f(\mathbf{r}, t)}{\partial t} \approx -\mathbf{u}(\mathbf{r}, t) \cdot \nabla f(\mathbf{r}, t) \quad (4.3)$$

There are two cases to consider: temporal interpolation of radar data, and spatial interpolation of rain gauge data. These topics will be discussed in following sections.

4.2.2 Measurement of Advection

Wind motion in the atmosphere is a very complex process. Velocity is in general a three-dimension vector, where the vertical component may, for example, be associated

with the updraft/downdraft motion of convective thunderstorms. Since the atmosphere is very thin compared to its extent, the movement of storm systems may be considered a horizontal motion, described by a two-dimensional velocity vector. For example, squall lines associated with mesoscale convective systems (MCSs), consisting of interacting thunderstorm cells and large areas of trailing stratiform precipitation^[27], often move in a direction perpendicular to the line of thunderstorm cells. However, the motion of the individual storm cells, and sometimes imbedded tornadic cyclones, may be along the squall line, transverse to the velocity of the storm front. Vertical dependence of advection may be examined when observing the passing of clouds overhead in a direction opposite the wind direction on the ground. The “sea-breeze boundary” along a coast-line may also generate very complex horizontal wind motions.

For the purpose of the following discussions, advection velocity will be considered a constant over a microscale area, on the order of 10 km^2 or less; and for some interval of time, on the order of one hour or less. The justification for this characterization of advection is that even though it is generally not a constant in time or space over mesoscale areas (hundreds of km^2) and several hours, it can be formed as a piece-wise construction of constant velocities. The work presented in this chapter focuses on the regime where advection is approximately constant, i.e., microscale spatial extents and time scales on the order of minutes or tens of minutes. It will be assumed that the techniques developed under this constraint may be extended to larger spatial and time scales by connecting the microscale solutions using a numerical mosaicing scheme.

4.2.2.1 Cross-Correlation of Radar Data

The advection velocity can be estimated^[28] by performing a cross-correlation between consecutive frames of reflectivity $Z_n(x, y)$ and $Z_{n+1}(x, y)$, where n is the time index of the radar scan image, generally occurring every 5 min or so.

$$\rho_n(\mathbf{u}) = \int_A (Z_n(x, y) - \mu_n) (Z_{n+1}(x, y) - \mu_{n+1}) dA \quad (4.4)$$

where μ_n is the average value of $Z_n(x, y)$ over a region of area A . The best estimate for advection velocity \mathbf{u} is that which maximizes $\rho_n(\mathbf{u})$.

The spatial coordinates x and y may be, for example, the raw WSR-88D base scan coordinates (lowest elevation scan of 0.5°), consisting of 1.0 km range increments and azimuth angle increments of 1.0° . At times, it may be more convenient to work with an interpolated set of reflectivity values, generated by the WSR-88D precipitation products software^[29], having a spatial resolution of 2 km x 2 km. Whatever the choice of x and y used to describe a time sequence n of two-dimensional radar reflectivity images $Z_n(x, y)$, maximizing the cross-correlation of adjacent image scans (as described by Equation (4.4)) by a discrete summation over a microscale region A , yields an estimate of the advection velocity \mathbf{u} associated with that spatial area.

This process may be better visualized by studying the 5 min radar image scans (base reflectivity) shown in Figures 7-4. The radar data of Figures 7-4 corresponds to a region where strong westerly advection collided with the sea-breeze boundary from the Florida east coast. The cluster of cells moving from left to right in the upper to middle portion of these images, show a predominately easterly advection; whereas the cell cluster moving up from the bottom of the image sequence, show a predominately north-easterly advection velocity. A microscale region of study is designated by the circle of radius 1.3 km where the advection is assumed to be constant over that area and over the time sequence of four radar scans (20 min). Note that the radar images of Figures 7-4 represent a 16 km x 16 km area, SSW of the Melbourne NWS radar.

The region of integration (discrete summation) prescribed by Equation (4.4) needs to be larger than the microscale region of study (circled area) in Figures 7-4, due to the displacement of correlated features between adjacent images, as a result of scan time and advection velocity. An upper limit of integration area is imposed by the variation of

advection within the radar image surrounding the area of interest. The result of this trade-off is that a region larger than the microscale area of interest needs to be chosen for the cross-correlation. This result is evident by careful inspection of the images in Figure 7-4.

4.2.2.2 Triangulation of Rain Gauge Data

A method of determining the advection velocity requires only a simple trigonometric computation. For example, note the cluster of three gauges shown in Figure 4-1. The advection time delay between gauges i and j can be formally found by performing a cross-correlation between the two:

$$\rho(\tau_{ij}) = \int R_i(t - \tau_{ij}) R_j(t) dt \quad (4.5)$$

where the maximum of $\rho(\tau_{ij})$ gives the best estimate of the time delay τ_{ij} . Equation (4.5) is approximately equivalent to simply measuring the time interval between correlated features of R_i and R_j , such as the rainfall rate peaks, as illustrated in Figure 4-2. The advection velocity can be estimated from the time delays determined from Equation (4.5), or by the graphical technique demonstrated in Figure 4-2:

$$\theta = \tan^{-1} \left\{ \frac{-\tau_{12}(x_3 - x_2) + \tau_{23}(x_2 - x_1)}{\tau_{12}(y_3 - y_2) + \tau_{23}(y_2 - y_1)} \right\} \quad (4.6)$$

$$\begin{aligned} u &= \frac{\cos \theta (x_2 - x_1) + \sin \theta (y_2 - y_1)}{\tau_{12}} \\ &= \frac{\cos \theta (x_3 - x_2) + \sin \theta (y_3 - y_2)}{\tau_{23}} \end{aligned} \quad (4.7)$$

where $\mathbf{u} = (u, \theta)$.

4.2.3 Interpolation of Radar Data

As described in the previous section, radar data can be represented as discrete time samples of two-dimensional functions of reflectivity data, $Z_n(x, y)$ where n is the time frame index and x and y are projections of the spherical coordinate data from three-dimensional space onto a two-dimensional ground coordinate system. The radar *base product* data are discrete samples of a volume scan $Z_n(x, y, z)$, where $Z_n(x, y)$ is calculated from a vertical composite of reflectivity, such as the maximum Z value in the z direction^[30]: $Z_n(x, y) = \underset{(z)}{\text{Max}}\{Z_n(x, y, z)\}$. Given $f(\mathbf{r}, nT) = Z_n(x, y)$, where T is the frame interval time (radar volume scan period), a solution to Equation (4.3) is:

$$f(\mathbf{r}, t) = Z_n(\mathbf{r} - \mathbf{u} t) \quad (4.8)$$

Radar data, in its original form, is not a continuous function of x and y . If an arbitrary area is considered, consisting of $k = 1 \dots N$ radar samples $\{x_{kn}, y_{kn}, Z_{kn}\}$ where x_{kn} and y_{kn} are the Cartesian coordinates of the projection of the reflectivity value Z_{kn} onto the x - y ground plane, Shepard's interpolation formula^[9] can be combined with Equation (4.8) for each time frame n :

$$Z_n(x, y, t) = \frac{\sum_{k=1}^N Z_{kn} \left((x - x'_{kn})^2 + (y - y'_{kn})^2 \right)^{-q}}{\sum_{k=1}^N \left((x - x'_{kn})^2 + (y - y'_{kn})^2 \right)^{-q}}, \quad t_n \leq t < t_{n+1} \quad (4.9)$$

$$x'_{kn} = x_{kn} + (t - t_n) u \cos \theta, \quad t_n \leq t < t_{n+1} \quad (4.10a)$$

$$y'_{kn} = y_{kn} + (t - t_n) u \sin \theta, \quad t_n \leq t < t_{n+1} \quad (4.10b)$$

where θ is the angle of \mathbf{u} measured from the x -axis so that $\mathbf{u} = (u, \theta)$. Note that a typical value^[9] for q is 2. Practical conditions on the choice of number of radar samples

N in Equation (4.9) is based on the requirement that the interpolated section should be well within the area enclosed by the $\{x_{kn}, y_{kn}\}$ coordinates.

In practice, Equation (4.9) must be *cross-faded* with consecutive radar frames $Z_n(x, y, t)$ and $Z_{n+1}(x, y, t)$ in order to prevent discontinuities in the interpolation due to the total time derivative term, \dot{Z}_n , which was ignored in the preceding derivation:

$$Z(x, y, t) = (1 - w(t)) Z_n(x, y, t) + w(t) Z_{n+1}(x, y, t), \quad t_n \leq t < t_{n+1} \quad (4.11a)$$

$$w(t) \equiv \frac{t - t_n}{t_{n+1} - t_n}, \quad t_n \leq t < t_{n+1} \quad (4.11b)$$

where $Z_n(x, y, t)$ and $Z_{n+1}(x, y, t)$ are determined from Equation (4.9) and Equations (4.10).

4.2.4 Interpolation of Rain Gauge Data

Rain gauge data can be treated as discrete spatial samples of a continuous time function of rainfall rate $R_j(t)$ where the j th gauge position is located at $\mathbf{r}_j = (x_j, y_j)$. Given $f(\mathbf{r}_j, t) = R_j(t)$, a solution^[12] to Equation (4.3) is:

$$f_j(\mathbf{r}, t) = R_j \left(t - \frac{(\mathbf{r} - \mathbf{r}_j) \cdot \mathbf{u}}{|\mathbf{u}|^2} \right) \quad (4.12)$$

Rain gauge data, in its original form, is not a continuous function of t . If a time sequence of rain rate data, consisting of $i = 1 \dots M$ samples $\{t_{ij}, R_{ij}\}$ where t_{ij} is the i th time at which the j th gauge acquires a rain rate sample of R_{ij} , Shepard's interpolation formula can be used with Equation (4.12) for each gauge location j :

$$R_j(x, y, t) = \frac{\sum_{i=1}^M R_{ij} |t - t_i|^{-p}}{\sum_{i=1}^M |t - t_i|^{-p}} \quad (4.13)$$

$$t_i = t_{ij} + \frac{\cos \theta (x - x_j) + \sin \theta (y - y_j)}{u} \quad (4.14)$$

where a value of $p = 3$ seems to produce good results, based on data presented in the following sections. The final interpolated rainfall rate is a superposition of the $R_j(x, y, t)$ from all L gauges of the network, again using Shepard's formula:

$$R(x, y, t) = \frac{\sum_{j=1}^L R_j(x, y, t) \left((x - x_j)^2 + (y - y_j)^2 \right)^{-q}}{\sum_{j=1}^L \left((x - x_j)^2 + (y - y_j)^2 \right)^{-q}} \quad (4.15)$$

4.2.5 RMS Gauge to Radar Error

In order to determine an optimum set of Z - R coefficients a and b in the standard Z - R power-law, $Z = a R^b$, a *root-mean-square* (RMS) error function can be defined, based on the differences between the j th rain gauge data and radar data (base scan or vertical reflectivity composite) above the j th gauge location:

$$E_j(a, b) = \left\{ \frac{1}{N} \sum_{n=1}^N \left[a R^b(x_j, y_j, t_n) - Z(x_j, y_j, t_n) \right]^2 \right\}^{1/2} \quad (4.16)$$

where again the interpolation formulas from Equations (11) and (15) are used. An RMS error function based on the *arithmetic average* of three gauge locations, for example, can also be defined as:

$$E_A(a, b) = \left\{ \frac{1}{N} \sum_{n=1}^N \left[\frac{1}{3} \sum_{j=1}^3 a R^b(x_j, y_j, t_n) - \frac{1}{3} \sum_{j=1}^3 Z(x_j, y_j, t_n) \right]^2 \right\}^{1/2} \quad (4.17)$$

And finally, an RMS error function can be defined, based on the *interpolated and spatially averaged* rain gauge and interpolated radar reflectivity:

$$E(a, b) = \left\{ \frac{1}{N} \sum_{n=1}^N \left[\frac{1}{A} \int_A a R^b(x, y, t_n) dA - \frac{1}{A} \int_A Z(x, y, t_n) dA \right]^2 \right\}^{1/2} \quad (4.18)$$

4.2.6 Gauge Spacing Considerations

The question of optimum gauge spacing can be addressed by examining the correlation of adjacent gauges as defined by Equation (4.5). This is graphically shown by superimposing rainfall rate plots from adjacent gauges, such as that shown in Figure 4-2. As the separation of gauges is increased, the time delay of correlated features of the rainfall rates also increases. As the separation continues to increase, the rates become uncorrelated so that it is no longer possible to identify related features and is therefore not possible to extract a physically meaningful time delay. Another way of looking at the question of gauge spacing is to compare the total time derivative term of Equation (4.1) to the advective term. When the spacing is small, the advective term dominates and Equation (4.3) is an approximation of the rainfall at adjacent gauge sites. Physically, the concept of gauge correlation is simply that the gauges should be far enough apart to get a good “view” of a single convective cell as it passes over a gauge cluster site. When the distance is too large, adjacent gauge sites are no longer measuring the same convective cell. These qualitative specifications for spacing are very dependent on the extent of the convective cells within a storm system. The best strategy is to find a spacing small enough to satisfy these requirements for most storm systems, while maintaining the

maximum separation possible. Based on the results presented in this work, a recommended spacing is 0.5 to 2 km. These distances are based on Florida summer thunderstorm characteristics, and may be different for other locations and time of year.

4.3 Experimental Results

The data that will be used to demonstrate the concepts from the previous section was acquired on June 14, 1997, 18:00 through 18:40 UTC at Kennedy Space Center (KSC). Three TRMM/KSC rain gauges were used for this analysis, corresponding to site numbers 017, 018, and 020. The gauges are tipping buckets (manufactured by Qualimetric), physically located at the lightning detection sites as shown on the map of Figure 4-3. The circle surrounding the gauges in Figure 4-3 is the interpolation area used to process and compare the gauge and radar data. The corresponding radar is from the Melbourne WSR-88D (KMLB) station, approximately 50 km to the south of the study area.

Using the rain gauge interpolation formula, Equation (4.15), $R(x_j, y_j, t)$ for the three TRMM/KSC gauges is plotted in Figures 4-4, where $j = 1, 2, 3$ corresponds to locations of gauges 017, 018, and 020. The rain rate in Figures 4-4 is essentially the raw tipping bucket data interpolated in time using a constant sample interval of $\Delta t = t_n - t_{n-1} = 60$ s. Also shown in Figures 4-4 is the interpolated NWS radar reflectivity, $Z(x_j, y_j, t)$, using Equations (4.11) and the lowest elevation scan data (base scan, 0.5° elevation), and again applying a sample interval of $\Delta t = 60$ s.

4.3.1 Interpolation of Gauge and Radar Rainfall Rates

Figures 4-5 show $\Delta t = 120$ s time frame intervals of gauge and radar rainfall over the study area surrounding the three TRMM gauge sites at KSC, using Equations (4.11) for radar interpolation, as well as Equation (4.15) for gauge interpolation (Figure 4-5b).

The radar reflectivity data is converted to rainfall rate in Figure 4-5a by inverting the standard form of the Z - R power-law relation, $Z = a R^b$, whose parameters are obtained from a minimization of the RMS function specified by Equation (4.18). In this specific example, the RMS method results in $a = 60$ and $b = 1.7$. (The most commonly accepted Z - R parameter values are $a = 300$ and $b = 1.4$, obtained from a very large ensemble of data points, averaging the statistical fluctuations that occur during a single rainfall event). Rainfall rate is shown in units of mm h^{-1} on a logarithmic scale versus color. Dark green, on the low end of the scale, represents 0.3 mm h^{-1} ; yellow is 17 mm h^{-1} ; while dark red on the upper end is 90 mm h^{-1} .

4.3.2 Gauge to Radar Comparisons

Two methods of comparing radar to gauge rainfall will be considered. First, a linear regression method will be used to find the optimum Z - R coefficients a and b for each TRMM/KSC gauge site studied. For comparison, the RMS error functions discussed in Section 4.2.5, will be used to find an optimum set $\{a, b\}$ for the three cases specified by Equations (4.16), (4.17), and (4.18). Based on these results, the radar rainfall rate will be calculated over the corresponding gauge site, making use of the radar interpolation method presented in Section 4.2.3.

4.3.2.1 Linear Regression

Determining the coefficients a and b of the Z - R power-law $Z = aR^b$ can be performed by fitting the measured data points of $\log Z$ and $\log R$ to a straight line:

$$y = y_0 + m x \quad (4.19)$$

where $y = \log Z$, $x = \log R$, $a = 10^{y_0}$, and $b = m$. This curve fitting procedure is often referred to as *linear regression* for historical reasons. For a set of N data points (x_i, y_i) , the following sums can be defined:

$$\begin{aligned}
 S &\equiv \sum_{i=1}^N 1 = N & S_x &\equiv \sum_{i=1}^N x_i \\
 S_y &\equiv \sum_{i=1}^N y_i & S_{xx} &\equiv \sum_{i=1}^N x_i^2 \\
 S_{yy} &\equiv \sum_{i=1}^N y_i^2 & S_{xy} &\equiv \sum_{i=1}^N x_i y_i
 \end{aligned} \tag{4.20}$$

Standard linear regression results in solutions for y_0 and m :

$$y_0 = \frac{S_{xx} S_y - S_x S_{xy}}{S S_{xx} - S_x^2} \tag{4.21a}$$

$$m = \frac{S S_{xy} - S_x S_y}{S S_{xx} - S_x^2} \tag{4.21b}$$

Equations (4.21) are the result of minimizing the χ^2 error defined as:

$$\chi^2(y_0, m) = \sum_{i=1}^N (y_i - y_0 - m x_i)^2 \tag{4.22}$$

The preceding procedure minimizes the vertical distance between the data point y_i and the calculated point $y(x_i)$. The implication of this method is that all of the error in the data is contained in y_i . If the error is assumed to be equally distributed among both x_i and y_i , an alternate procedure is to minimize the perpendicular distance between (x_i, y_i) and the line $y = y_0 + m x$. In this case, the χ^2 error is defined as:

$$\chi^2(y_0, m) = \sum_{i=1}^N \frac{(y_i - y_0 - m x_i)^2}{1 + m^2} \quad (4.23)$$

The new solutions for y_0 and m are now:

$$m = \frac{-\Gamma + \sqrt{\Lambda^2 + \Gamma^2}}{\Lambda} \quad (4.24a)$$

$$y_0 = \frac{S_y - m S_x}{S} \quad (4.24b)$$

where,

$$\Gamma \equiv S S_{xx} - S_x^2 - S S_{yy} - S_y^2 \quad \Lambda \equiv 2 (S S_{xy} - S_x S_y) \quad (4.24c)$$

Figures 4-6 show linear regression results for each of the three gauges under study at the TRMM/KSC sites. The standard linear fit according to Equations (4.21), summarized in Table 4-1, results in a lower slope (smaller b) than does the regression fit based on Equations (4.24), summarized in Table 4-2. Based on these results, the standard fit agrees better with $Z-R$ parameters based on NWS operations standards^[29] where $a = 300$ and $b = 1.4$.

Table 4-1. Z-R parameters based on standard linear regression from Figures 4-6 and Equations (4.21)

Gauge Site No.	a	b
017	55	1.8
018	98	1.5
020	87	1.3

Table 4-2. Z-R parameters based on linear regression from Figures 4-6, using Equations (4.24).

Gauge Site No.	a	b
017	39	2.1
018	61	1.8
020	24	1.9

4.3.2.2 RMS Error

Plots of $E_j(a, b)$ for $j = 1, 2,$ and $3,$ from Equation (4.16) are shown in Figures 4-7a, 4-8a, and 4-9a. Note that N in Equation (4.16) is the number of $\Delta t = 60$ s time intervals plotted in Figures 4-4. These RMS error plots immediately reveal an error surface minimum, representing the optimal choice of the $Z-R$ coefficients a and $b.$ When the optimal $Z-R$ coefficients from Figures 4-7a, 4-8a, and 4-9a are used to calculate radar rainfall rate from interpolated reflectivity data above the j th gauge, the best possible match, in a *least squares* sense, results. Figures 4-7b, 4-8b, and 4-9b are the corresponding plots of radar rainfall compared to the gauge rainfall, using the $Z-R$ parameters determined from the RMS error surface minimum, as summarized in Table 4-3. As shown by comparing Tables 4-1 and 4-3, the RMS surface minimums agree with the linear regression results, within plotting quantization error of the RMS surface plots.

Table 4-3. $Z-R$ parameters based on RMS error surfaces from Figures 4-7 through 4-9.

Gauge Site No.	a	b
017	60	1.8
018	100	1.5
020	90	1.3

A plot of $E_A(a, b),$ based on Equation (4.17) for the data of Figures 4-4, is shown in Figure 4-10a. For comparison, a plot of $E(a, b),$ based on Equation (4.18) is shown in Figure 4-10b. The optimum a and b found from the corresponding RMS error surface minimums are summarized in Table 4-4. Based on Table 4-4, the spatial average method, based on Equation (4.18), results in a similar set of $Z-R$ parameters as found from the *arithmetic average* method of Equation (4.17). However, when comparing the error

surface minimum values in Table 4-5, it is clear that the spatial average error function $E(a, b)$ results in a choice of Z - R parameters which yield the minimum RMS error.

Table 4-4. Z - R parameters based on RMS error surface minimums of Figures 4-10.

RMS Type	a	b
Arithmetic Average $E_A(a, b)$	60	1.68
Spatial Average $E(a, b)$	60	1.72

Table 4-5. Comparison of RMS error surface minimum values and Z - R parameters.

RMS Type	a	b	E_{min} dBz
Gauge Site #017 $E_1(a, b)$	60	1.80	2.05
Gauge Site #018 $E_2(a, b)$	100	1.48	2.75
Gauge Site #020 $E_3(a, b)$	90	1.32	3.69
Arithmetic Average $E_A(a, b)$	60	1.68	1.75
Spatial Average $E(a, b)$	60	1.72	1.03

A conclusion from these results is that the spatial average method of gauge to radar comparison $E(a, b)$, reduces many of the errors associated with single point comparisons. Even though the arithmetic average function $E_A(a, b)$ may result in similar Z - R parameters, the reliability of the results may be less than those based on spatial averages, due to the larger RMS error.

Figure 4-11a shows comparison of the minimum RMS error based on the June 14, 1997, KSC data, identical to the E_{min} data summarized in Table 4-5. Figures 4-11b and

4-11c show similar comparisons for two other rainfall events. It is clear from these graphs that the spatial averaging method results in a choice of $Z-R$ parameters which yield the minimum RMS error.

4.4 Applications and Discussion

An algorithm for combining and interpolating rain gauge data for the purpose of real-time rainfall mapping has been proposed, based on an advection transformation and Shepard's formula. Preliminary data provides evidence that this interpolation processing scheme can lead to improved mapping of areal rainfall over microscale gauge networks. By integrating the spatially interpolated gauge and radar rainfall rates over microscale gauge clusters, the effects of advection and gravitational sorting of drops are reduced so that accurate areal average rainfalls may be generated with high temporal resolution. This method of gauge to radar comparison is suggestive of the *Window Probability Matching Method*^[31], but in this case both the gauge and radar are windowed in space.

In applications for TRMM Ground Validation (GV), where only single gauges are available (gauge separation > 5 km, which is the predominant case of gauge network placement), analysis suggests that an interpolation over single gauge points (actually, an *extrapolation*) may also lead to better gauge to radar comparisons. Figures 4-12a and 4-12b show examples of gauge extrapolation, using Equation (4.15) with $N = 1$, over a single gauge site in Satellite Beach, FL. Note that the horizontal scales are in units of min, which is the spatial extent of interpolation scaled by the inverse of advection velocity. Knowing an estimate of the total time rate of change of rainfall from the corresponding radar measurements, a time constant τ can be approximated corresponding to a $1/e = 37\%$ change, for example, in the radar reflectivity over the gauge site. A distance corresponding to τ along the horizontal axis of Figures 4-12 from

the gauge location, gives some quantitative definition of an area of extrapolation around the gauge site.

UNIVERSITY OF TORONTO LIBRARY

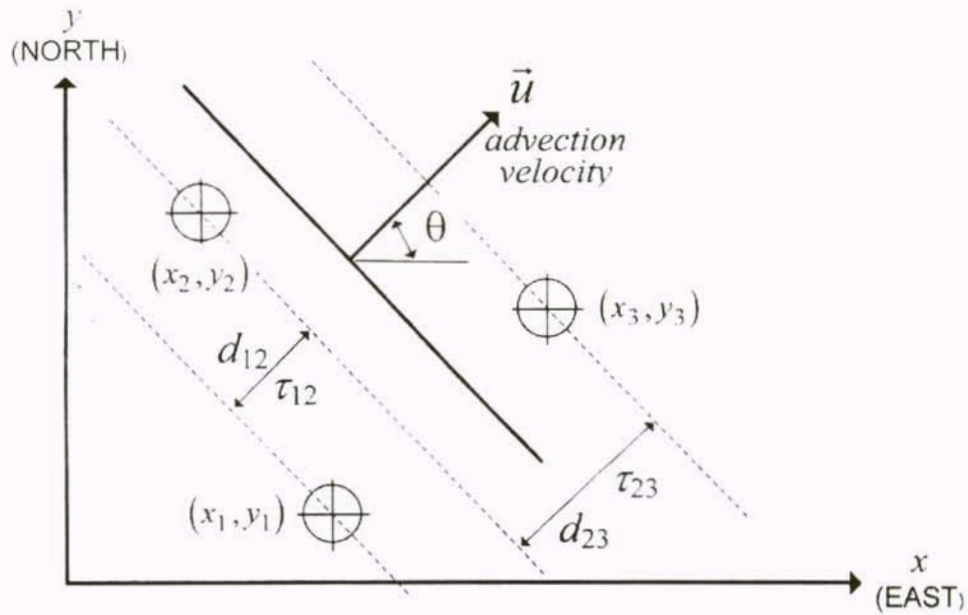


Figure 4-1. Determination of advection velocity \mathbf{u} from adjacent gauges using triangulation.

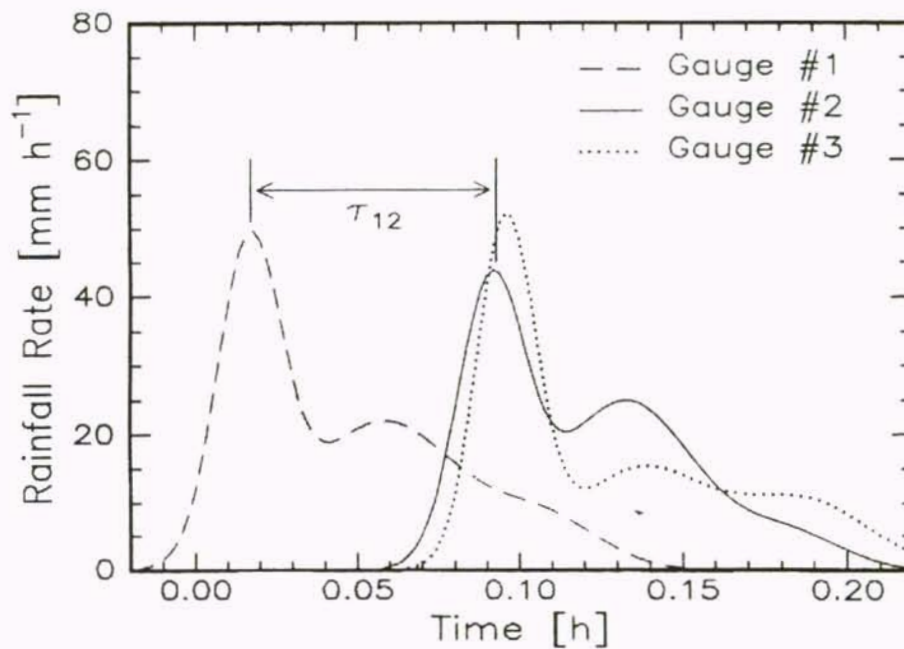


Figure 4-2. Three adjacent gauges showing delay time between correlated features of rainfall rate.

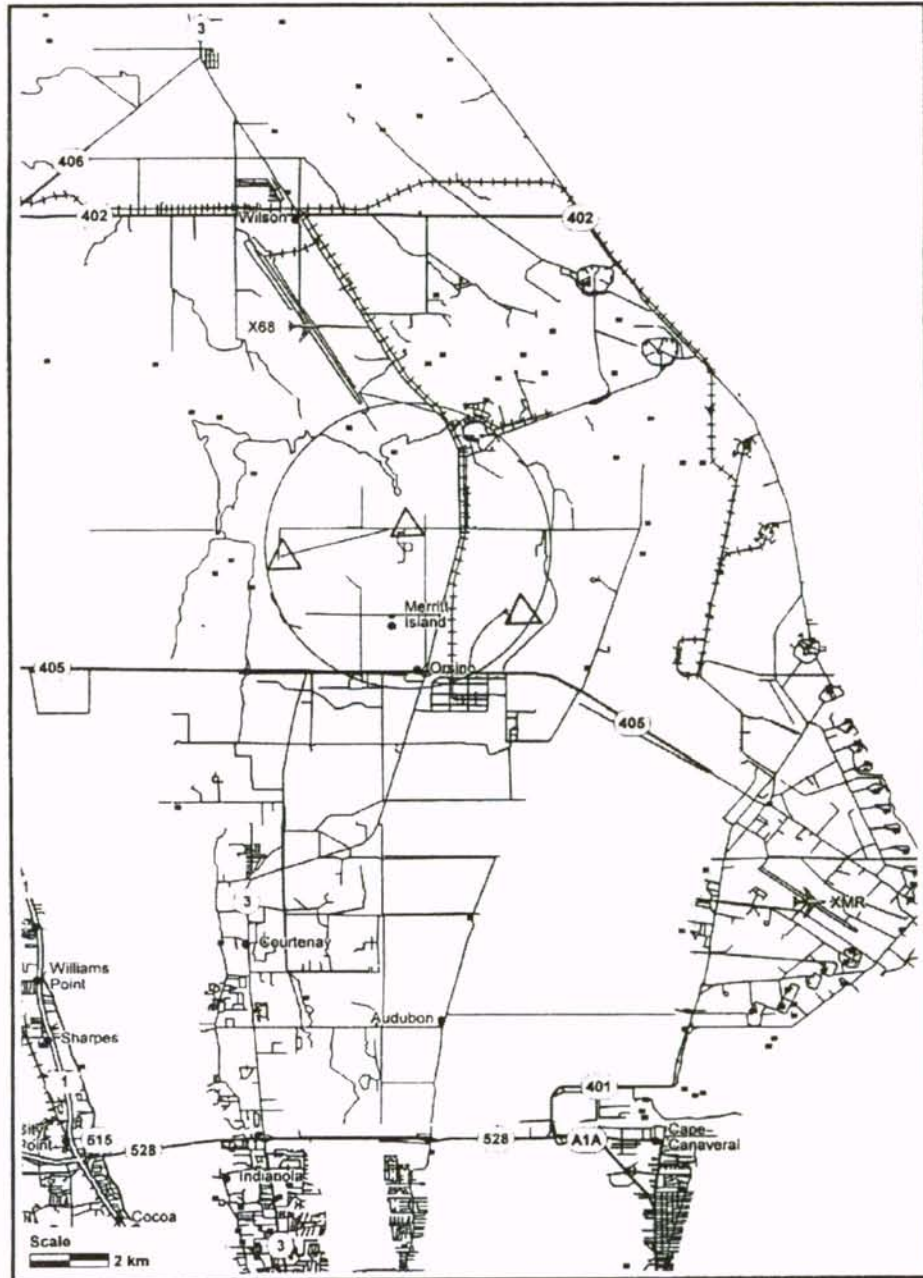


Figure 4-3. Map of TRMM/KSC gauge test site.

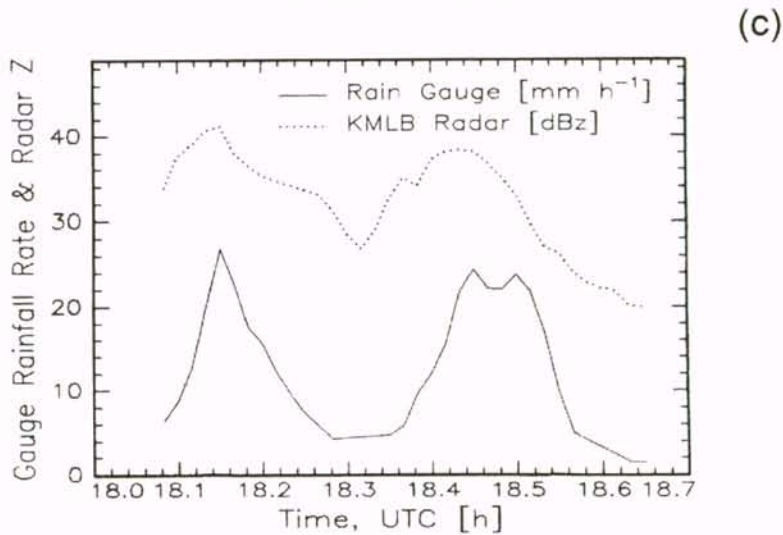
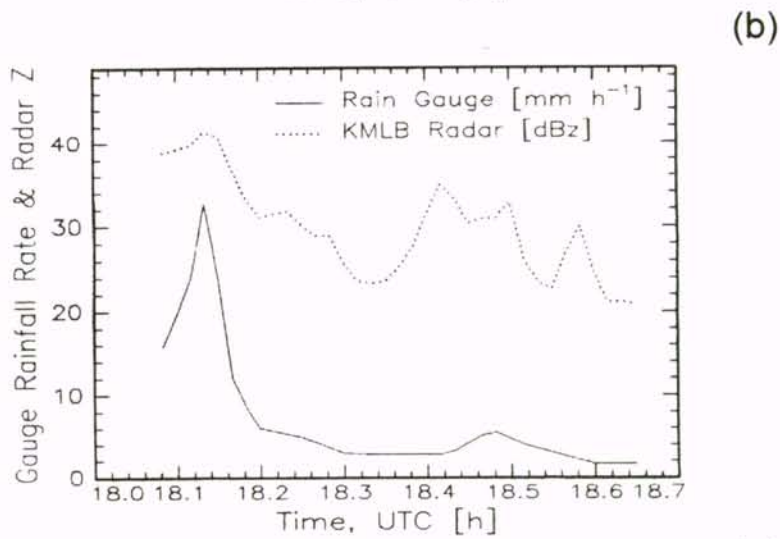
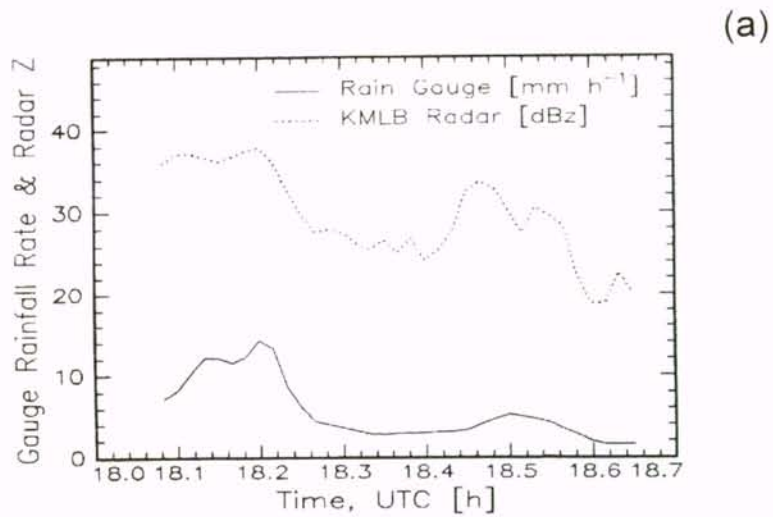


Figure 4-4. TRMM/KSC rain gauge and Melbourne NEXRAD interpolated data, June 14, 1997; (a) Gauge 017, (b) Gauge 018, (c) Gauge 020.

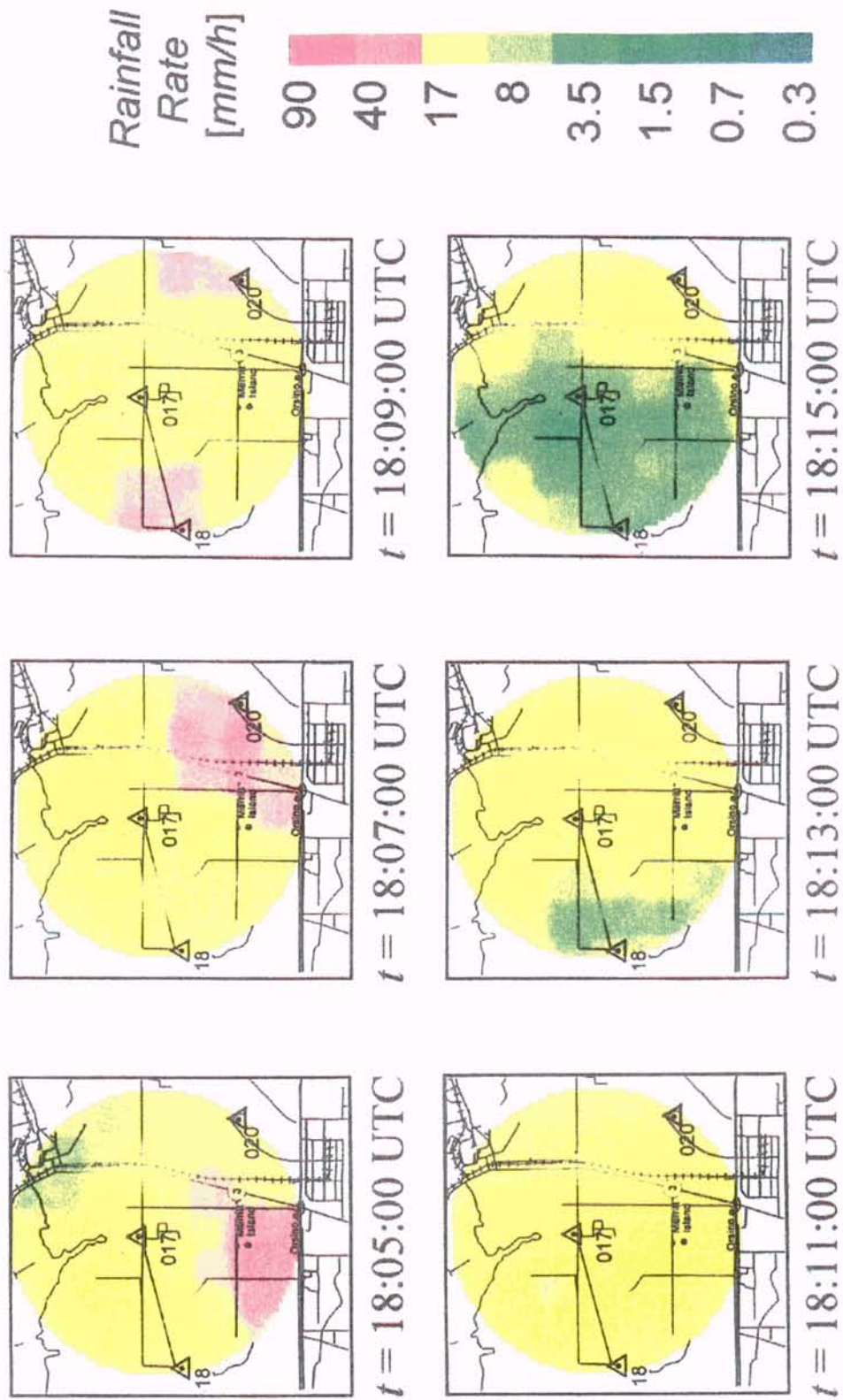


Figure 4-5a. Interpolated radar rainfall, based on Melbourne NEXRAD data of June 14, 1997, over KSC.

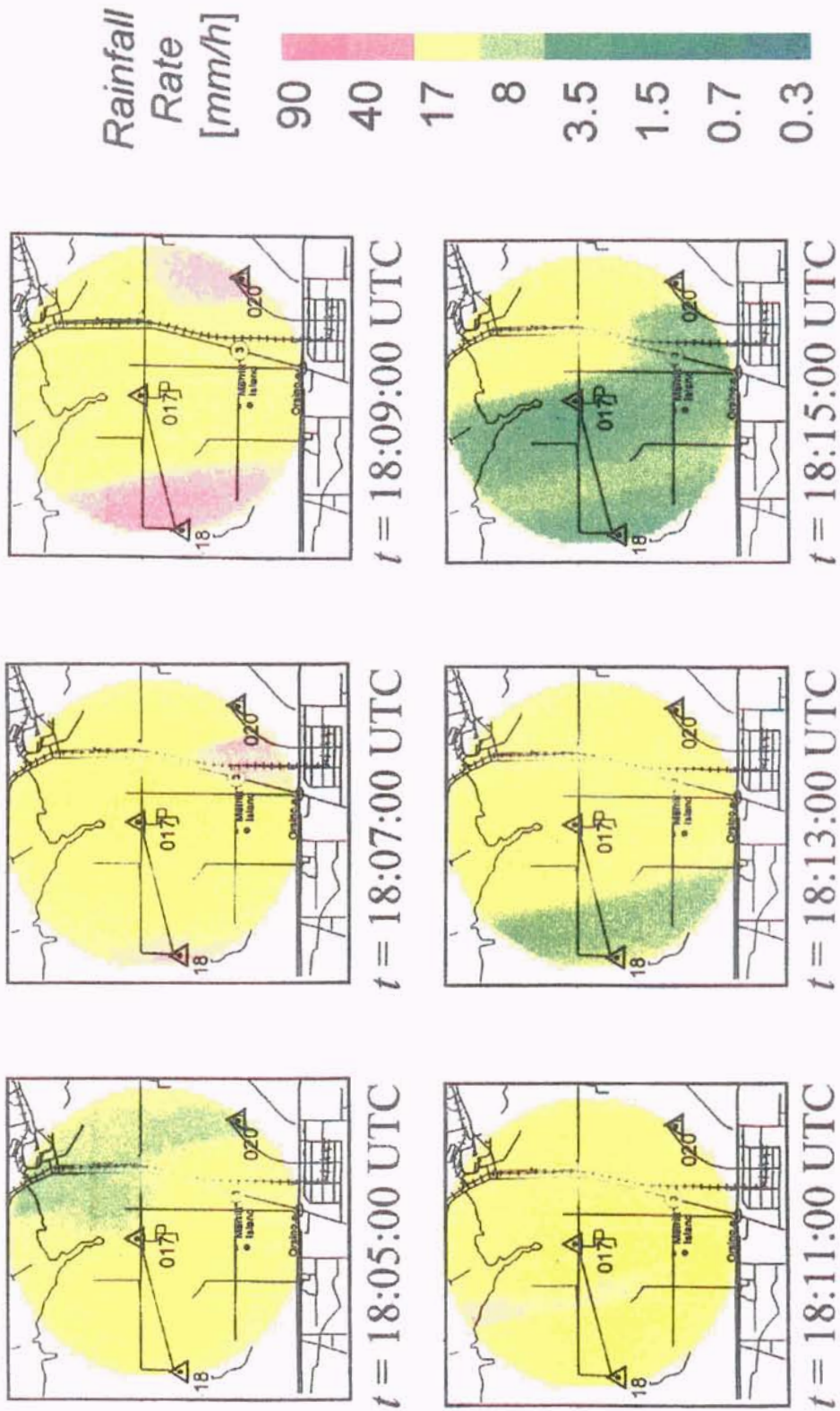


Figure 4-5b. Interpolated gauge rainfall, based on TRMM rain gauge data of June 14, 1997 over KSC.

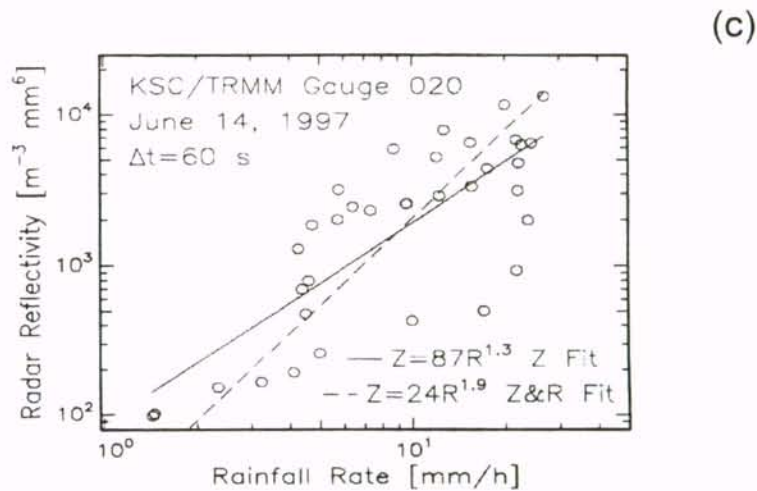
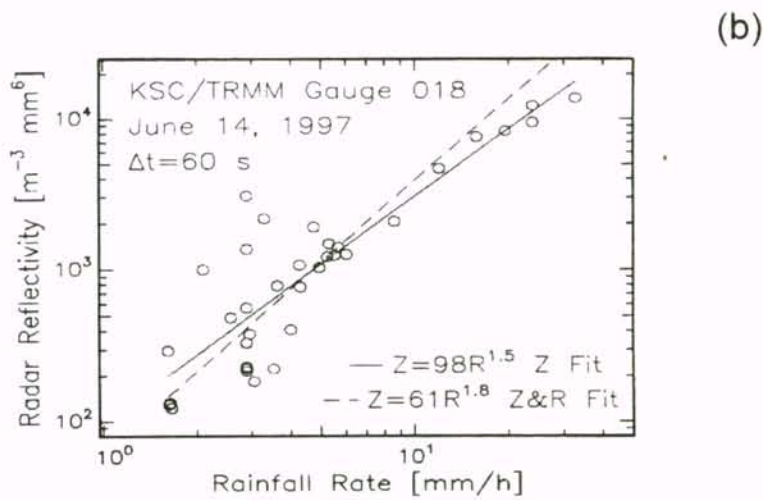
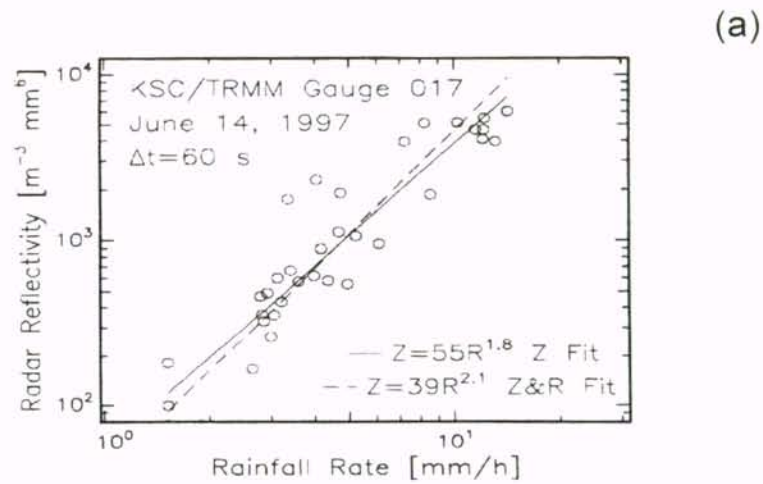


Figure 4-6. Linear regression of $\log Z$ versus $\log R$ of interpolated data, where solid line is a standard linear fit based on Equations (4.21) and dashed line is a fit based on Equations (4.24); (a) gauge site 017 with correlation coefficient $r = 0.93$, (b) gauge site 018 with $r = 0.88$, (c) gauge site 020 with $r = 0.79$.

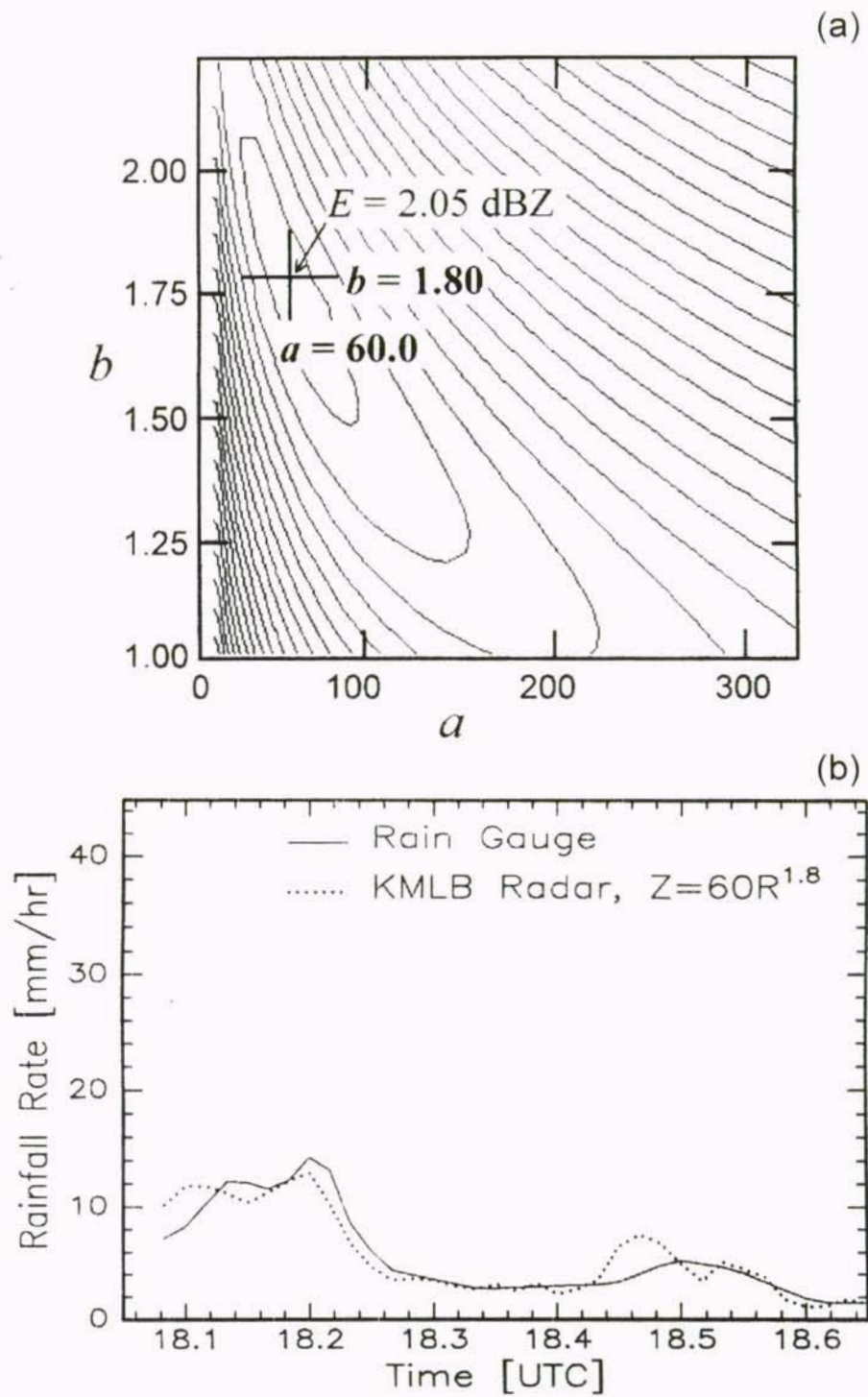


Figure 4-7. TRMM/KSC gauge site 017, June 14, 1997; (a) RMS error surface from Equation (4.16), (b) radar rainfall (dotted line) from Z - R parameters $a = 60$ and $b = 1.80$, determined from RMS error surface minimum, compared with gauge rainfall rate (solid line).

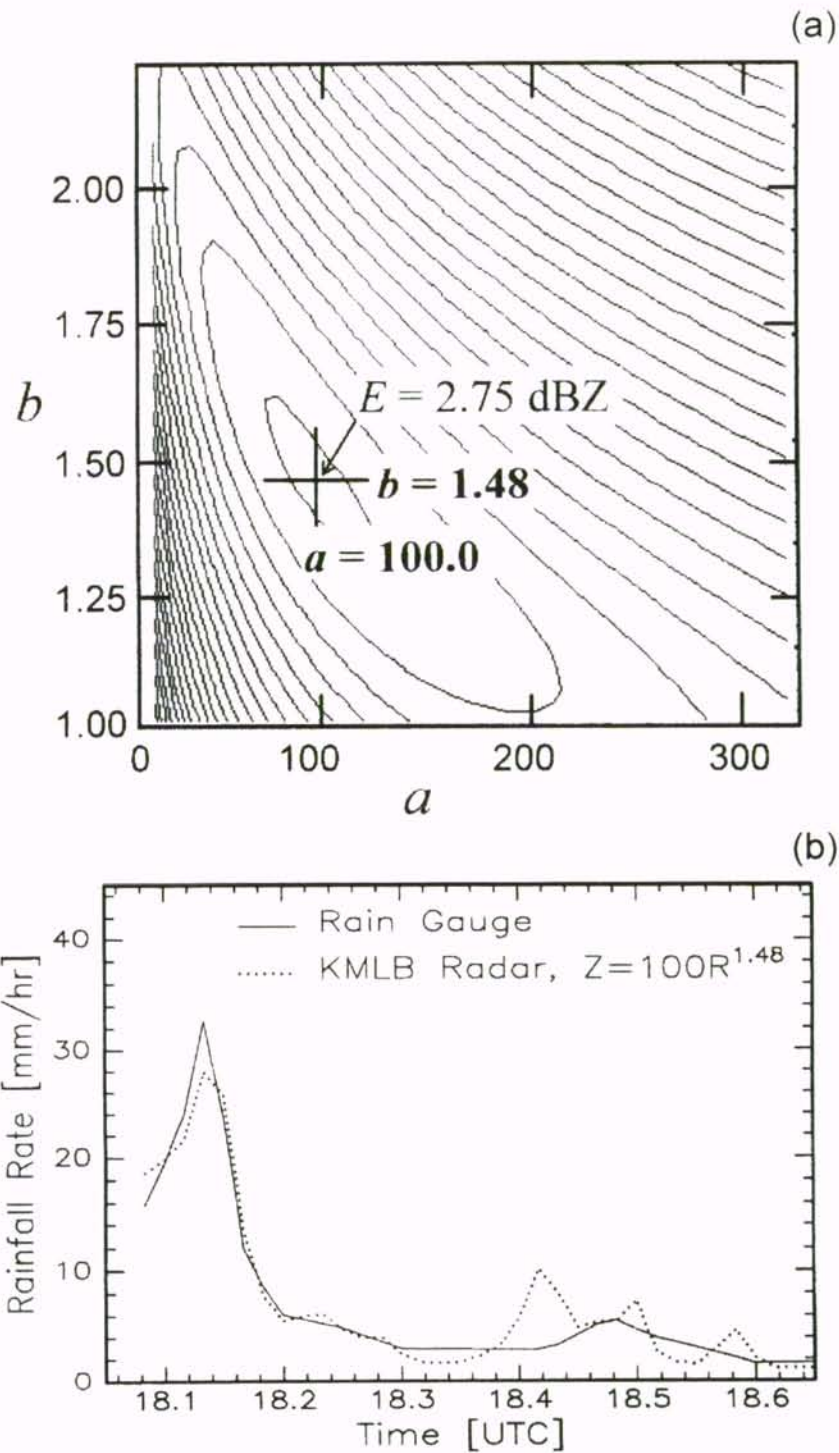


Figure 4-8. TRMM/KSC gauge site 018, June 14, 1997; (a) RMS error surface from Equation (4.16), (b) radar rainfall (dotted line) from Z - R parameters $a = 100$ and $b = 1.48$, determined from RMS error surface minimum, compared with gauge rainfall rate (solid line).

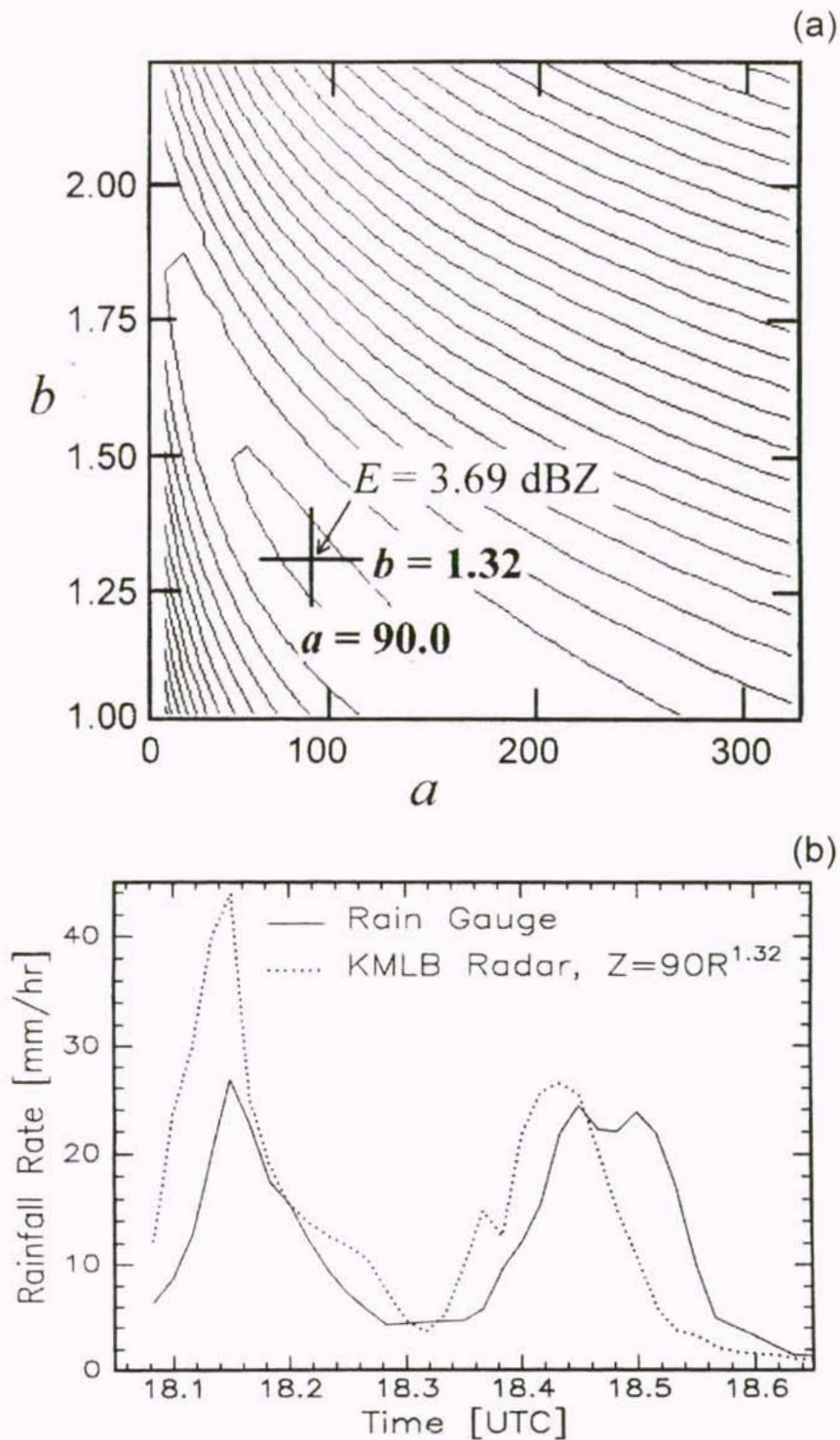


Figure 4-9. TRMM/KSC gauge site 020, June 14, 1997; (a) RMS error surface from Equation (4.16), (b) radar rainfall (dotted line) from Z - R parameters $a = 90$ and $b = 1.32$, determined from RMS error surface minimum, compared with gauge rainfall rate (solid line). (Note the time delay in (b) between gauge and radar data, which is most likely due to advection and/or the fall time of drops above the gauge).

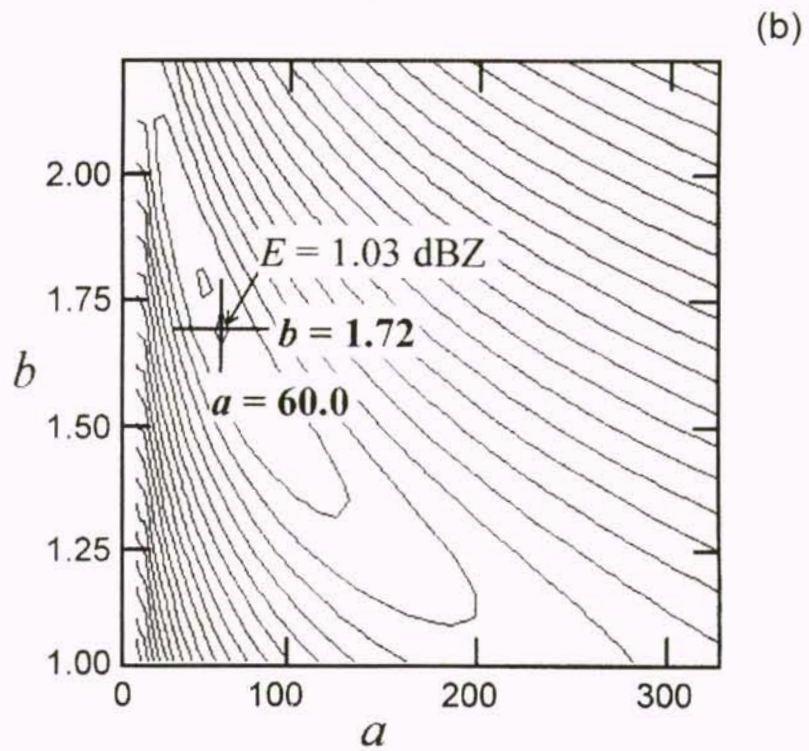
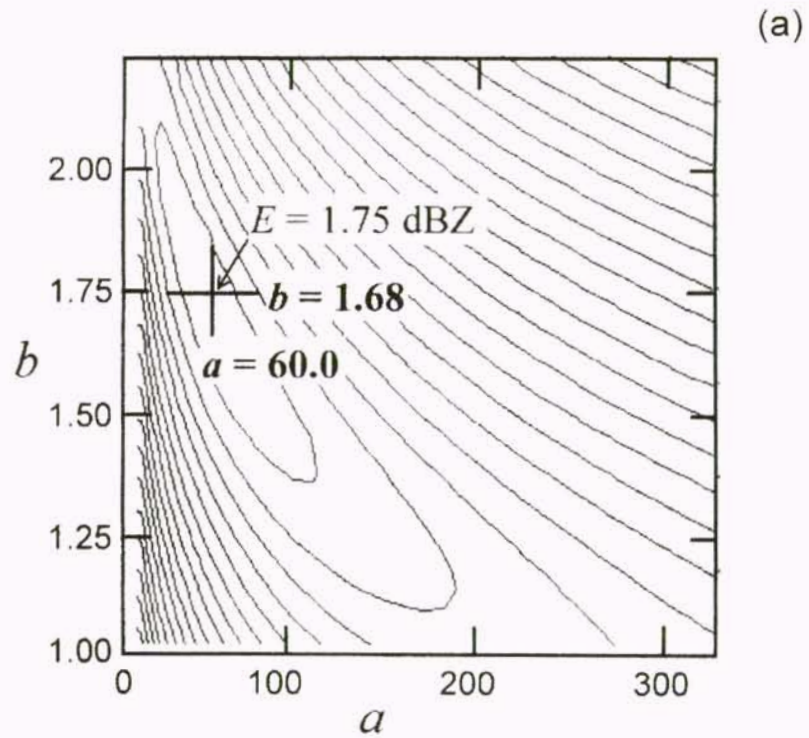


Figure 4-10. RMS error functions and corresponding Z-R parameter solutions based minimum of error surfaces; (a) arithmetic average RMS error $E_A(a, b)$, based on Equation (4.17), (b) spatial average RMS error $E(a, b)$, based on Equation (4.17).

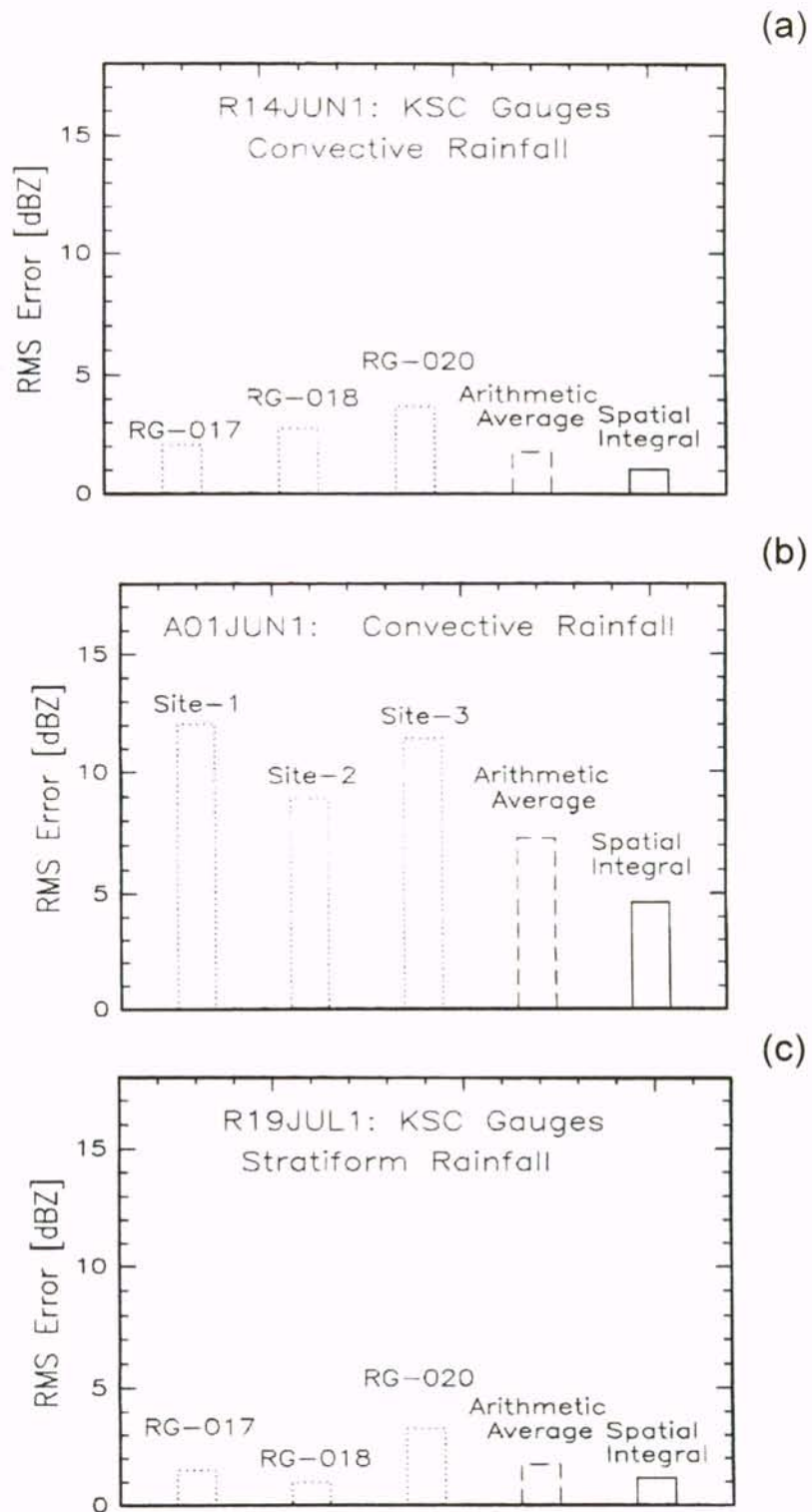


Figure 4-11. Comparisons of RMS error minimums determined from Equations (4.16), (4.17), and (4.18) for different locations and times; (a) KSC - June 14, 1997, (b) Palm Bay, FL - June 1, 1997, (c) KSC - July 19, 1997.

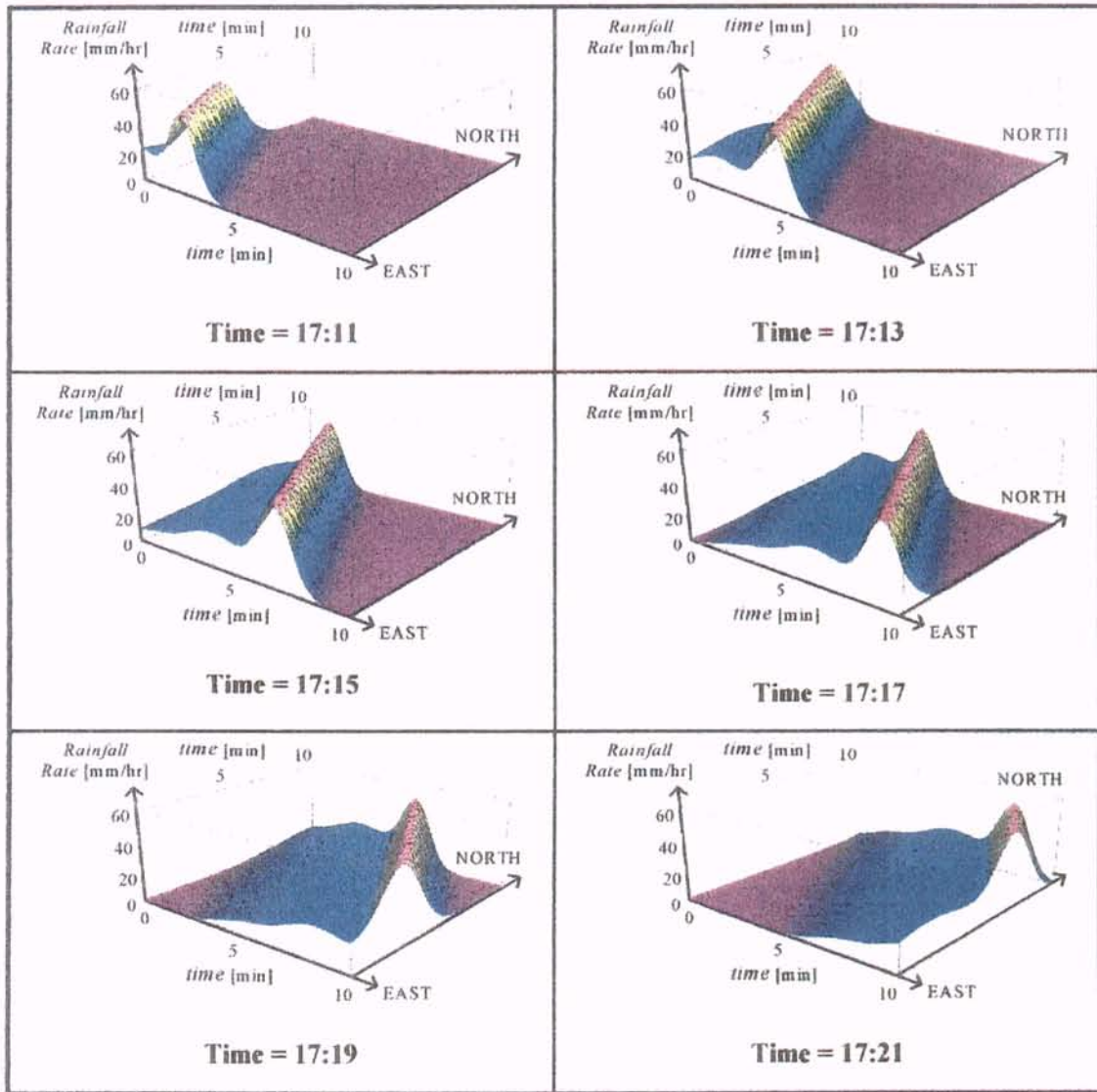


Figure 4-12a. Spatially interpolated rainfall rate from a single gauge, Satellite Beach, FL, June 9, 1996, using Equation (4.15) with $N = 1$. Advection velocity $u \approx 11$ m/s.

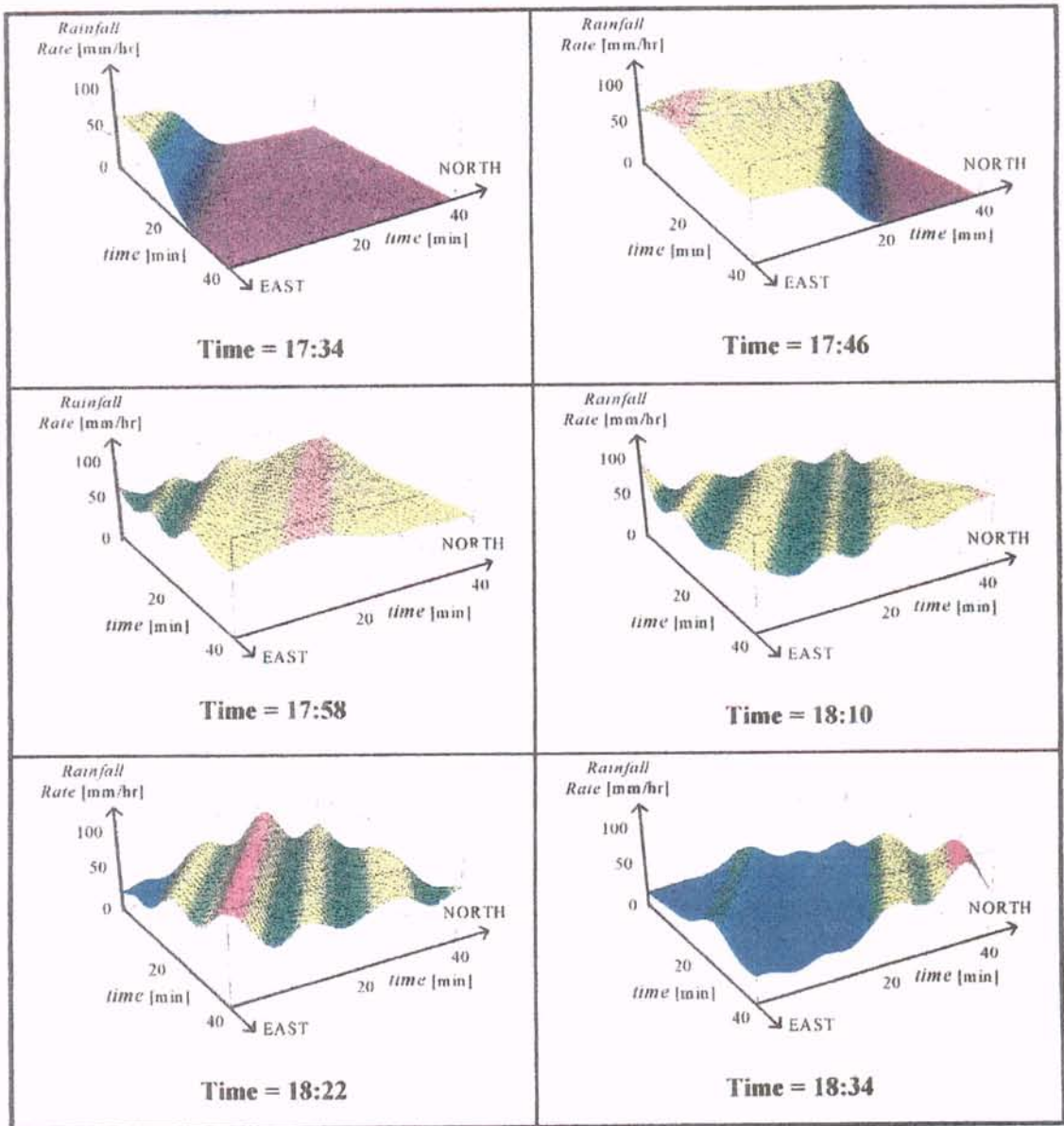


Figure 4-12b. Spatially interpolated rainfall rate from a single gauge, Satellite Beach, FL, June 28, 1996, using Equation (4.15) with $N = 1$. Advection velocity $u \approx 9.5$ m/s.

CHAPTER 5

ALGORITHMS FOR PROCESSING DISDROMETER DATA

5.1 Background

Impact disdrometers are the class of rainfall measurement instruments for recording individual raindrop impacts. These instruments convert the impact of a single water drop at terminal velocity to an electrical impulse. The disdrometer's processing electronics is responsible for converting the impulse amplitude to an equivalent drop diameter. The relationship between electrical signal amplitude and drop diameter is dependent on the various physical mechanisms which couple the drop momentum or impulsive force to the mechanical portion of the sensing element. Most impact disdrometers transform drop momentum to an electrical output by a direct coupling of the sensor mass to the sensor transducer^[11,32]. These instruments can sometimes be modeled as a simple spring-mass system where the sensor mass reacts to the impulsive force of the drop impact. In other cases, the appropriate model may be a two-dimensional drum-head. The sensing element of the Acoustic Rain Gauge Array, is similar in principle to previous impact disdrometers except that in this case, the drop impact impulse is acoustically coupled through air to the transducer^[12].

The calibration of impact disdrometers has traditionally been a tedious process, whereby known diameter single water droplets are generated and allowed to fall from a height of 10 m or more in order to obtain terminal velocity. An alternate method of calibration is proposed which eliminates the need of a single drop generator and associated drop shaft. The strategy behind this technique is to use an accumulation rain

measurement instrument, such as a tipping bucket rain gauge, to provide a known signal for the purpose of training an adaptive calibration algorithm. The reference signal to this digital signal processing algorithm is the output of the impact disdrometer which is preprocessed by an impulse amplitude estimation algorithm. This calibration technique has been evaluated using data from UCF's Acoustic Rain Gauge Array, which estimates raindrop size distributions (1.0 mm drop diameter or more) by digitally sampling the acoustic signal from an array of acoustic impact sensors. This calibration technique should be applicable for use with other impact disdrometers.

Partially spurred by the advent of radar, an extensive amount of experimental and theoretical work was performed during the 1940s to analyze rainfall. The main thrust of that research was to describe and characterize rain as a volume density distribution of water droplets, where the number of drops in a volume of air as a function of drop size is defined as the drop size distribution^[16]. Since that time, interest in characterizing rain from this perspective has continued^[33,34]. Weather radar remains the primary motivation in rainfall DSD measurements, although, there are many other reasons to study DSDs, especially as a function of time and surface coordinates^[12].

Even though impact disdrometers^[10] were originally developed to measure rainfall rate, they have since been used to estimate rainfall DSD functions by counting and measuring the individual raindrop impacts on a measurement surface. These instruments convert the collision of a single water drop (assumed at terminal velocity) with the sensing surface to an electrical impulse. The impact disdrometer's processing electronics is then responsible for converting the impulse amplitudes to equivalent drop diameters, even though it has been found that these instruments are seldom reliable below drop size diameters of 1 or 2 mm^[35]. Impact disdrometers can nevertheless contribute to the understanding of cloud physics, hydrology, and numerous other fields which require knowledge of detailed rainfall characteristics.

5.2 UCF Acoustic Disdrometer

Most impact disdrometers transform a drop impulse to an electrical output by a direct coupling of the drop impulse to the sensor transducer. UCF's Acoustic Rain Gauge Array^[12] (ARGA) sensor is similar to previous impact disdrometers, except that in this case, the drop impulse is acoustically coupled through air. By incorporating low-cost components, off-the-shelf hardware, and custom software, the ARGA disdrometer can be implemented as an array of sensors at a lower cost than most single disdrometers. Since the sensors are acoustic in nature, other useful applications may be implemented by simply downloading application specific software to the programmable hardware. In this way, ARGA can possibly be used as a wind measurement system for severe weather events such as a tornado, for example.

Referring to Figure 5-1, the sensing element consists of a balsa wood diaphragm, 12 cm in diameter and coated with a waterproof sealant, which acts like a highly damped drum head (resonant frequency of the diaphragm is about 530 Hz). The foam sleeve is used to suppress impulses from drop impacts on the side of the sensor housing. Figure 5-2 is an example plot of the digitally sampled output of the acoustic sensor, with sample frequency $f_s = 11025$ Hz, while acquiring data during a typical Florida thunderstorm. Note that the impulse width is on the order of 10 ms. The dead-time, equal to the pulse width, is comparable to that of previous impact disdrometers^[36].

Figure 5-3 shows a block diagram of the acoustic sensor's digital signal processing algorithm section. The primary DSP functions are: (1) signal filtering, (2) peak detection and amplitude estimation, and (3) drop size diameter conversion. The filtering is accomplished by a 16th order bandpass filter centered around the resonant frequency of the sensor diaphragm $f_0 = 530$ Hz, with a bandwidth of 375 Hz. The amplitude estimation algorithm incorporates any necessary dead-time by recognizing characteristics in the pulse which may correspond to impulse overlap. The peak detection and amplitude

estimation algorithms are based on simple pattern recognition principles. The drop size conversion is accomplished by an empirical drop impulse to drop diameter, based on a set of parametric coefficients determined by an adaptive calibration algorithm. During a rainfall event, all impulses over the sensor's measurement area, and within a time frame interval T (for example, $T = 30$ s), are measured, converted to equivalent drop volumes, and presented as rainfall rate or an estimation of the DSD function $N(D)$ (for diameters greater than 1 mm).

5.3. Calibration

Since disdrometers measure the voltage output resulting from the impact of a raindrop, a calibration is necessary to convert peak impulse voltages to the equivalent drop size diameters. Two methods will be discussed: traditional *single drop* calibration; and UCF's method of *adaptive* calibration (this method is also referred to as an *in situ* calibration).

5.3.1 Single Drop Calibration

Single drop generators, designed and built by the NOAA Atlantic Oceanographic and Meteorological Laboratory (AOML) in Miami^[36], are shown in Figures 5-4. In these apparatus, a water reservoir is attached to a needle valve which controls the flow rate through different diameter copper tubing. For larger raindrop sizes of 2.5 - 5.5 mm diameter (Figure 5-4a), water is allowed to drip off the end of copper tubing of various inner diameters ranging from 0.2 to 5 mm. The relationship between tube diameter and drop size is shown in Figure 5-5a. Flow rate does not affect drop size, as long as individual drops are allowed to form at the tube tip. Drop sizes are determined by weighing 100 drops for each tube size in groups of 20 drops each.

In order to generate smaller drop sizes, the individual drops must be actively knocked off of the tube tip. To accomplish this, the smallest diameter tubes were mounted onto an audio speaker (Figure 5-4b), driven by a sine wave of variable frequency. By varying the frequency of the sine wave driver, drop sizes from 0.6 - 2 mm diameter can be created as shown in Figure 5-5b. Drop sizes were determined by collecting 15 - 20 individual drops on a water repellent surface and then measuring their diameter using precision calibrated optical magnifying lenses. The drop sizes are verified before each experimental run because the relationship between drop size and driver frequency is not generally stable.

Drops are allowed to fall five stories in an internal stairwell, since the largest 5.5 mm drops need approximately 12 m in order to obtain terminal velocity. For small drop sizes, a shorter fall height of 4.5 m can be used to assure that the drops hit the sensor surface, since small drops exhibited significant horizontal drift as they fell. Peak voltage for approximately 100 drop impacts for each of 15 drop sizes ranging from 0.6-5.5 mm diameter are collected. Spurious data points (low voltage values) due to drop breakup, near misses, spatter, and noise are removed subjectively. The result is a calibration curve, yielding drop diameter as a function of peak instrument voltage.

5.3.2 Tipping Bucket as a Reference Signal

An alternate method of calibration^[37], based on the numerical minimization of a function, is now proposed. This technique is similar to many well known adaptive signal processing algorithms. The strategy behind this technique is to use a tipping bucket rain gauge for providing reference data to optimize a set of adaptive coefficients $\alpha_0, \alpha_1, \dots, \alpha_{L-2}$, and β . An error surface defined by Equation (5.1), is the sum of the square of the differences between the tipping bucket output $V(n-k)$ and the calculated $\hat{V}(n-k)$ for the current and previous $N-1$ time frame intervals:

$$\begin{aligned}
E(n) &= \sum_{k=0}^{N-1} [V(n-k) - \hat{V}(n-k)]^2 \\
&= \sum_{k=0}^{N-1} [V_0 - \hat{V}(n-k)]^2
\end{aligned} \tag{5.1}$$

$$\hat{V}(n) = \sum_{m=1}^{M_n} \hat{v}_m(n) \tag{5.2}$$

$$\hat{v}_m(n) = \sum_{k=0}^{L-2} \alpha_k x_m^{k\beta}(n) \tag{5.3}$$

where $x_m(n)$ is the amplitude of the m th drop impulse amplitude, such as those in Figure 5-2, and of the n th time frame. $V(n)$ is the accumulated volume of rain measured by the tipping bucket during the n th time frame, whereas $\hat{V}(n)$ is the corresponding volume of rain measured by the acoustic sensor. Note that both $V(n)$ and $\hat{V}(n)$ correspond to the volume of rain collected over an area equivalent to the sensor diaphragm, A_s . The time frame n is triggered by the tipping bucket, corresponding to the accumulation of a constant volume of water V_0 in the collector (V_0 might typically be equal to 0.01 inches multiplied by A_s), where n could correspond to a few seconds for a hard downpour or several minutes for a light drizzle. $\hat{V}(n)$ is calculated by summing the m th estimated raindrop volume $\hat{v}_m(n)$ from Equation (5.3), the *adaptive drop size estimator* algorithm shown in Figure 4, for all M_n drops in the n th time frame. The drop diameter $D_m(n)$ is then estimated from the estimated volume assuming a spherical shape:

$$D_m(n) = (6 \hat{v}_m(n) / \pi)^{1/3} \tag{5.4}$$

Note that the form of Equation (5.3) is arbitrarily based on a polynomial power series of x^β , and that other forms may likely exist which will yield improved results.

The parameters $\alpha_0, \alpha_1, \dots, \alpha_{L-2}$, and β are the coordinates of an L -dimensional error surface defined by Equations (5.1) through (5.3). Using the *Steepest Descent* gradient search algorithm, an approximately optimized set of parameters can be found,

and by evaluating Equations (5.3) and (5.4), provide the calibration curve for any subsequent sensor output. In this way, the disdrometer is calibrated for all future measurements where periodically, the adaptive calibration procedure can again be performed to compensate for changes in the sensor response.

During the sensor calibration phase, or equivalently the coefficient adaption phase, the drop size estimation parameters are updated using the gradient of Equation (5.1):

$$\mathbf{c}(l) = \mathbf{c}(l-1) - \mu \nabla E(n) \quad (5.5)$$

$$\mathbf{c} = \begin{bmatrix} \alpha_0 \\ \alpha_1 \\ \vdots \\ \alpha_{L-2} \\ \beta \end{bmatrix} \quad (5.6)$$

$$\nabla E(n) = \begin{bmatrix} \frac{\partial}{\partial \alpha_0} \\ \frac{\partial}{\partial \alpha_1} \\ \vdots \\ \frac{\partial}{\partial \beta} \end{bmatrix} E(n) \quad (5.7)$$

where μ is the convergence *gain factor* (gradient search step size) and the index l represents a multiple coefficient update, occurring during the time frame n . The number of iterations or multiple updates defined by Equation (5.5) necessary to arrive at a coefficient vector \mathbf{c} in the vicinity of the error surface minimum, may be several thousand. The reason for the large number of iterations at each time frame n is due to the limited number of available tipping bucket triggers (or clocks) during a typical rainfall event. The total number of tipping bucket clocks is often a hundred or less for a typical, fast moving, summer thunderstorm.

The number of data sets $\mathbf{x}(n)$ (consisting of M_n components $x_m(n)$) stored in memory for use in Equation (5.5) is N , as specified by Equation (5.1). The gradient term of Equation (5.5) is shown to depend on a triple sum from Equations (5.1) through (5.3). Therefore, each iteration of each component of Equation (5.5) involves $L M_n N$ terms, where $L = 3$, $M_n = 1000$, and $N = 50$ might be typical values. The total number of terms per component, per iteration of the coefficient vector, is then 150000 for these example values. In addition, the amount of memory required to store the N vectors of $\mathbf{x}(n)$, is $M_n N$ which is equal to 50000, again using the above typical values.

The total number of iterations and memory storage requirements can be reduced significantly by representing $\mathbf{x}(n)$, a vector of variable length M_n , by a histogram vector $\mathbf{H}(n)$ of constant length P , such that:

$$\sum_{j=0}^{P-1} \sum_{k=0}^{L-2} \alpha_k u_j^{k\beta} H_j(n) = \sum_{m=1}^{M_n} \hat{v}_m(n) = \hat{V}(n) \quad (5.8)$$

$$u_j = x_1 \exp\left[\frac{\ln(x_2 / x_1)}{P-1} j\right] \quad (5.9)$$

where x_1 and x_2 are the lower and upper limits of x_m , defined by the number of bits used to sample the acoustic sensor output. For a 16 bit sampling system, half of the bits are used to represent x_m because of the absolute value operation shown in Figure 5-3, so that $x_1 = 2^{-15}$ and $x_2 = 1-2^{-15}$. Using this method, the histogram $\mathbf{H}(n)$ is a logarithmic partitioning of the drop amplitude vector $\mathbf{x}(n)$ into P bins.

The gradient vector in the coefficient update formula of Equation (5.5) now becomes:

$$\begin{aligned}
\nabla E(n) &= \frac{\partial}{\partial \mathbf{c}} E(n) = \frac{\partial}{\partial \mathbf{c}} \sum_{k=0}^{N-1} \left[V_0 - \hat{V}(n-k) \right]^2 \\
&= -2 \sum_{k=k_1}^{k_2} \left[V_0 - \hat{V}(k) \right] \mathbf{G}(k) \\
&= -2 \sum_{k=k_1}^{k_2} \left[V_0 - \sum_{j=0}^{P-1} \sum_{k=0}^{L-2} \alpha_k u_j^{k\beta} H_j(k) \right] \mathbf{G}(k)
\end{aligned} \tag{5.10}$$

$$\begin{aligned}
\mathbf{G}(k) &\equiv \frac{\partial}{\partial \mathbf{c}} \hat{V}(k) \\
&\quad \frac{\partial}{\partial \mathbf{c}} \sum_{j=0}^{P-1} \sum_{k=0}^{L-2} \alpha_k u_j^{k\beta} H_j(k)
\end{aligned} \tag{5.11}$$

where the summation over k has been rewritten as a summation over a new k index with limits of $k_1 = n - N + 1$ and $k_2 = n$. In this way, the summation over the time frame index $n - k$ is treated as a sliding window of length N over time frames k stored in memory. The purpose of the change of summation index is to simplify notation, by representing $H_j(k)$ as a $P \times N$ matrix of components H_{jk} .

Equation (5.11) is the partial derivative of the adaptive drop size estimator output of Figure 5-6, which can now be expressed as:

$$\mathbf{G}_k = \begin{bmatrix} \sum_{j=0}^{P-1} H_{jk} \\ \sum_{j=0}^{P-1} H_{jk} u_j^\beta \\ \vdots \\ \sum_{j=0}^{P-1} H_{jk} u_j^{(L-2)\beta} \\ \sum_{j=0}^{P-1} H_{jk} \left(\sum_{i=1}^{L-2} i \alpha_i u_j^{i\beta} \right) \ln u_j \end{bmatrix} \tag{5.12}$$

$$\nabla E = -2 \sum_{k=k_1}^{k_2} \left(V_0 - \sum_{j=0}^{P-1} \sum_{i=0}^{L-2} \alpha_i u_j^{i\beta} H_{jk} \right) \mathbf{G}_k \tag{5.13}$$

The adaptive coefficient vector of Equation (5.5) can now be updated using Equations (5.12) and (5.13). With typical values of $P = 100$, $L = 3$, and $k_2 - k_1 - 1 = 50$, the total number of iterations per component of the coefficient vector \mathbf{c} is 15000, requiring $(k_2 - k_1 - 1) \cdot P = 5000$ words of memory storage for H_{jk} . The number of iterations and memory storage requirements may be further reduced by increasing k_1 , thus decreasing P , since the first several j bins of H_{jk} are usually well below the sensor's noise threshold.

In order to prevent instability and divergence in the recursive coefficient update formula, and at the same time, allow reasonable convergence with a moderate number of iterations, the constant gain factor μ in Equation (5.5) is replaced with individual gain factors μ_i for each coefficient c_i . An empirical approximation for μ_i , which has experimentally proven (in this work) to be useful under a wide range of conditions, is:

$$\mu_i \leq \frac{c_i}{100 \nabla E_i} \quad (5.14)$$

The μ_i are approximated by Equation (5.14) for some number of initial iterations (1000 for example) and then held constant for the remainder of the adaption process.

Another way to utilize the empirical relationship of Equation (5.14) is to use the quantity $100\mu_i \nabla E_i / c_i$ as a convergence indicator and adjustment for the individual gain factors μ_i . If this quantity remains less than one for each adaption parameter, and continues to decrease with successive iterations, convergence will most likely be achieved.

5.3.3 In Situ Calibration of UCF Disdrometer

Figures 5-7 show examples of $\hat{V}(n)$ versus $t(n)$ from three individual acoustic sensors, along with the tipping bucket data $V(n) = V_0$, where $t(n)$ is the relative time at which the tipping bucket clock pulses occur. The $\hat{V}(n)$ are generated by the output of

the adaptive drop size estimator in Figure 5-6, using the approximately optimized coefficients from Table 5-1. The coefficients in Table 5-1 were generated by updating the adaption coefficient vector of Equation (5.5) with $P = 100$, $N = k_2 - k_1 - 1 = 46$, and $L = 3$, for a thunderstorm event lasting 6 min on August 15, 1996, passing over Satellite Beach, Florida. The number of iterations used to adapt the coefficient vector was approximately 10000 for each of the three sensors. Figure 5-8 is a calibration curve generated for each of the three sensors under test, using the coefficients from Table 5-1 and Equations (5.3) and (5.4).

The raw data output mode of the acoustic disdrometer is the drop size versus time (D/t) mode, which is the output of the parametric drop size estimator, Equations (5.3) and (5.4) (D_m of Figure 5-3). As shown in Figures 5-9, this type of output data is displayed by plotting a small dot at the corresponding drop diameter (vertical axis) and time (horizontal axis) coordinate, where each dot represents a measured raindrop.

An average rainfall rate $R(t)$ during a time interval Δt , is calculated by summing the drop volumes given by Equation (5.3) during a vertical slice of the D/t plot of width Δt :

$$\begin{aligned}
 R(t) \approx R(j\Delta t) &= \frac{1}{A_s \Delta t} \sum_m^{\Delta t} \hat{v}_m \\
 &= \frac{1}{A_s \Delta t} \sum_m^{\Delta t} \sum_{k=0}^{L-2} \alpha_k x_m^{k\beta}
 \end{aligned} \tag{15}$$

where the x index m now represents all drop impulse amplitudes occurring during the j th time interval Δt . Figures 5-10 show the result of converting the D/t data from Figures 5-9 to rainfall rate using Equation (5.15) with $\Delta t = 6$ s and sensor area $A_s = 116.7 \text{ cm}^2$.

Table 5-1. Parameters using Equations (5.3) and (5.4), as shown in Figure 5-8.

Sensor	α_0	α_1	β
B	-1.551	54.12	0.5959
C	-1.806	80.99	0.6002
D	-1.905	64.60	0.5543

Drop size distributions can be extracted from the D/t data of Figures 5-9 by generating a DSD histogram and dividing by the drop terminal velocity. A good approximation for terminal velocity, which takes into account the variation of terminal velocity with atmospheric density, is by Best^[22]:

$$v_D \approx Ae^{bz} \left\{ 1 - e^{-(D/a)^n} \right\} \text{ cm / s} \quad (5.16)$$

where $A = 958 \text{ cm s}^{-1}$, $b = 0.0854 \text{ km}^{-1}$, z is the elevation at the ground (or at the point of measurement), D is the drop diameter, $a = 1.77 \text{ mm}$, and $n = 1.147$. Figures 5-11 show DSD extracted from the D/t data of Figures 5-9. In these examples, the drop size distributions were generated by using D/t data from times of equivalent rainfall rate, defined by partitioning rainfall rate data $R(t)$ into bins of width $\Delta R = 20 \text{ mm/hr}$.

Disdrometer calibration has been an area of debate and concern for the research meteorologist and atmospheric scientist.^[32,34,38] Using an adaptive digital signal processing approach, a calibration algorithm has been proposed which provides a relatively simple means of relating the impact disdrometer response to actual rainfall accumulation. Utilizing a tipping bucket rain gauge as a reference clock, the impulse amplitudes from the disdrometer sensor are transformed by an adaptive drop size estimator algorithm and summed together within a reference time frame defined by the clock. The sum of the transformed impulses within each time frame are all equal and equivalent to the tipping bucket collector volume. An adaptive algorithm updates a

coefficient vector, which attempts to minimize the error between transformed disdrometer volume and the tipping bucket volume, thus producing a set of coefficients which are thereafter used to convert the disdrometer impulse amplitude to drop diameter.

Example data from UCF's acoustic rain gauge sensors was processed using this adaptive calibration algorithm. Rainfall rate was generated from the acoustic sensor data using the coefficient vector obtained from the output of the adaptive drop size estimator and was compared to the rainfall rate calculated from a tipping bucket rain gauge. Comparisons of rainfall rate are shown to be good. It is hoped that this method can be used to replace or supplement previous disdrometer calibration methods, providing additional means of checking accuracy of DSD measurements obtained from impact disdrometers.

5.4. Suppression of Environmental Noise

Using an impulse suppression algorithm, environmental noise such as thunder and wind can be filtered from the sound of raindrops impacting an acoustic rain gauge sensor. A non-linear filter algorithm, based on a gated median filter, was previously used to suppress scratch noise from damaged phonograph records. The goal of this work is to adapt this impulse suppression algorithm and evaluate its performance in detecting and filtering the impulse signal from a sensor element of ARGGA at the University of Central Florida. In this case, the amplitude of each impulse is a measurement of the raindrop size impacting the sensor. By subtracting the filtered signal from a delayed version of the original, the output signal contains only the drop impulses from which the raindrop size distribution can be derived.

5.4.1 Impulse Detection Using a Non-Linear Filter

The adaptive scratch noise filter^[8] was originally inspired from the similarities between scratch filtering of damaged phonograph records and suppression of impulsive noise (known as "salt and pepper") from images. This suggested the idea that filters traditionally used in image processing could be applied for scratch filtering as well. A well-known filter for salt and pepper noise suppression is the *median filter* (MF) which replaces each image pixel with the median of surrounding pixels. However, direct median filtering has undesirable side-effects such as smoothing of noise free regions, resulting in loss of image detail. The *conditional median filter* (CMF) improves the performance of the MF by selectively filtering only pixels contaminated by impulses. Scratch impulses in audio signals have some distinct differences from salt and pepper impulses in images, thus direct application of filters such as the CMF may not produce satisfactory results. This stems from the nature of the source that generates the impulses. Salt and pepper noise is generated from bit errors in the data stream and occurs as isolated impulses. Scratch noise is generated when a phonograph playback stylus encounters discontinuities in the groove and is essentially the impulse response of the playback mechanism. A typical scratch waveform consists of an initial pulse followed by decaying oscillations, due to mechanical vibration of the stylus.

In the case of rainfall drop measurements, the waveforms have a very similar appearance, but now the role of signal and noise is reversed. As shown in the top trace of Figure 3, the drop impact is the equivalent of the phonograph scratch, while thunder is the equivalent of the music audio signal.

The *gated median filter* (GMF) is a modification of the CMF algorithm where an independent detector first locates impulses, then gates a median filter on and off accordingly, as shown in the block diagram of Figure 2. Impulse suppression is accomplished with a median filter placed in the main signal path. The MF is normally

disabled and bypassed, except in those signal regions where impulses have been detected, i.e.:

$$y_n = \begin{cases} m_n & g_n > 0 \\ x_n & \text{otherwise} \end{cases} \quad (5.17a)$$

where:

$$m_x = MED\{x_{n-k}, \dots, x_n, \dots, x_{n+k}\} \quad (5.17b)$$

is the median value over a window of length $N = 2k + 1$ samples. x_n and y_n are the input and output sequences and g_n is a gating signal which is provided with the correct timing so that the MF is activated when impulses are within the filter window. It is well known that MFs preserve smooth signal regions and suppress impulses of widths narrower than $k = (N - 1)/2$. The signal g_n is generated in the lower branch of Figure 12 where impulse detection and gating generation take place.

The input signal is first highpass filtered so that the presence of impulses (which are rich in high frequencies) are enhanced. The highpass filter used is a simple discrete second derivative approximation, and the output z_n is given by:

$$z_n = D^2\{x_n\} = x_{n-1} - 2x_n + x_{n+1} \quad (5.18)$$

The second derivative produces a large output when an abrupt change in slope is encountered. Because of the oscillatory characteristics of the scratch waveform, the MF must remain active for the entire duration of a scratch. Thus, the gating impulse must bracket the scratch waveform. An impulse profile w_n can be obtained from the envelope of a full-wave rectified z_n . This can be accomplished by a local *recursive median filter* (RMF) operator applied on z_n over a sliding window of length M , i.e.:

$$w_n = \left(\frac{1}{M+1} \sum_{j=-M/2}^{M/2} z_{n+j}^2 \right)^{1/2} \quad (5.19)$$

This RMS operator was found to discriminate impulses better than simple local averaging of $|z_n|$. Smoothing the output of the highpass filter defines the impulse duration more clearly. The length M of the averaging window is not very critical, but it should be large enough to include at least one cycle of the impulsive oscillations.

The gating signal g_n can be obtained by applying a threshold on w_n with respect to a signal reference floor b_n which excludes peak excursions. Again, we may call upon the MF for assistance in generating b_n but a recursive median filter would be more appropriate because in a single application it can suppress multiple closely spaced impulses, whereas, the MF may require repeated applications. The RMF is identical to the MF with the exception that previous medians are placed in the input buffer and used in the computation of subsequent medians. Compared to Equation (5.17a) the RMF output r_n is obtained from:

$$r_n = MED\{r_{n-k}, \dots, r_{n-1}, x_n, x_{n+1}, \dots, x_{n+k}\} \quad (5.20)$$

Since impulse peak widths in w_n may exceed 30 samples, the RMF window length required to extract the background should be over 60 samples, but such large windows are computationally expensive. A simple method to reduce the window size and number of computations, without significant performance loss, is to decimate w_n and use a small RMF window. The final background extraction operator, in this case, can be written as:

$$b_n = RMF\{w_n; L, K\} \quad (5.21)$$

where L is the RMF window length, K is the decimation ratio, and KL is the effective RMF window length. The gating signal is defined from the normalized absolute difference between w_n and b_n as:

$$g_n = \begin{cases} m_n & d_n > C \\ 0 & \text{otherwise} \end{cases} \quad (5.22a)$$

where,

$$d_n = \frac{|w_n - b_n|}{b_n} \quad (5.22b)$$

and m is the number of consecutive sample positions where the upper branch of Equation (5.22a) is valid. Essentially m indicates the width of the resulting gates in g_n . Normalization by b_n makes d_n insensitive to input conditions (amplitude or spectral content) so that a constant value for the threshold C can be used. Values of C from 1.5 to 2.5 seemed to work well over a wide range of input conditions.

The adaptive scratch filter can now be expressed as:

$$y_n = MED\{x_{n-g_n}, \dots, x_n, \dots, x_{n+g_n}\} \quad (5.23)$$

where the filter window length $N_n = 2g_n + 1$ is dependent on the gate width so that when $g_n = 0$, no filtering takes place. For this reason, the filter is adaptive. The top trace of Figure 13, x_n shows typical rain drop data from a UCF disdrometer contaminated by thunder and wind noise. The middle trace y_n is the result of filtering x_n with the filter algorithm summarized in Equation (5.23). The final data used to determine the DSD, shown in the bottom trace of Figure 13, is simply $x_n - y_n$.

5.4.2 Noise Suppression of Thunder with a Median Filter

The primary DSP functions previously used to process data from the ARGAs disdrometer, are (1) signal filtering and (2) signal peak detection with amplitude estimation. The filtering is accomplished by a 16th order bandpass filter, centered around the resonant frequency of the sensor diaphragm, $f_0 = 750$ Hz, with a bandwidth of 350 Hz. An amplitude estimation algorithm incorporates any necessary dead-time by recognizing characteristics in the pulse which may correspond to impulse overlap. The peak detection and amplitude estimation algorithms are based on pattern recognition principles.

During a rainfall event, all impulses over the sensor's measurement area, and within a time frame interval T (for example, $T = 30$ s), are measured and converted to equivalent drop volumes using a parametric relationship between drop diameter and the maximum amplitude of the measured impulse^[37]. The raw output display mode of the acoustic disdrometer is drop size versus time (D/t) plot, as shown in Figure 14a. This output format is accomplished by plotting a small dot at the corresponding drop diameter (vertical axis) and time (horizontal axis) coordinate, where each dot represents a measured raindrop^[39]. A complex plotting routine might adjust the dot size based on the raindrop diameter in order to accurately convey the drop density. In Figure 14a, all dots are of equal size, but the density is nevertheless apparent from this plotting format. Consecutive vertical time slices of the D/t plot can be readily converted to a rainfall rate versus diameter $R(D)$ distribution (or histogram) by counting the number of dots in corresponding drop size bins, converting to equivalent spherical volumes, dividing out the area of the sensor, and dividing by the width of the time slice. The total rainfall rate R during that time interval is the integral of $R(D)$ over all diameters. Figure 14b shows R as a function of time corresponding to the data in Figure 14a. The dotted line is

rainfall rate measured by a tipping bucket rain gauge. The data shown in Figures 14a was processed by the bandpass filter method described in a previous section.

As can be seen by examination of the D/t plot of Figure 14a, linear filtering methods lead to problems during high background noise such as thunder (shown as vertical lines) which degrade the overall DSD measurement. Figure 15a and 15b show the same data as Figures 14, but processed by the adaptive non-linear filter described by Equation (5.23). The thunder noise is suppressed in this case. However, the lower drop size detection limit has increased so that in the case of Figure 15a, the DSD lower cutoff is approximately 2 mm, whereas, in the previous case, data is detected to approximately 1 mm or lower.

Optimization of the median filter parameters could increase the drop diameter sensitivity, with a possible trade-off with some noise contamination. Alternatively, a method which may yield the best performance would be a combination of both the linear and non-linear filtering methods. A possible strategy would be to use linear filtering on data with relatively low background noise, then automatically switch to the non-linear filter when the background noise rises above a threshold value. This will be a subject of future work.

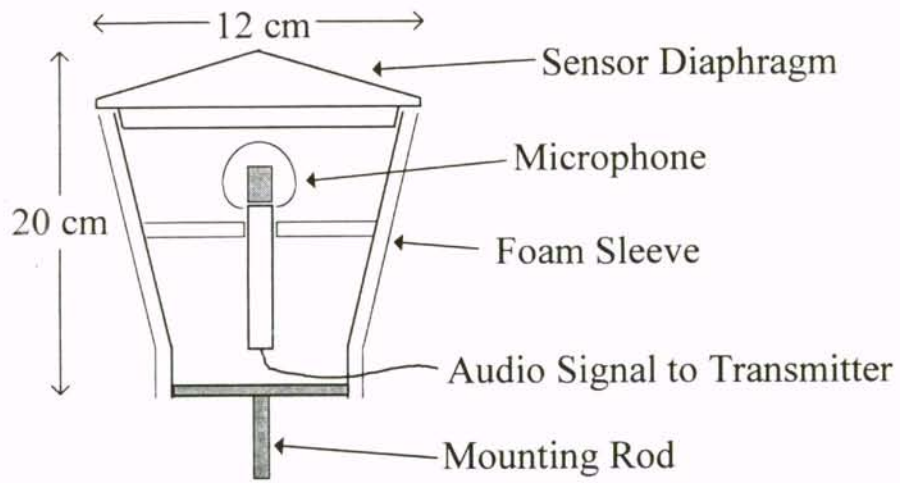


Figure 5-1. Schematic diagram of acoustic sensor.

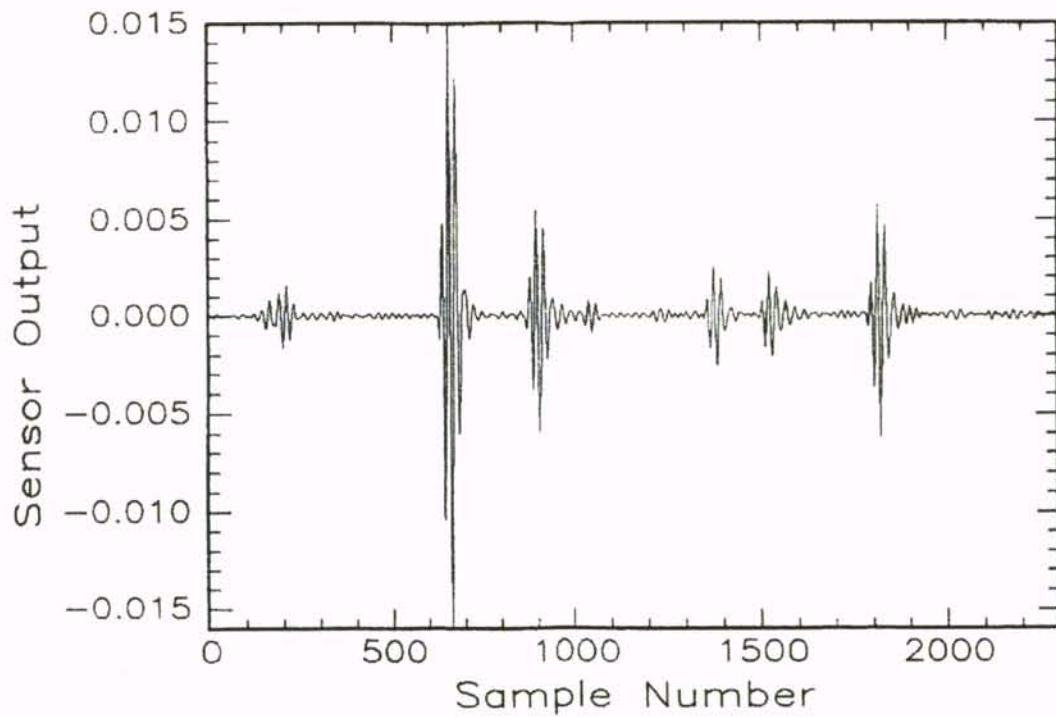


Figure 5-2. Sampled output of acoustic sensor.

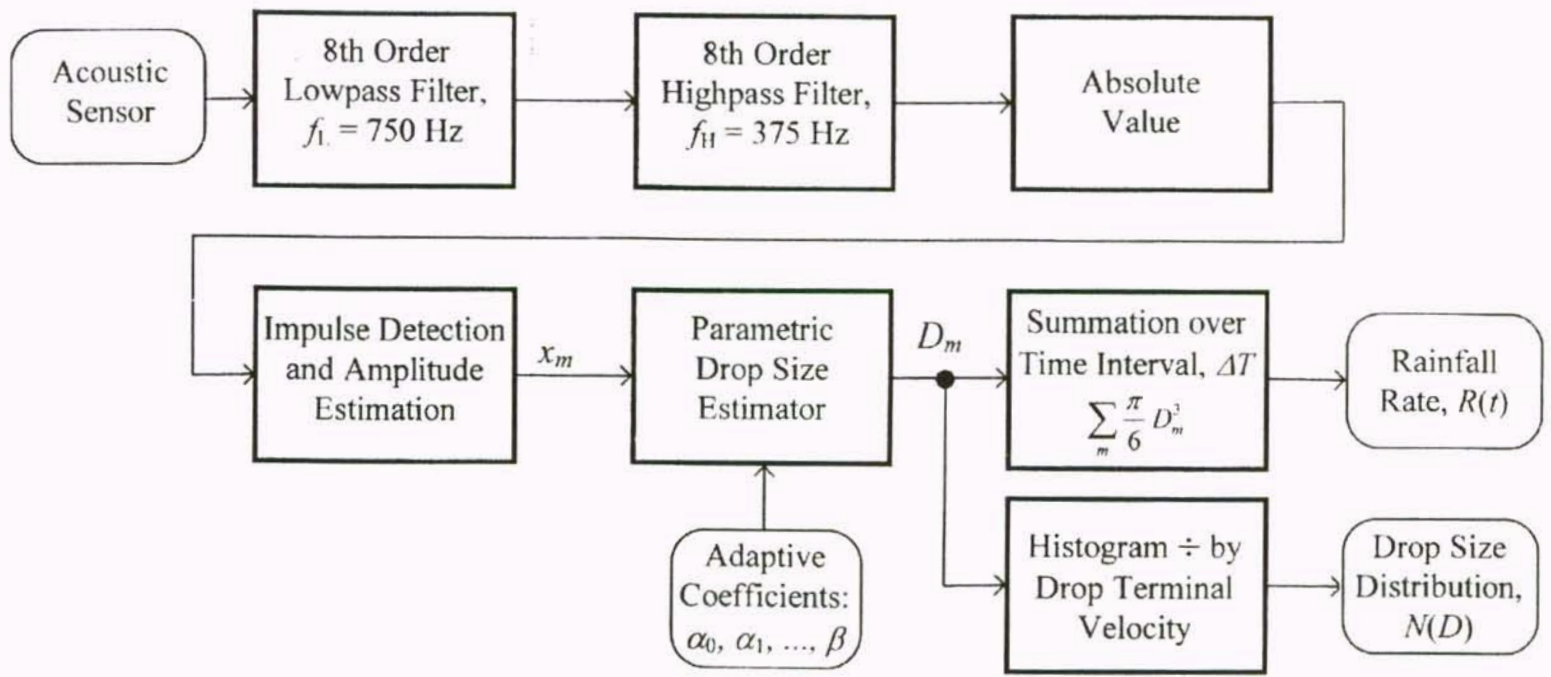


Figure 5-3. Block diagram of acoustic sensor's digital signal processing section.

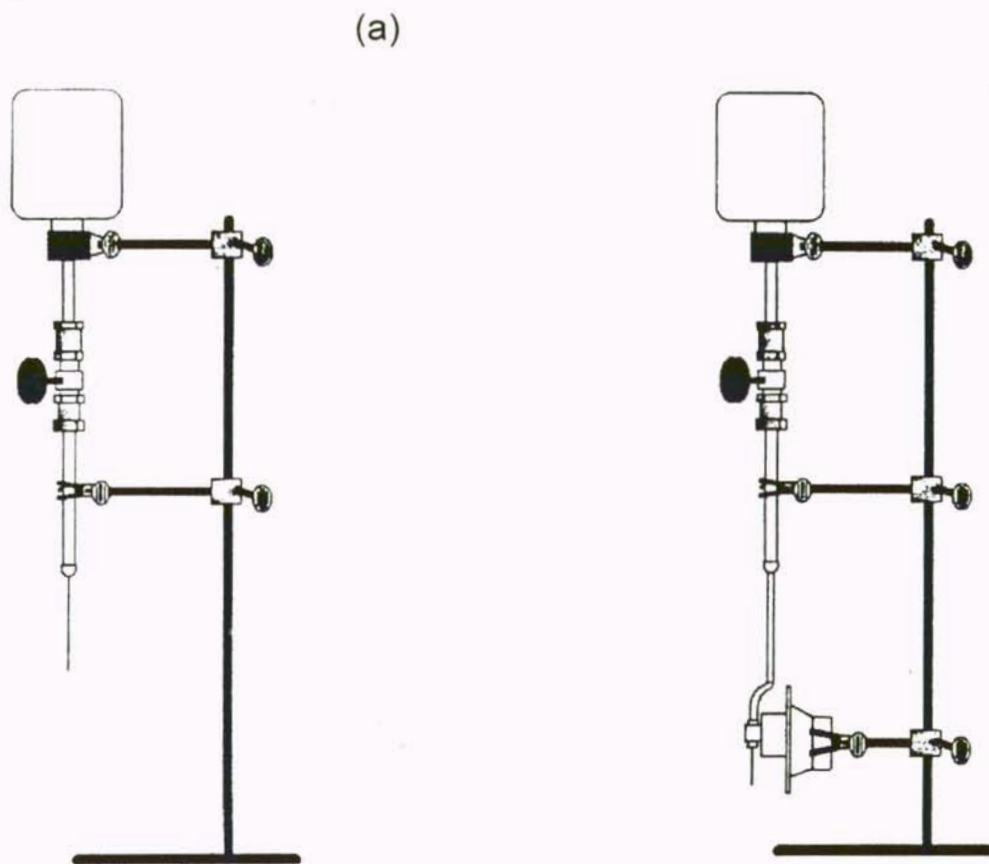
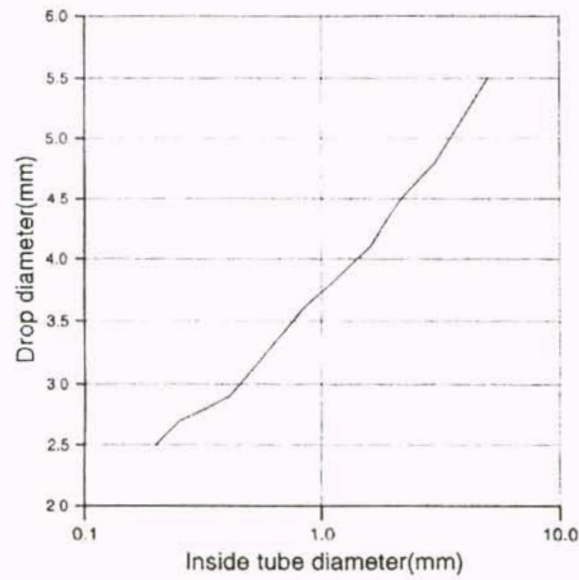


Figure 5-4. (a) Synthetic drop production apparatus. The large drop generator produces different sized drops by allowing drops to form at the end of different diameter tubes. (b) Small drop generator actively knocks drops off the tip of a small tube using an audio speaker.

(a)



(b)

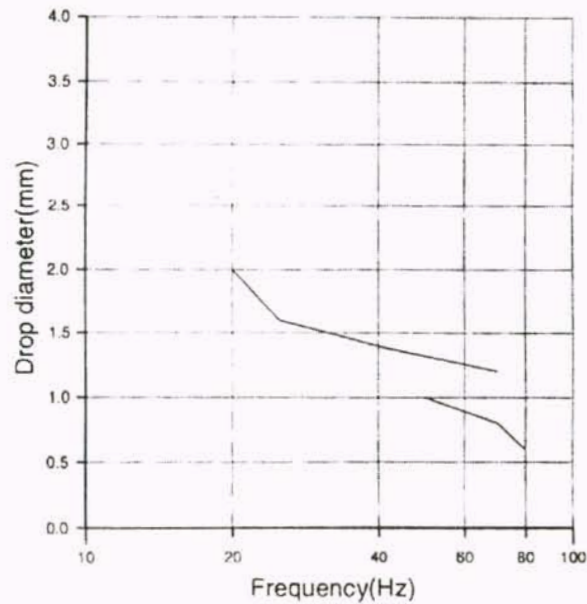


Figure 5-5. (a) Relationship between inner diameter tube size and drop diameter using the large drop generator. (b) Relationship between audio speaker frequency and drop diameter using the small drop generator (top curve is for a 0.3 mm inner diameter tube and bottom curve is for a 0.2 mm inner diameter tube).

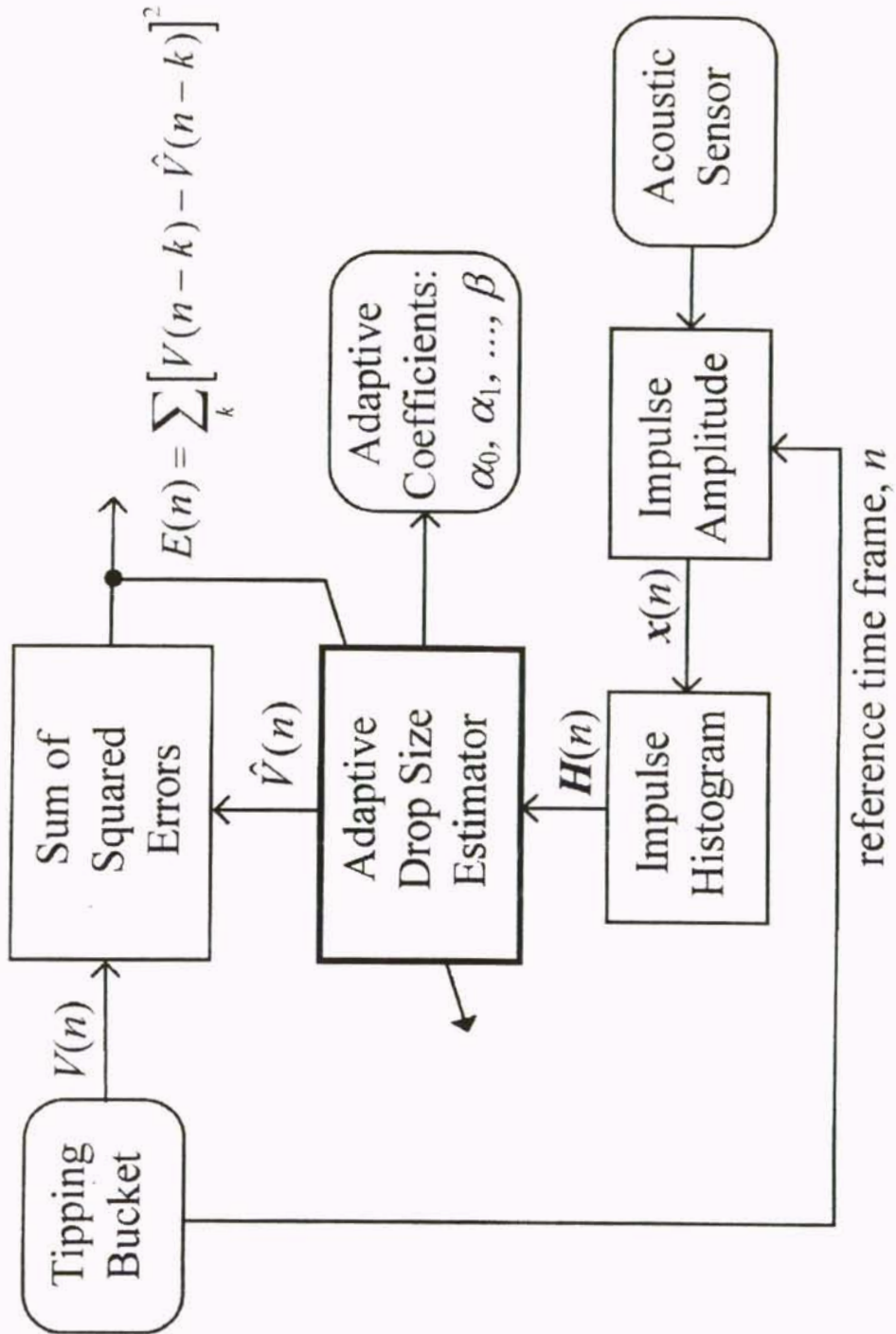


Figure 5-6. Block diagram of adaptive DSP calibration algorithm.

(a)

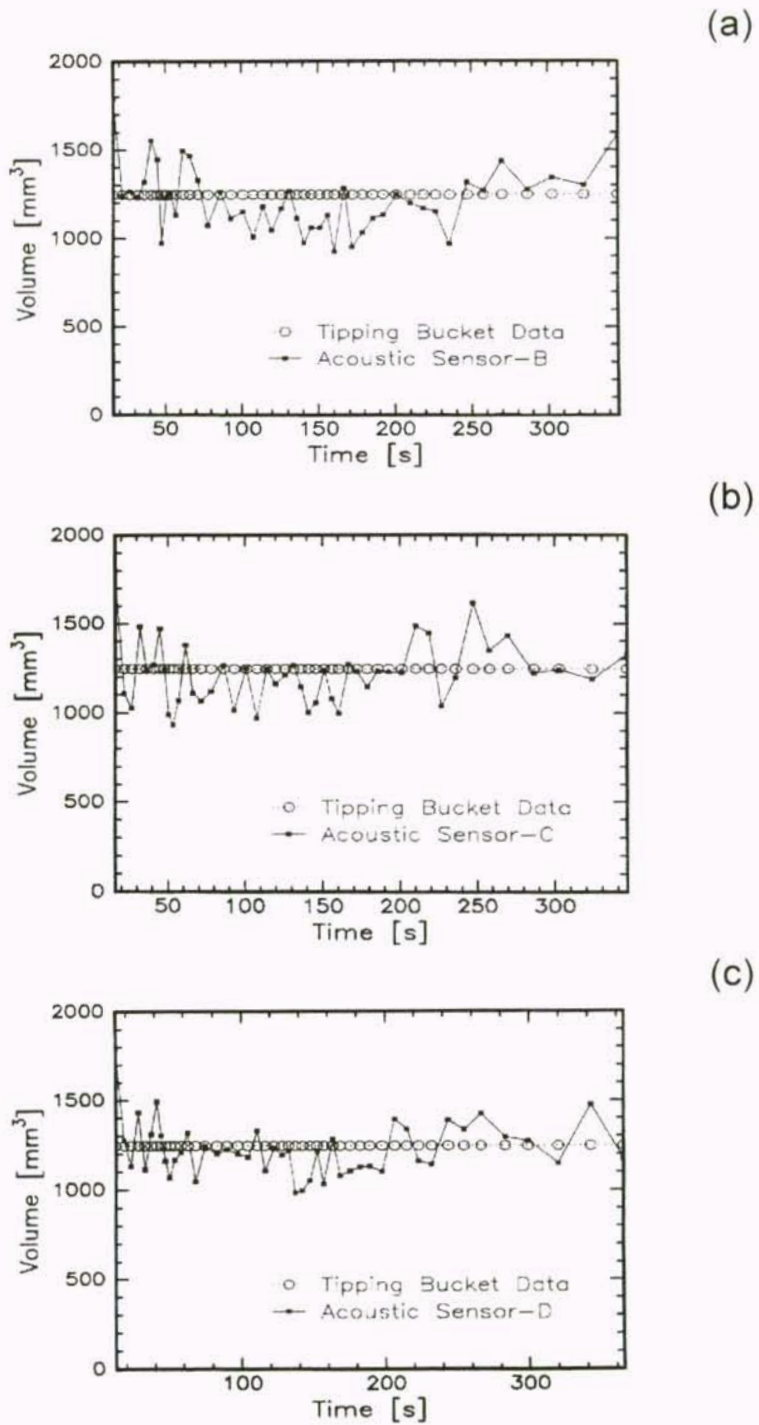


Figure 5-7. $V(n)$ (open circles) and $\hat{V}(n)$ (solid squares) versus $t(n)$ for (a) sensor B, (b) sensor C, and (c) sensor D, using coefficients from Table 5-1.

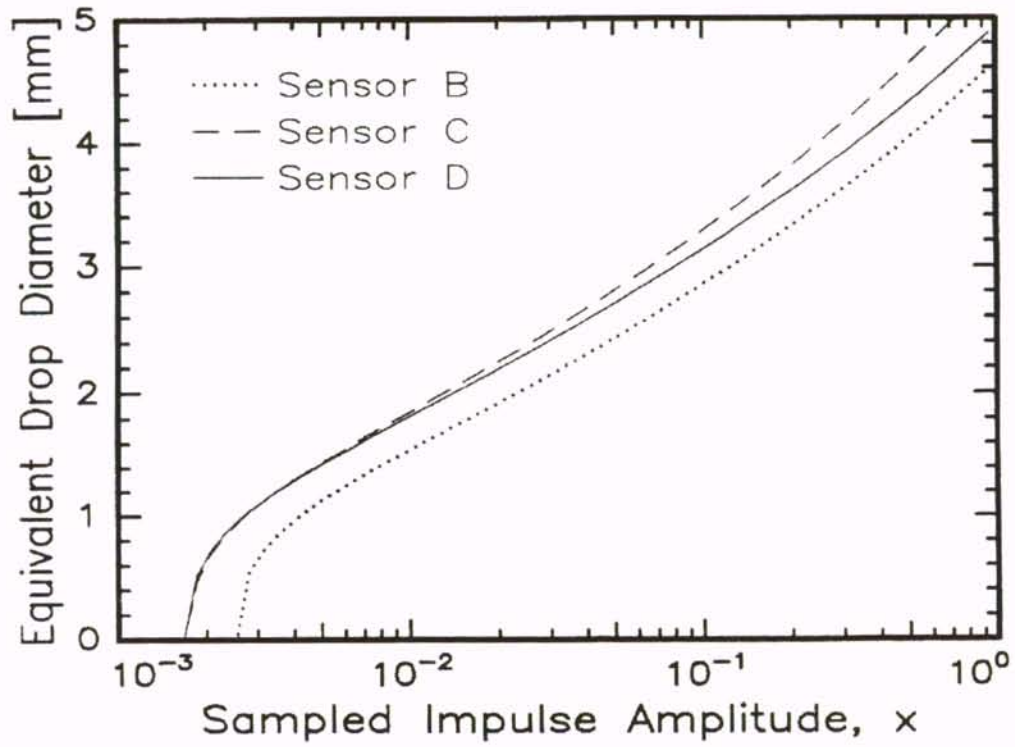
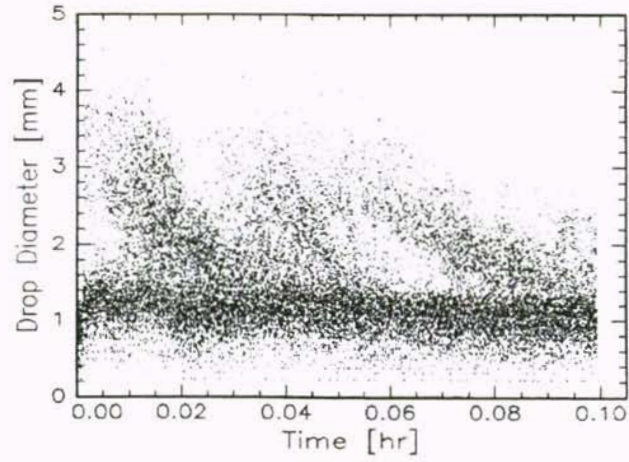
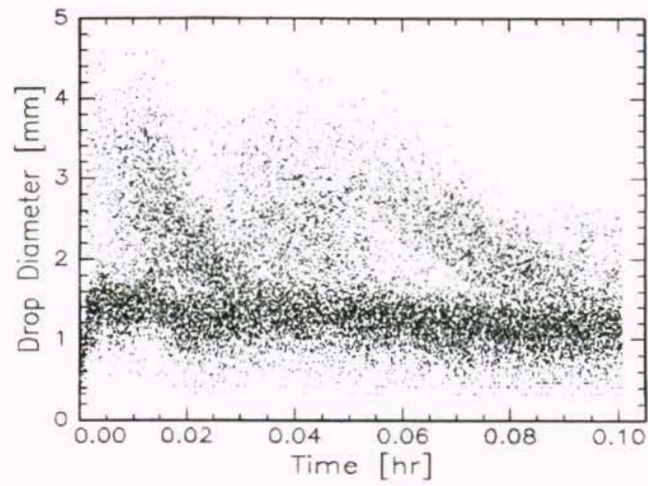


Figure 5-8. Calibration curves for three acoustic sensors, based on coefficients from Table 5-1.

(a)



(b)



(c)

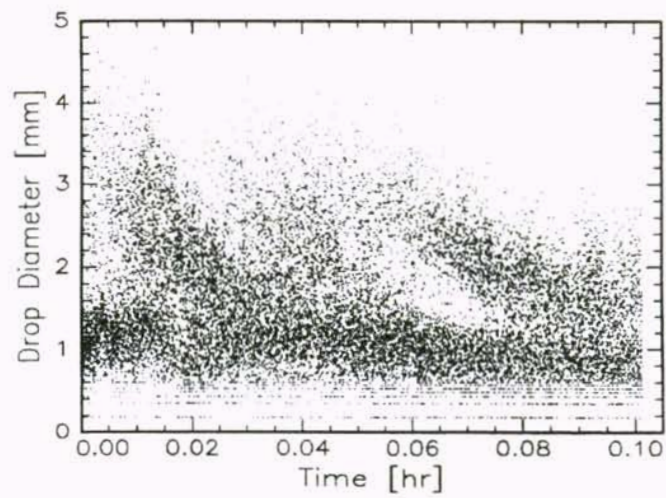
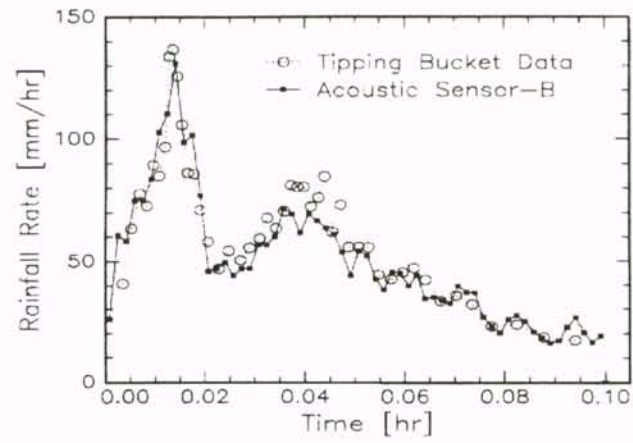
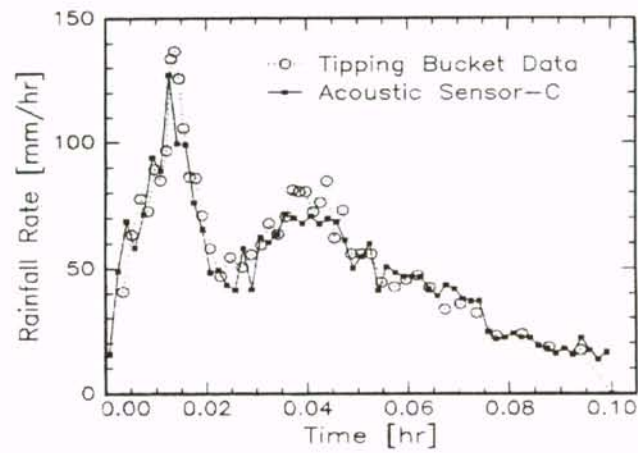


Figure 5-9. D/t plots for (a) sensor B, (b) sensor C, and (c) sensor D.

(a)



(b)



(c)

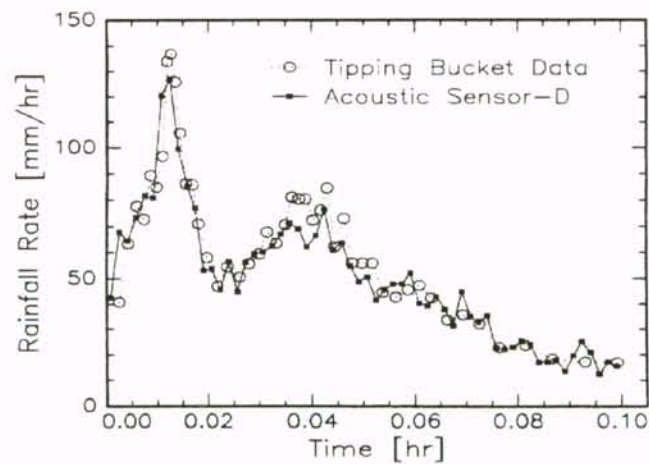


Figure 5-10. Rainfall rate versus $t(n)$ with $\Delta t = 6$ s. Open circles are tipping bucket data and solid squares are acoustic sensor data, for (a) sensor B, (b) sensor C, and (c) sensor D.

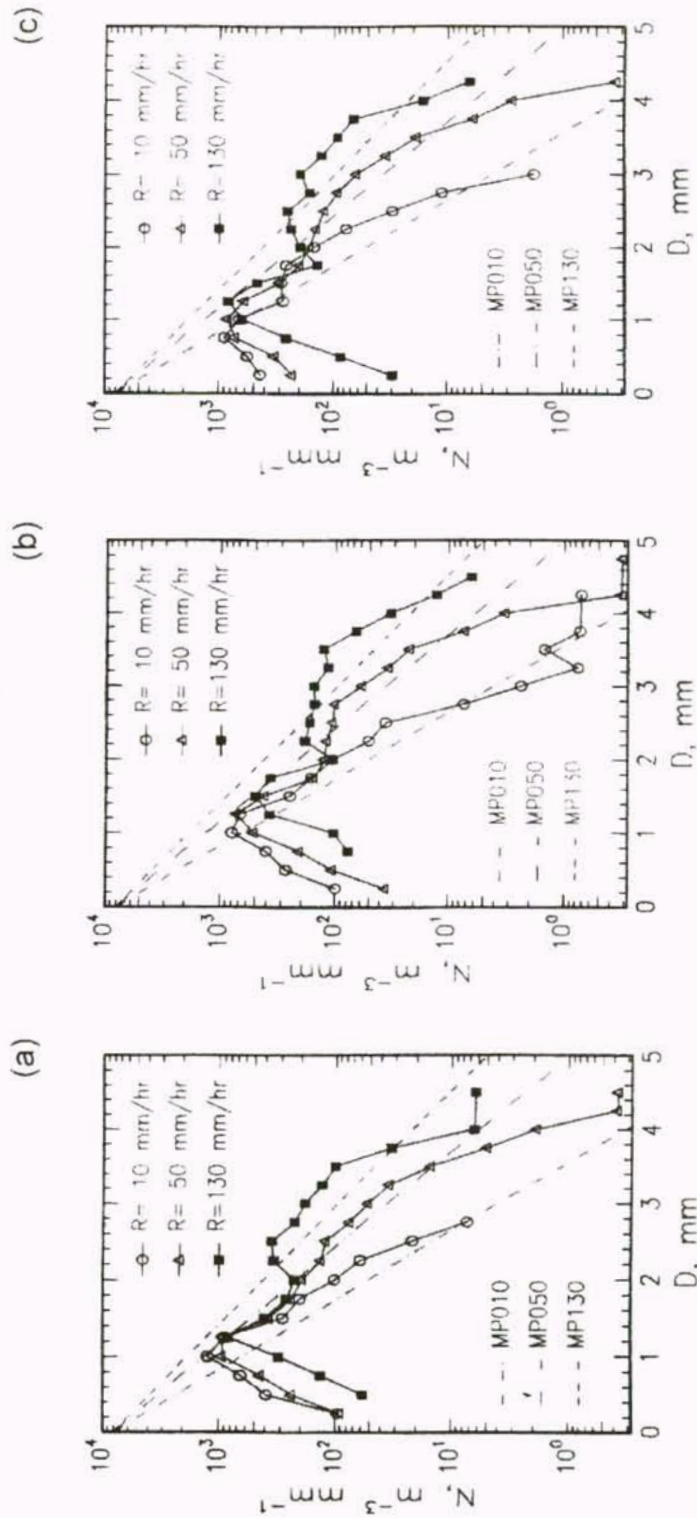


Figure 5-11. Various rainfall rate drop size distributions $N(D)$ for (a) sensor B, (b) sensor C, and (c) sensor D. Also shown are the equivalent Marshall-Palmer DSD approximations for the same rainfall rates.

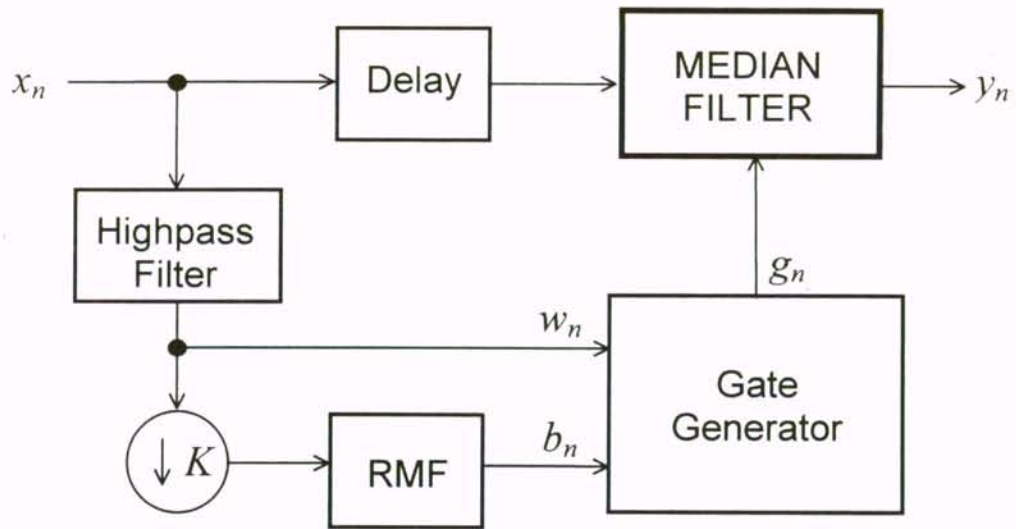


Figure 5-12. Block diagram of adaptive scratch filter.

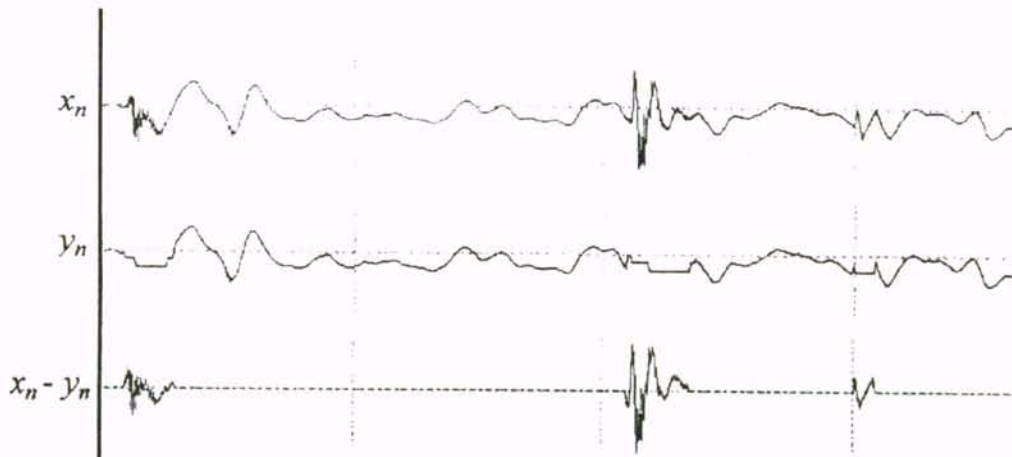


Figure 5-13. Processing of ARGAs disdrometer data by adaptive scratch filter algorithm. Top trace is input data x_n ; middle trace is filter output y_n , as described by Equation (5.13); and bottom trace is the difference of the input and output signals.

(5.23)

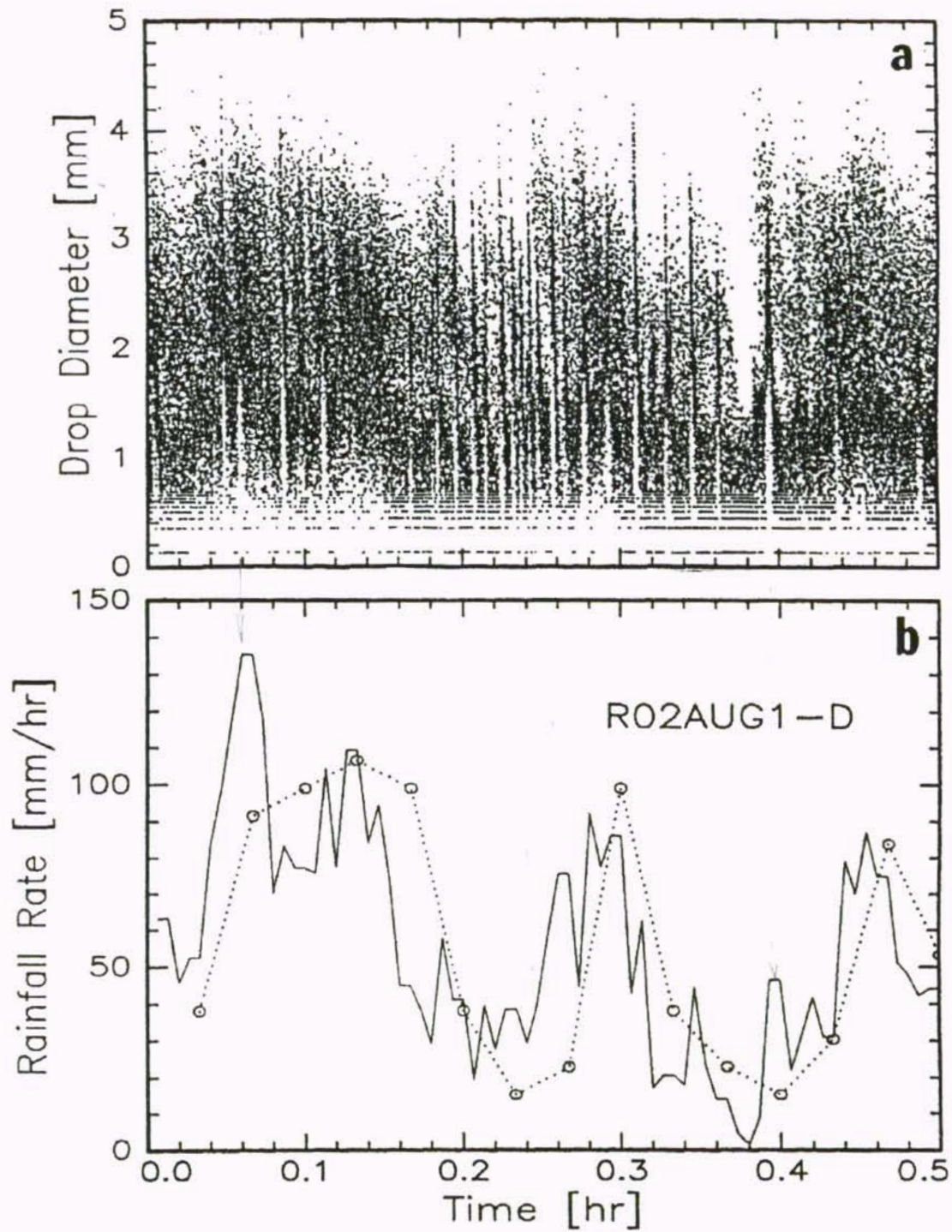


Figure 5-14. ARGA disdrometer data processed by previous linear filter; (a) drop diameter D versus time, (b) calculated rainfall rate R versus time (solid line) and tipping bucket data (dotted line).

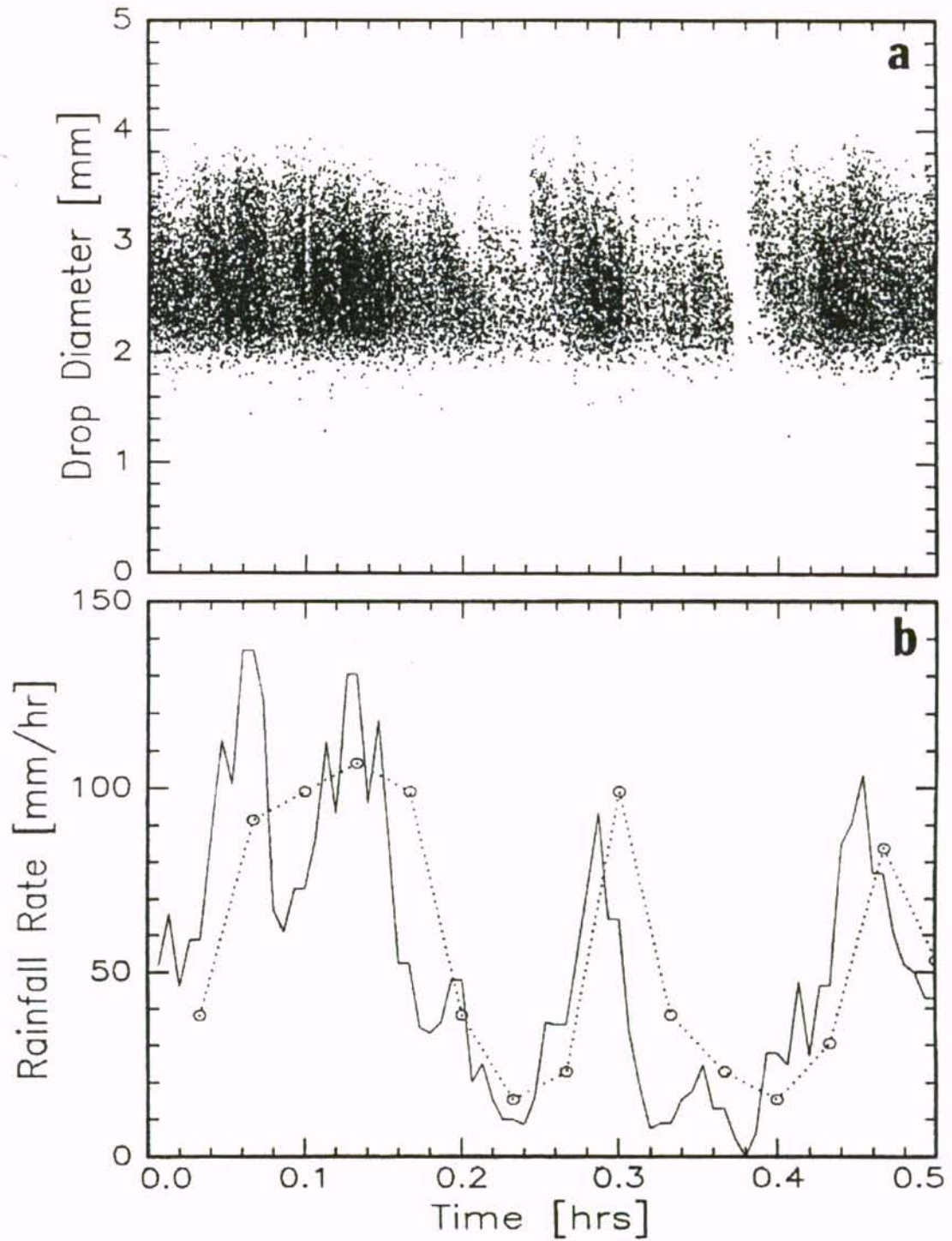


Figure 5-15. Same data shown in Figures 5-14, but processed by non-linear filter of Equation (5.13).

CHAPTER 6

CONVOLUTION RAINFALL MODEL

6.1 Background

The primary goal of this simulation model is to study the effects of advection and gravitational sorting on drops as they fall. This model considers only drop dynamics and for that reason is too over-simplified to produce quantitative results that would be observed in nature. Since factors such as evaporation, drop breakup and coalescence, and updraft/downdraft velocities will be ignored, simulation results are only expected to yield some qualitative insight into the nature and variation of the Z - R relationship under conditions of advection and large transient conditions of rainfall rate. These characteristics are common to convective thunderstorm systems across central Florida during the summer months.

6.2. Mathematical Development

The basis of the *convolution rainfall* (CR) model is the *exponential* drop size distribution:

$$N(D) = N_0 e^{-\Lambda D} \quad (6.1)$$

where N_0 and Λ are independent parameters, possibly dependent on rainfall rate. Using the approach of Marshall-Palmer^[16] (MP), Λ can be defined as a function of rainfall rate:

$$\Lambda = \xi R^{-\epsilon} \quad (6.2)$$

where ξ and ε are again independent parameters. In the case of the MP DSD $\Lambda = 4.1 R^{-0.21} \text{ mm}^{-1}$. Using terminal velocity as defined by Gunn^[21], $v_D \approx K D^{1/2} \text{ m s}^{-1}$, where $K \approx 4.5 \text{ m s}^{-1} \text{ mm}^{-1/2}$ and D is expressed in mm, rainfall rate becomes the 7/2 moment of the DSD:

$$\begin{aligned}
 R &= 0.0036 K \frac{\pi}{6} \int_0^{\infty} D^{7/2} N(D) dD \\
 &= K' \int_0^{\infty} D^{7/2} N_0 e^{-\xi R^{-\varepsilon} D} dD \\
 &= K' (\xi R^{-\varepsilon})^{-9/2} N_0 \int_0^{\infty} x^{7/2} e^{-x} dx \\
 &= K' \xi^{-9/2} R^{9\varepsilon/2} N_0 \Gamma(9/2)
 \end{aligned} \tag{6.3}$$

where $K' \equiv 0.0036 K \frac{\pi}{6}$ and the scale factor 0.0036 allows rate R to be expressed in standard units of mm/hr. Note that the *gamma function* $\Gamma(9/2) = \frac{105}{16} \sqrt{\pi}$.

Since R appears on both sides of Equation (6.3), the implication is that the exponential DSD parameters N_0 , ξ , and ε defined by Equations (6.1) and (6.2), are not independent. Two constraints result as a consequence of Equation (6.3):

$$\varepsilon = 2/9 \tag{6.4a}$$

$$\begin{aligned}
 \xi &= [K' N_0 \Gamma(9/2)]^{2/9} \\
 &= 0.5977 N_0^{2/9}
 \end{aligned} \tag{6.4b}$$

Using the “standard” value of $N_0 = 8000 \text{ m}^{-3} \text{ mm}^{-1}$, $\xi = 4.404$. For comparison, the MP DSD defines these values as $\varepsilon = 0.21$ and $\xi = 4.1$. Using $N_0 = 8000 \text{ m}^{-3} \text{ mm}^{-1}$, the normalized (based on terminal velocity by Gunn) exponential DSD can be expressed as a function of D and R as:

$$\begin{aligned}
N(D; R) &= N_0 \exp(-0.5977 N_0 R^{-2/9} D) \\
&= 8000 \exp(-4.404 R^{-2/9} D)
\end{aligned}
\tag{6.5}$$

The basic assumption of the CR model is that the *normalized* DSD as described by Equation (6.5) represents the distribution of rain drops at a cloud height h , where R is defined as a function of the spatial horizontal distance \bar{r} and time t . A simplified (one spatial dimension) *Gaussian* model of R will be defined which captures the basic characteristics of the total time derivative of rainfall, spatial variation, and advection:

$$R(x, t) \equiv R_0 e^{-[(t-t_0)/A]^2 - [(x-x_0-ut)/B]^2} \tag{6.6}$$

characterized by the parameters R_0 , A , and B where u is the advection velocity. The parameters A and B define the temporal and spatial widths of the rainfall rate function, as well as the corresponding widths of the DSD. As $A \rightarrow \infty$ and $B \rightarrow \infty$, $R(x, t) \rightarrow R_0$ for all time and space. Figure 6-1 portrays an example rainfall rate function $R(x, t)$ at a height h above the ground, based on the description provided by Equation (6.6).

Radar reflectivity Z is the 6th moment of the DSD, and using the exponential form of Equation (6.1) and (6.2), becomes:

$$\begin{aligned}
Z &= \int_0^{\infty} D^6 N(D) dD \\
&= N_0 \int_0^{\infty} D^6 e^{-\xi R^{-\varepsilon} D} dD \\
&= N_0 (\xi R^{-\varepsilon})^{-7} \int_0^{\infty} x^6 e^{-x} dx \\
&= N_0 \xi^{-7} R^{7\varepsilon} \Gamma(7)
\end{aligned}
\tag{6.7}$$

Note that $\Gamma(7) = 6! = 720$. Using the parameter constraints from Equations (6.4), Z then becomes:

$$\begin{aligned} Z &= N_0 \left[K' N_0 \Gamma\left(\frac{9}{2}\right) \right]^{-14/9} R^{14/9} \Gamma(7) \\ &= a R^b \end{aligned} \quad (6.8a)$$

where $a \approx 26423 N_0^{5/9}$ and $b = 14/9$ where Z is in standard units of $\text{mm}^6 \text{m}^{-3}$ and R is in units of mm h^{-1} . Using the standard value of $N_0 = 8000 \text{m}^{-3} \text{mm}^{-1}$, the Z - R relation becomes:

$$Z \approx 180 R^{1.6} \quad (6.8b)$$

6.2.1 Rainfall Rate Model

Rainfall rate $R_G(x_G, t)$ measured at gauge location x_G , is in general, not the same as the rainfall rate $R(x, t)$ at the cloud level. For the limiting case of infinite A and B :

$$R_G(x, t) \rightarrow R(x, t) \rightarrow R_0, \quad \text{for } \begin{array}{l} A \rightarrow \infty \\ \& \\ B \rightarrow \infty \end{array} \quad (6.9a)$$

This result is independent of the magnitude of u . Another useful case, with finite B , results in a relation between cloud rainfall and ground rainfall:

$$\begin{array}{l} R_G(x, t) \rightarrow R(x, t) \quad A \rightarrow \infty \\ \& \\ R_G(x_0, t) \rightarrow R(x_0, t) \rightarrow R_0 \quad u \rightarrow 0 \end{array}, \quad \text{for } \& \quad (6.9b)$$

The relations expressed by Equations (6.9) are useful for testing the validity of the simulation model.

Referring to Figure 6-1, it can be seen that the DSD at gauge location x_G on the ground, is convolution sum of drop sizes formed at past times and locations based on advection. The explanation for this model is simply this: For the j th drop size bin of width ΔD , corresponding to a mean drop diameter of $D_j \equiv j\Delta D$, the fall time Δt_j of the drop (based on Gunn's terminal velocity) is:

$$\Delta t_j = h / (K D_j^{1/2}) \quad (6.10)$$

The horizontal distance Δx_j in the negative x direction from the gauge location (for $u > 0$), corresponding to the time interval Δt_j is:

$$\begin{aligned} \Delta x_j &= u\Delta t_j \\ &= uh / (K D_j^{1/2}) \end{aligned} \quad (6.11)$$

Together, Equations (6.10) and (6.11) describe the linear trajectory of a rain drop packet ΔN_j of mean size D_j :

$$\Delta N_j \equiv N(D_j) \Delta D \quad (6.13)$$

traveling at a constant velocity \vec{v}_j formed by the vector sum of the advection and terminal velocity vectors:

$$\vec{v}_j = -K D_j^{1/2} \hat{e}_z + u \hat{e}_x \quad (6.14)$$

where \hat{e}_x and \hat{e}_z are unit vectors in the x and z directions, respectively. For a fall height of $z = h = 0$, the total number of drops arriving at the gauge is the integral of the DSD, and is approximately equal to the sum of the ΔN_j :

$$\int_0^{\infty} N(D) dD \approx \sum_{j=0}^{\infty} \Delta N_j = \sum_{j=0}^{\infty} N(j\Delta D) \Delta D \quad (6.15)$$

The rainfall arriving at the gauge location is 7/2 moment of the DSD (using Gunn for terminal velocity). However, the DSD at the gauge site is not the same as the DSD at cloud level $z = h$. The correct description of rainfall rate at the gauge site is the 7/2 moment of the *convolved* DSD, now using a continuous time and space description :

$$R_G(x_G, t) = K' \int_0^{\infty} D^{7/2} N[D; R(x', t')] dD \quad (6.16)$$

where $K' \equiv 0.0036 K \frac{\pi}{6}$ and:

$$x' \equiv x_G - uh / (KD^{1/2}) \quad (6.17a)$$

$$t' \equiv t - h / (KD^{1/2}) \quad (6.17b)$$

which are based on the drop trajectory arguments leading to Equations (6.10) and (6.11). The convolution of the DSD in Equation (6.16) is a consequence of summing (integrating) over D , resulting in a time delay $\Delta t = h / (K D^{1/2})$ due to fall height and terminal velocity. The complete description of gauge rainfall, using Equations (6.16), (6.17), and (6.5) is:

$$\begin{aligned} R_G(x, t) &= K' \int_0^{\infty} D^{7/2} N[D; R(x', t')] dD \\ &= 8000K' \int_0^{\infty} D^{7/2} \exp[-4.404 R^{-2/9}(x', t') D] dD \\ &= 8000K' \int_0^{\infty} D^{7/2} \exp\left[-4.404 R^{-2/9}\left(x - \frac{uh}{K D^{1/2}}, t - \frac{h}{K D^{1/2}}\right) D\right] dD \end{aligned} \quad (6.18)$$

where x is any arbitrary point on the ground where a gauge might be located. Equation (6.18) is evaluated using numerical integration procedures. For purposes of simulation, the cloud rainfall rate $R(x, t)$ will be described by Equation (6.6).

6.2.2 Radar Reflectivity Model

Radar reflectivity is calculated in a manner similar to rainfall rate. In this simplified CR model, the y dependence is ignored and we assume there is no variation of the DSD, rainfall rate, or radar reflectivity along the y axis. Starting with Equations (6.16) and (6.17) as a guide, the 6th moment of the DSD is calculated at a point (ρ, θ) within the radar cross-section, as shown in Figure 6-2:

$$Z(x, t) = \frac{1}{\pi \rho_0^2} \int_0^{2\pi} \int_0^{\rho_0} \int_0^{\infty} D^6 N[D; R(x'', t'')] dD d\rho d\theta \quad (6.19)$$

x'' and t'' are similar to x' and t' described by Equations (6.17), but instead of evaluating the DSD convolution at a gauge point on the ground at $x = x_G$ and $z = 0$, the points of evaluation are now within the cross-section, at $x = x_G + \rho \cos \theta$ and $z = z_0 + \rho \sin \theta$. The x'' and t'' in Equation (6.19) now become:

$$x'' \equiv x_G + \rho \cos \theta - \frac{u(h - z_0 - \rho \sin \theta)}{K D^{1/2}} \quad (6.20a)$$

$$t'' \equiv t - \frac{h - z_0 - \rho \sin \theta}{K D^{1/2}} \quad (6.20b)$$

where again, x_G has been replaced by x since the gauge location can be at any point along the ground.

6.3 Simulation of Z versus R

The Convolution Rainfall model consists of three basic computational steps for every value of time t :

- 1) Simulation of a cloud DSD based on a cloud rainfall $R(x, t)$, using Equation (6.6).

- 2) Simulation of rainfall $R_G(x, t)$ at a gauge site $x = x_G$, using Equations (6.16) and (6.17).
- 3) Simulation of radar reflectivity $Z(x, t)$, centered above a gauge site at $x = x_G$, using Equations (6.19) and (6.20).

The equations used in steps 2 and 3 are calculated using numerical approximations, based on converting integrals to discrete sums, and the example parameters shown in Table 6-1.

A simulated Z - R relation is generated by calculating a Z - R pair for each time step t , using steps 1 through 3. After many Z - R points are generated, a linear regression is performed to determine a power-law fit, as shown by Equations (6.8). If advection and gravitational effects are minimized, the Z - R parameters of the simulation will converge to the values contained in Equation (6.8b). Otherwise, the Z - R coefficients can be very different, depending on the overall effects of advection and drop sorting.

Table 6-1. Convolution model (CR) example simulation parameters

<i>Parameter Name</i>	<i>Parameter Description</i>	<i>Units</i>	<i>Parameter Value</i>
R0	R_0 , maximum rainfall rate of $R(x, t)$	mm h ⁻¹	100
A	temporal Gaussian width of $R(x, t)$	s	300
B	spatial Gaussian width of $R(x, t)$	m	1000
t0	t_0 , center of temporal Gaussian of $R(x, t)$	s	0
x0	x_0 , center of spatial Gaussian of $R(x, t)$	m	0
u	u , advection velocity	m s ⁻¹	10
h	height of $N(D; R)$ (cloud height)	m	3000
Rr	radar range	m	50000
xG	x_G , gauge location	m	6000
elev	radar scan elevation angle	degrees	0.5
MD	number of D integration steps	--	100
DD	ΔD , integration step-size	mm	0.1
Nrho	number of ρ integration steps	--	50
Ntheta	number of θ integration steps	--	50

6.3.1 Point Z at Gauge Location

The WSR-88D beam width of 1.0° is used in the example CR simulations. In order to approximate $Z(x, t)$ at a point directly at the gauge site, the following change is made to the parameter control file of Table 6-1: *set radar range*, $R_r \approx 0$. Depending on the way the equations specified by steps 1 through 3 of the previous section are implemented in software, it may be necessary to avoid setting simulation parameters, such as R_r to zero. This is to avoid a *divide by zero* error. In this case, it is sufficient to substitute very small non-zero values.

Figures 6-3 through 6-6 are the simulated Z - R values and corresponding linear regression fits, using the example values of Table 6-1, and the approximation of a point Z - R above the gauge. These plots simulate the Z - R relation measured by a disdrometer, which is essentially a point measurement of Z and R . Each of these four simulation plots correspond to a different value of gauge location, with everything else the same as specified by Table 6-1, with the exception of range, $R_r \approx 0$.

6.3.2 Volume Z Over Gauge Location

Figures 6-7 through 6-10 are the simulated Z - R values and corresponding linear regression fits, using the example values of Table 6-1, with a typical radar range $R_r = 50$ km. These plots simulate the Z - R relation measured by a gauge and WSR-88D (essentially a volume averaged measurement of Z). Each of the four simulation plots again correspond to different values of gauge locations x_G , with everything else equal to that specified by Table 6-1. The different x_G locations simulate different types of drop sorting (coupled with advection) which could be seen by radar or a disdrometer, using an identical simulated convective cell system passing overhead.

In both simulation types, the *point* Z - R and *volume* Z - R , linear regression splits into two distinct lines. One possible explanation for this very distinct display of two

different $Z-R$ relations, is the way in which the drop distributions arrive at the ground. A convective cell, as it moves along its advective trajectory, forms large drops directly beneath the cloud, while small drops trail behind and beneath, due to the increase and decrease of rainfall rate at the cloud level. This segregation of drop sizes then leads to a dual $Z-R$. In nature, many other processes are active which tend to smear the dual $Z-R$ split into a distribution of points, which are then fitted to a single $Z-R$ line. These conclusions are very preliminary.

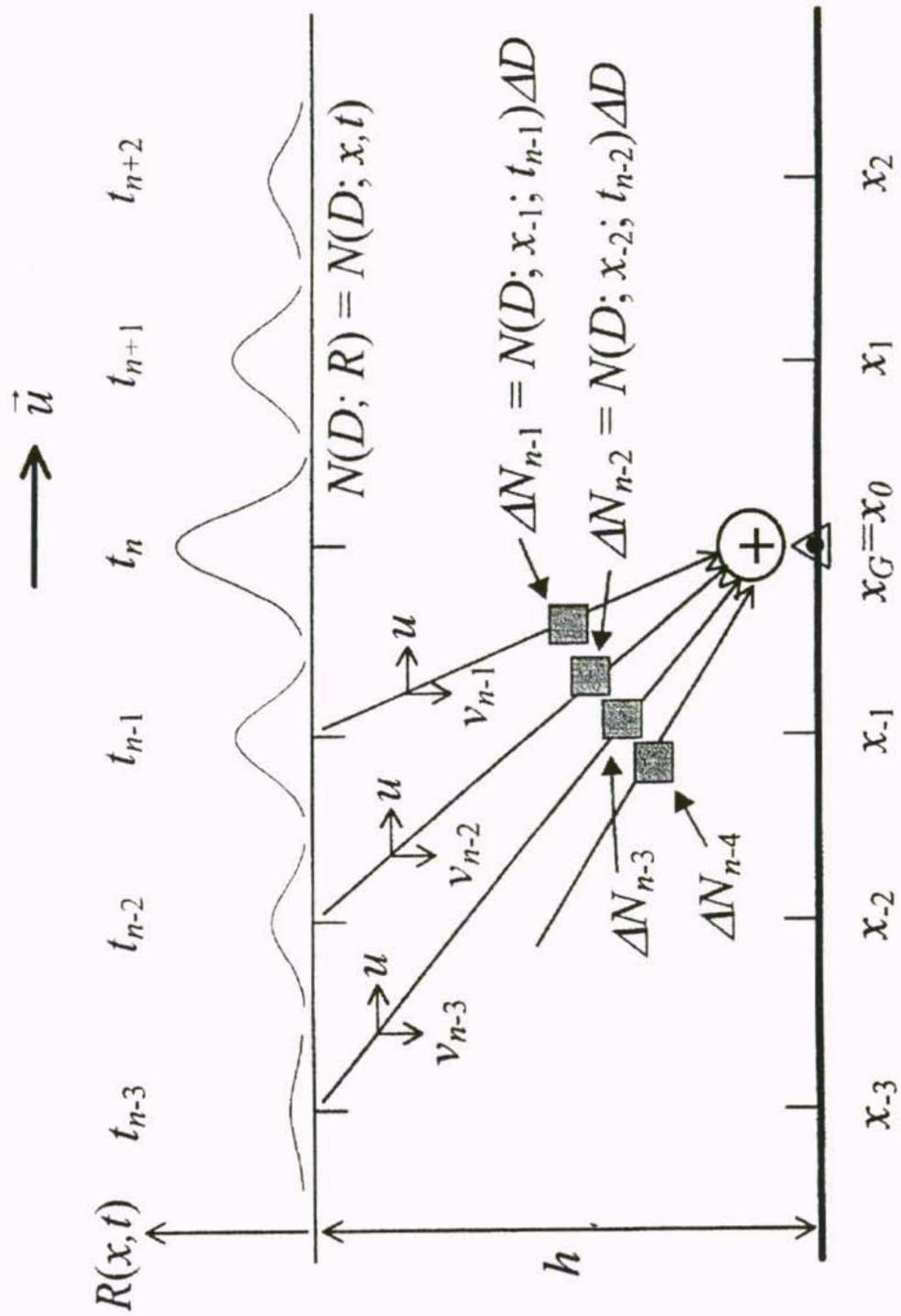


Figure 6-1. Calculated rainfall at gauge site x_G based on convolution of DSD.

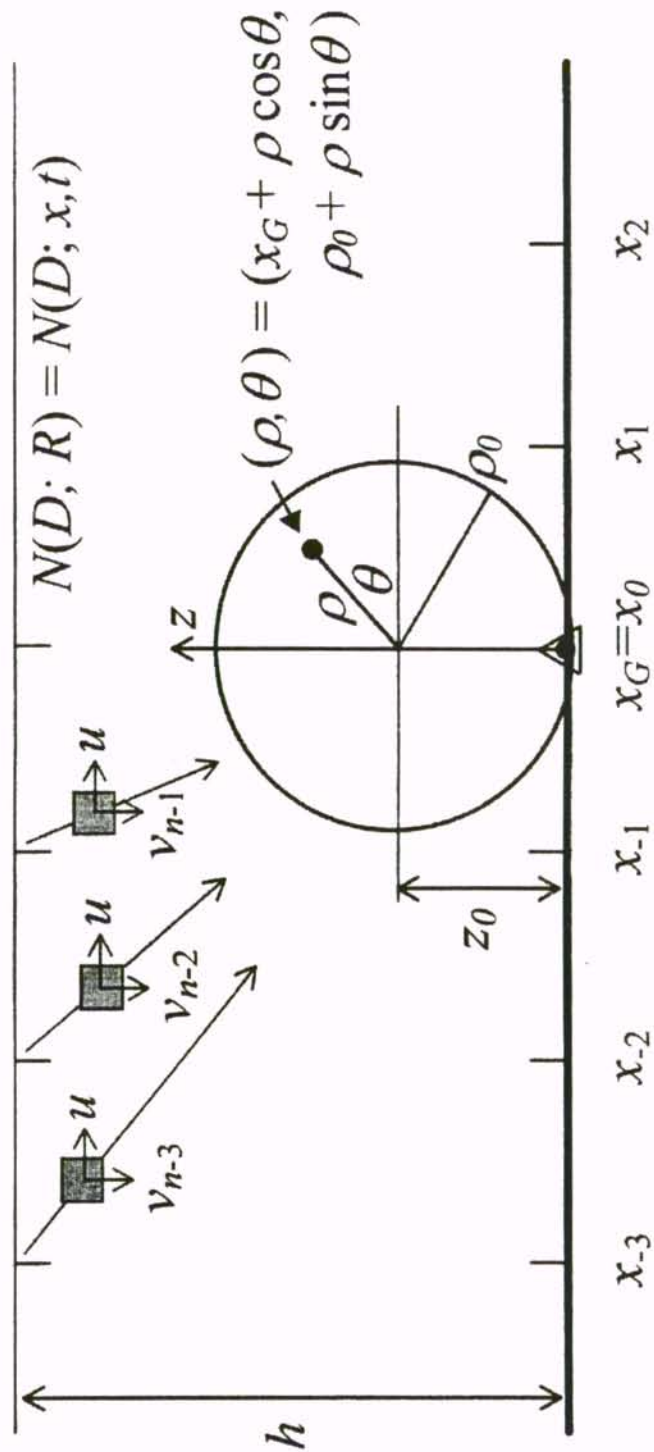


Figure 6-2. Volume integration for radar reflectivity calculation.

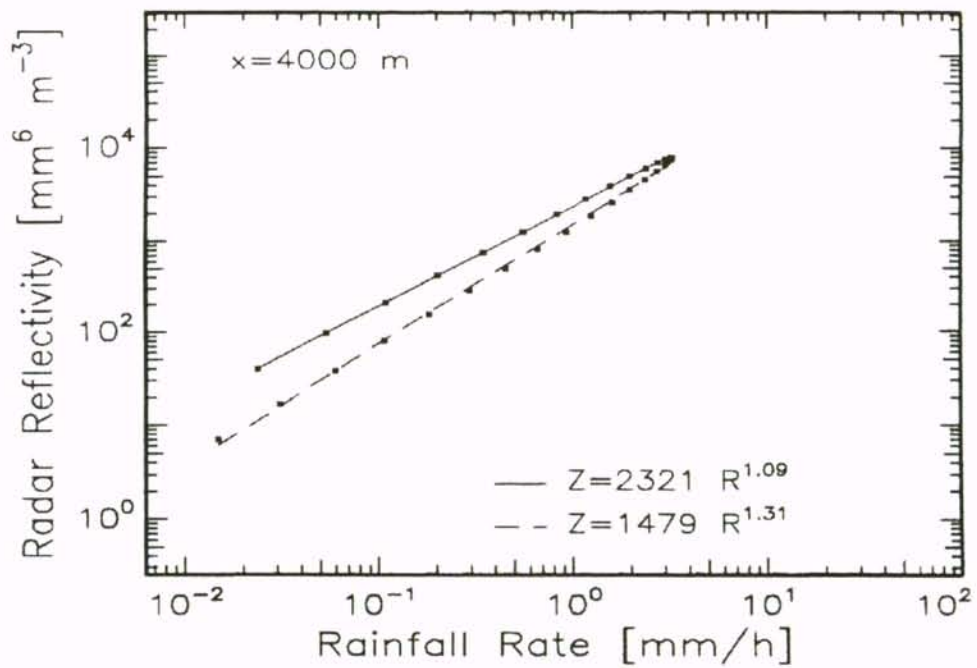


Figure 6-3. Simulated point Z - R at $x_G = 4 \text{ km}$.

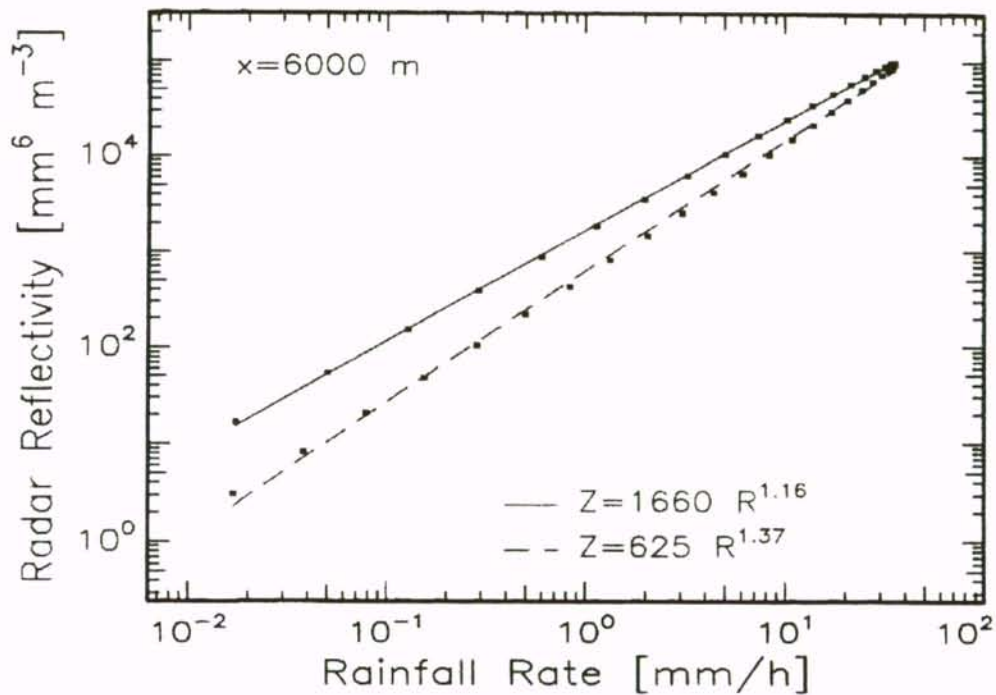


Figure 6-4. Simulated point Z - R at $x_G = 6 \text{ km}$.

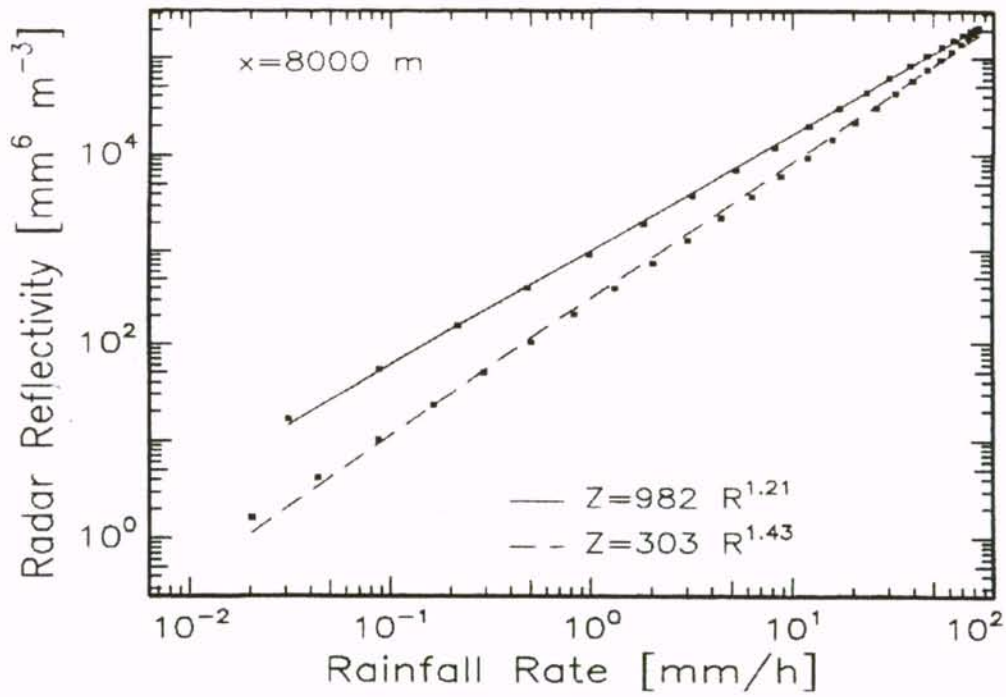


Figure 6-5. Simulated point $Z-R$ at $x_G = 8 \text{ km}$.

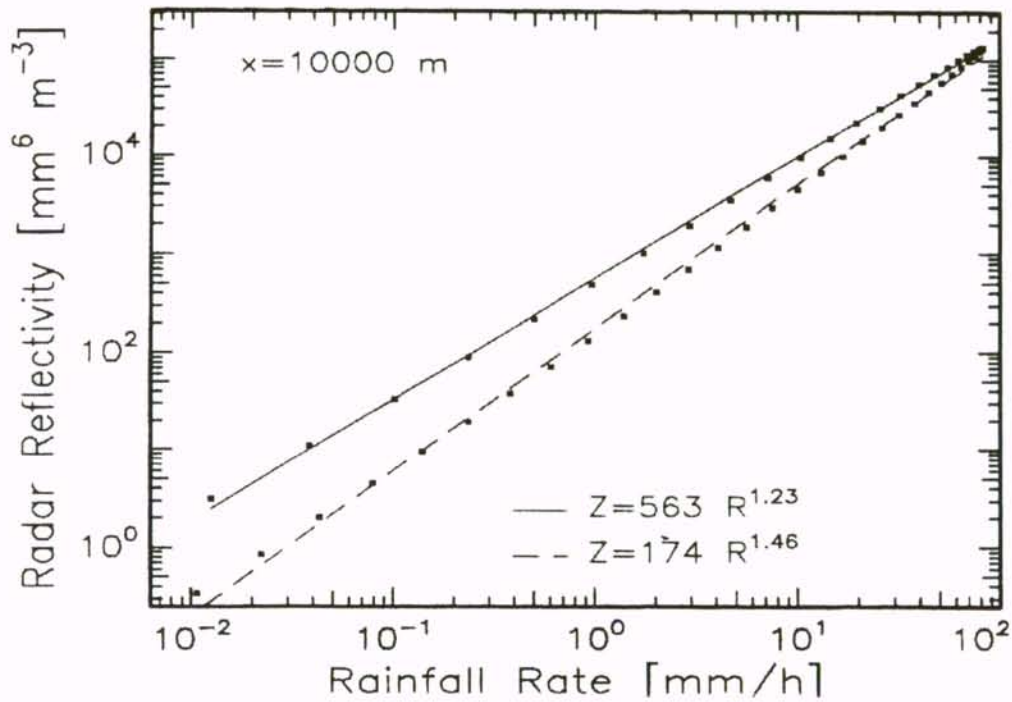


Figure 6-6. Simulated point $Z-R$ at $x_G = 10 \text{ km}$.

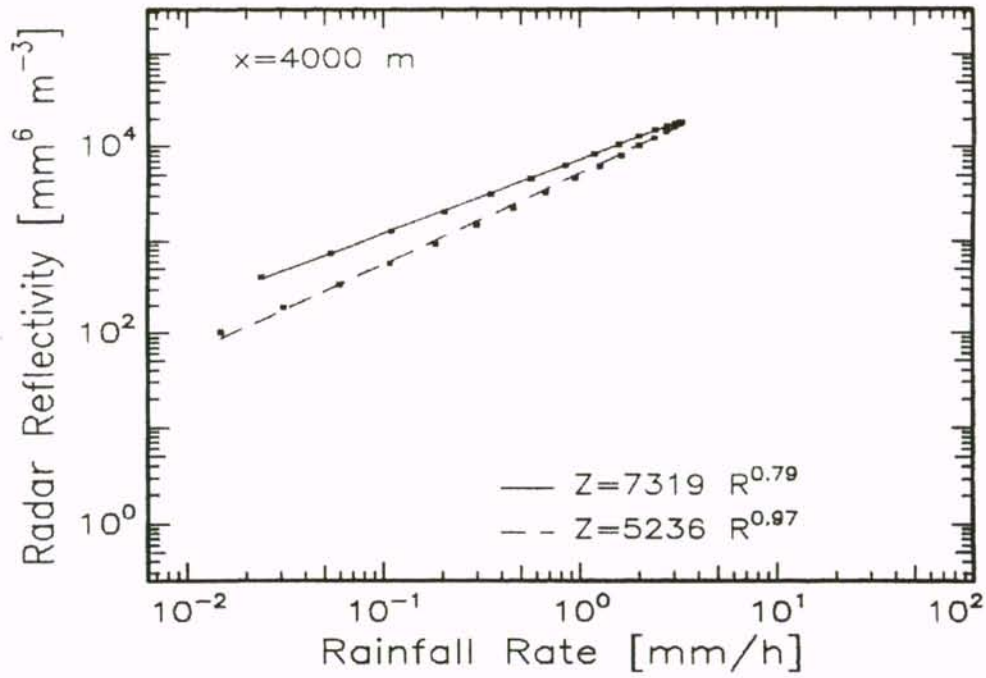


Figure 6-7. Simulated volume Z - R at $x_G = 4 \text{ km}$.

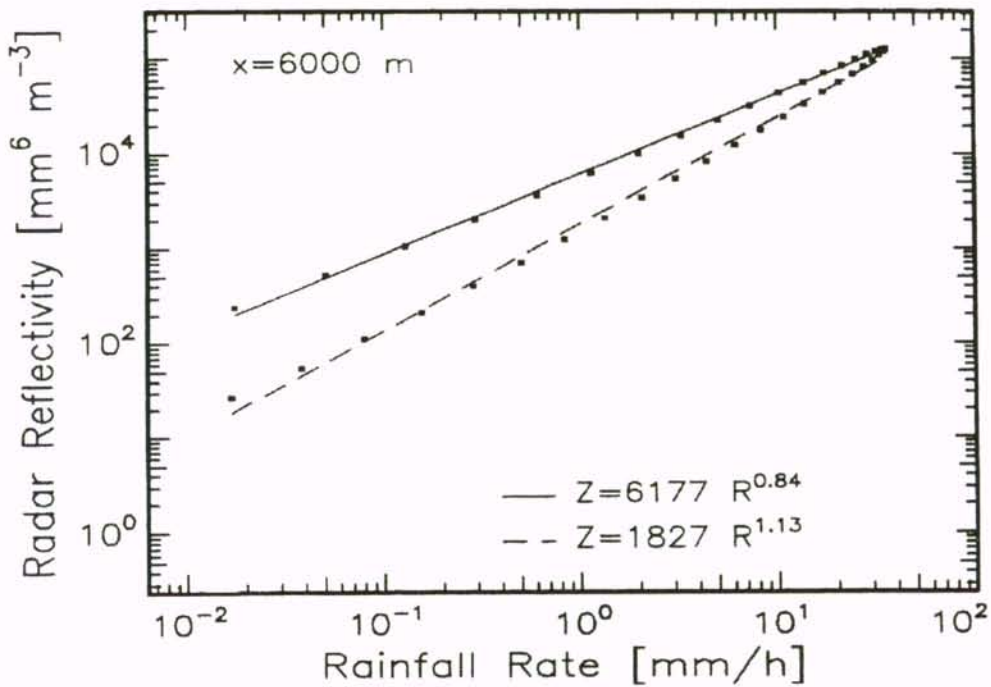


Figure 6-8. Simulated volume Z - R at $x_G = 6 \text{ km}$.

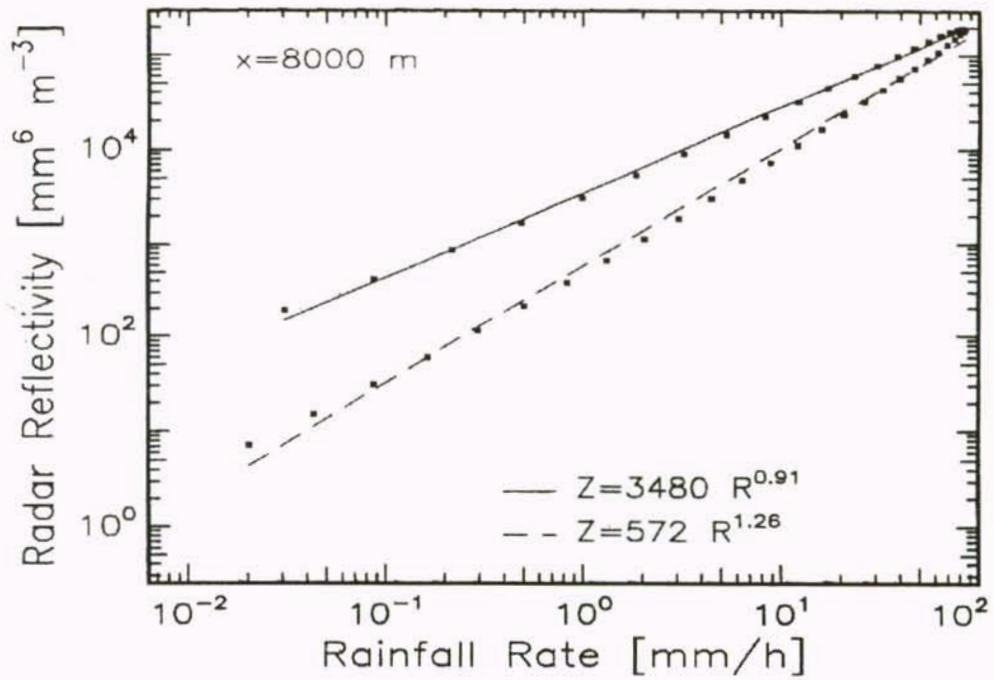


Figure 6-9. Simulated volume Z - R at $x_G = 8 \text{ km}$.

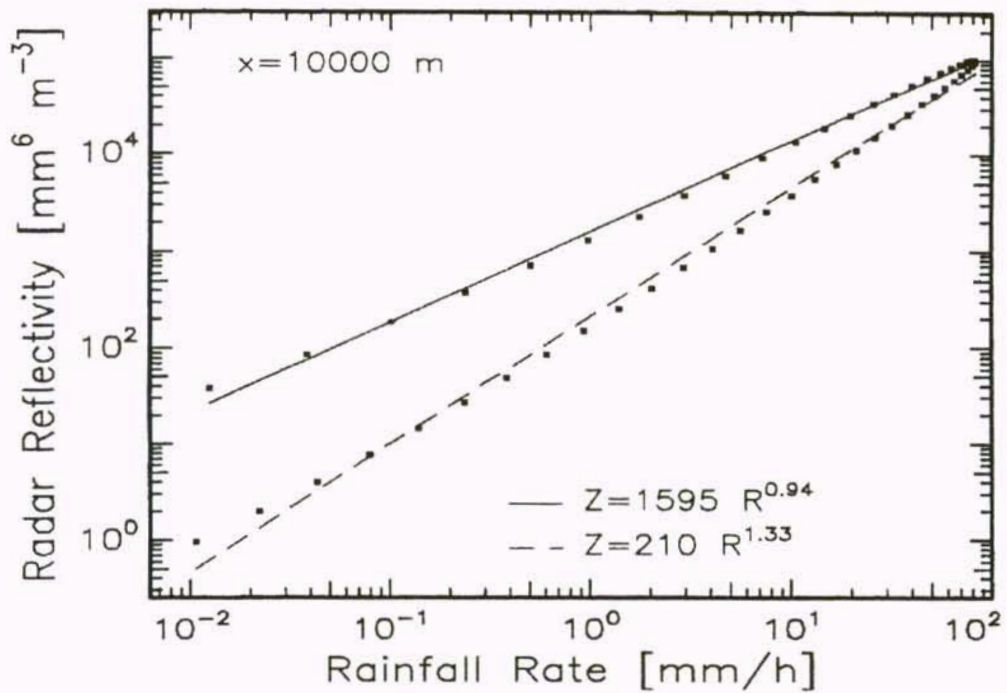


Figure 6-10. Simulated volume Z - R at $x_G = 10 \text{ km}$.

CHAPTER 7

MICROSCALE Z-R ANALYSIS

7.1 Background

A major objective of NASA's Tropical Rainfall Measurement Mission (TRMM) is to improve rainfall estimates using satellite and ground based radar remote sensing methods. For the TRMM ground validation program, NASA will process radar data from the National Weather Service's network of WSR-88D radar (NEXRAD) using a Z - R relationship that transforms radar reflectivity into rainfall rate. Previous Z - R models relate rainfall rates to radar reflectivity through a non-linear relationship based on model parameters that are constant throughout the radar image. Recent work has extended this concept to include parameterization based on range, and to apply different Z - R relationships based upon the classification of rainfall regime into convective and stratiform precipitation types^[14].

Strategies for estimating rainfall amounts from weather radar reflectivity data have traditionally taken different paths. One path is the statistical approach such as the Probability Matching Method (PMM)^[30], where large areal averages and long time intervals (days to months) are used to give an averaged Z - R relation. One such relation^[29] between radar reflectivity Z and rainfall rate R used by the National Weather Service (NWS), is $Z=300R^{1.4}$ where Z is in units of $\text{mm}^6 \text{m}^{-3}$ and R is in units of mm h^{-1} . Most research involving Z - R studies tends to approach the problem from the long time interval and large area average perspective^[14]. A second approach is based on optimizing the Z - R relationship, again over large areas, but using short time intervals

(minutes to hours) for real-time applications such as flood warnings. This approach is often associated with Kalman filtering^[26], a recursive optimization algorithm used to adjust the Z - R coefficients based on the instantaneous readings from a network of rain gauges. Even though there has been a fair amount of work in the area of real-time rainfall estimation algorithms, few practical results have made it into NWS operations. A third direction of research considers the problem from the point of view that more information is needed. More information can be supplied by polarimetric radar^[25] or ground based disdrometers^[13]. Strategies of extracting additional radar reflectivity information from the standard NEXRAD dataset, or *base product*, were investigated. Some of the techniques employed are common image processing problem solutions, such as two-dimensional cross-correlation for extracting advection velocity^[28].

Two directions were considered. First, using base scan reflectivity data, or a composite of vertical scans, a time derivative of Z has been constructed. In this way, rainfall rate R becomes a function of both reflectivity Z and the total time derivative of reflectivity \dot{Z} . A second method, using the complete volume scan, constructs a time derivative of movement of a constant Z level in the vertical direction, or \dot{z} . This vertical velocity $W_z \equiv \dot{z}$ may be closely coupled to the vertical wind velocity, thus affecting the drop terminal velocities^[40,41]. With this approach, R becomes a function of both Z and W_z .

7.2. Mathematical Development

The *exponential* drop size distribution model approximates the number of drops per unit volume of air, per drop size interval D , and can be expressed as:

$$N(D) = N_0 e^{-\Lambda D} \quad (7.1)$$

The number of drops as a function of drop size which exit or enter a unit volume of air is termed the *flux density* of rain. This quantity is experimentally measured as the number of drops as a function of drop diameter that strike a horizontal surface:

$$n(D) = v_D N(D) \quad (7.2)$$

where v_D is the drop velocity. For the purpose of this derivation, we will assume that all rain drops that strike a horizontal surface on the ground can be considered to be traveling at their terminal velocity.

7.2.1 The \dot{Z} Model

During conditions of the onset of rain at $t = 0$, the drop size distribution can be approximated as a Marshall-Palmer^[16] (MP) DSD at the cloud level H above the ground. The Marshall-Palmer DSD is a special case of the *exponential distribution*, Equation (7.1), with $N_0 = 8000 \text{ m}^{-3} \text{ mm}^{-1}$ and $\Lambda = 4.1R^{0.21} \text{ mm}^{-1}$, with R in units of mm h^{-1} . At $t = 0$, $N(D) = \text{MP-DSD}$ for $z = H$, and $N(D) = 0$ for $z < H$. Approximating drop terminal velocity^[21] for ease of analysis by $v_D \approx K_G D^{1/2}$, where $K_G = 4.5$, leads to the following expression for lower drop diameter cut-off for $z < H$ and $t > 0$:

$$D_L(z, t) = \left(\frac{H}{K_G t} \right)^2 \left(1 - \frac{z}{H} \right)^2 \quad (7.3)$$

where z is a vertical distance measured from the ground. Radar reflectivity is calculated as the 6th moment of the DSD, integrated over the radar cross-section $A = \pi h^2 / 4$, where for simplicity, it will be assumed that the cross-sectional volume is a cylinder of length $\Delta R = 1 \text{ km}$ and area A :

$$Z = \frac{8}{\pi h^2} \int_0^h \sqrt{(h/2)^2 - (z - h/2)^2} \int_{D_L(z,t)}^{\infty} D^6 N(D) dD dz \quad (7.4)$$

Note that Equation (7.4) assumes a base scan with a beam center height of $h/2$. The expression under the square root symbol is the differential area dA of the cross-section A as a function of height z above the ground. The integral of this term from 0 to h over dz is equal to $A/2 = \pi h^2/8$.

Using Gunn's terminal velocity formula, the equivalent expression for rainfall rate is:

$$R = \frac{4K_G}{3 h^2} \int_0^h \sqrt{(h/2)^2 - (z - h/2)^2} \int_{D_L(z,t)}^{\infty} D^{7/2} N(D) dD dz \quad (7.5)$$

If the height at the top of radar cross section h is much less than the cloud height H , $h \ll H$, then $D_L(z,t) \approx (H/K_G t)^2$. In this case, along with the simplifying assumption that $N(D)$ is uniform throughout the radar cross-section, expressions for Z and R are:

$$Z = N_0 \Lambda^{-7} \Gamma\left(7, \frac{H^2 \Lambda}{K_G^2 t^2}\right) \text{ mm}^6 \text{ m}^{-3} \quad (7.6)$$

$$R = 0.0006 \pi K_G N_0 \Lambda^{-9/2} \Gamma\left(\frac{9}{2}, \frac{H^2 \Lambda}{K_G^2 t^2}\right) \text{ mm h}^{-1} \quad (7.7)$$

The total time derivative of Z can be computed as:

$$\begin{aligned} \dot{Z} &= N_0 \Lambda^{-7} \frac{d}{dt} \Gamma\left(7, \frac{H^2 \Lambda}{K_G^2 t^2}\right) \\ &= 2N_0 \left(\frac{H}{K_G t}\right)^{14} \frac{e^{-\Lambda(H/K_G t)^2}}{t} \end{aligned} \quad (7.8)$$

where $\Gamma(x, a)$ is the *incomplete gamma function*. Equations (7.6) through (7.8) can be plotted parametrically, eliminating Λ , as shown in Figure 7-1 with an arbitrary choice of $H = 3000$ m. This plot defines R in terms of Z and \dot{Z} , $R = R(Z, \dot{Z})$.

7.2.2 The W_Z Model

The relationship between terminal velocity and drop diameter can be approximated with greater accuracy by an empirical formula^[23]:

$$v_D \approx v_0(1 - K e^{-cD}) \quad (7.9)$$

where $v_0 = 9.65 \text{ m s}^{-1}$, $K = 1.067$, $c = 0.6 \text{ mm}^{-1}$, and D is expressed in mm. If vertical updraft velocity W reduces the terminal velocity, Equation (7.9) becomes:

$$\begin{aligned} v_D &\approx v_0(1 - K e^{-cD}) - W \\ &= v_w(1 - K_w e^{-cD}) \end{aligned} \quad (7.10a)$$

where,

$$v_w \equiv v_0 - W \quad (7.10b)$$

$$K_w \equiv \left(\frac{v_0}{v_0 - W} \right) K \quad (7.10c)$$

A drop diameter D_w corresponding to a terminal velocity of zero is defined from Equation (7.10a) as:

$$v_D = v_w(1 - K_w e^{-cD_w}) = 0 \quad (7.11)$$

so that,

$$D_w = \begin{cases} \frac{1}{c} \ln K_w & K_w > 1 \\ 0 & K_w \leq 1 \end{cases} \quad (7.12)$$

Combining Equations (7.8) and (7.10a) yields:

$$n(D) \approx v_w (1 - K_w e^{-cD}) N(D) \quad (7.13)$$

The *rainfall rate distribution* is the product of the drop volume and flux density distribution, where a spherical drop volume is assumed (even though drops at terminal velocity tend to be more elliptical due to the frictional drag of air). The total rainfall rate R is the integral of $R(D)$ over all possible diameters which result in a *positive downward terminal velocity* :

$$R = v_w \frac{\pi}{6} \int_{D_w}^{\infty} (1 - K_w e^{-cD}) D^3 N(D) dD \quad (7.14)$$

A scale factor must be added to express R into standard units of mm/h. Noting that the incomplete gamma function $\Gamma(D, D_w)$ must, in general, be determined numerically:

$$R = v'_w N_0 \Lambda^{-4} \left[\Gamma(4, \Lambda D_w) - \frac{K_w \Lambda^4}{(c + \Lambda)^4} \Gamma(4, D_w (c + \Lambda)) \right] \quad (7.15a)$$

where,

$$v'_w = (0.0036) v_w \pi / 6 \quad (7.15b)$$

Radar reflectivity Z is the *6th moment* of the DSD:

$$\begin{aligned} Z &= \int_{D_w}^{\infty} D^6 N(D) dD \\ &= \Lambda^{-7} N_0 \Gamma(7, \Lambda D_w) \end{aligned} \quad (7.16)$$

Equations (7.15a) and (7.16) are plotted parametrically, eliminating Λ , as shown in Figure 7-2. This plot defines R in terms of Z and W , $R = R(Z, W)$. The incomplete

gamma functions of Equations (7.15a) and (7.16) can be evaluated analytically as follows:

$$\Gamma(4,a) = \frac{a^3 + 3a^2 + 6a + 6}{e^a} \quad (7.17)$$

$$\Gamma(7,a) = \frac{a^6 + 6a^5 + 30a^4 + 120a^3 + 360a^2 + 720a + 720}{e^a} \quad (7.18)$$

NEXRAD radar reflectivity $Z_n(x,y,z)$ can be expressed in a three-dimensional Cartesian coordinate system, where the time interval index n corresponds to a complete volume scan time interval of approximately 5 min. In the presence of rain, an arbitrary constant reflectivity Z level can be measured as a function of altitude z above the ground at point $\{x, y\}$ and at time interval n . A 30 dBZ reflectivity is a convenient Z value to follow as a function of z and t where the discrete time index n is interpolated to provide the continuous variable t . The basis of the W_Z model is a proposed relationship between vertical velocity $W(t)$, and the time derivative of the 30 dBZ level $W_Z(t)$:

$$W(t) = \gamma W_Z(t - t_0) \quad (7.19)$$

where γ is an empirical scaling factor and t_0 is a delay time related to the average fall time of drops. A zeroth order approximation of the delay time is to describe t_0 by an average fall distance divided by an average terminal velocity, $t_0 \approx \bar{h} / \bar{v}_D$. The fall distance might be proportional to the 30 dBZ altitude above the ground, $z_{30\text{dBZ}}$, while the average terminal velocity would roughly correspond to the velocity of mid to large drop sizes.

7.3. Experimental Results

Figure 7-3 shows a UCF rain gauge test site consisting of a triad of rain gauge locations, with a separation of approximately 1.3 km . This was a temporary site in southwest Palm Bay, east of the St. John's River basin, and about 21 km SSW of the Melbourne NEXRAD (KMLB). Each rain gauge location within the cluster consisted of a tipping bucket, accumulation rain gauge, and one UCF acoustic disdrometer.

KMLB reflectivity of the lowest elevation scan equal to 0.5° , is shown in Figure 7-4 for four consecutive time frames, beginning at 19:13:53 UTC (the center of the beam is approximately 209 m above the rain gauges at a range of 21 km). Each plot displays a 16 x 16 km section, approximately centered about the rain gauge test site. Reflectivity Z is plotted as a polar projection of the 0.5° scan's original spherical coordinates. The Z plots are filled with a spatial interpolation over x and y , based on Shepard's formula^[9].

7.3.1. Predicted Vertical Velocity

Using the Z interpolation formula from Equation (7.29), the average Z in the circle of radius $r_0 = 1$ km centered around the rain gauge cluster, is computed for the lowest elevation, $k = 1$ sweep:

$$Z_A(t) \equiv \frac{\int_0^{2\pi} \int_0^{r_0} Z_1(x, y, t) d\theta r dr}{\int_0^{2\pi} \int_0^{r_0} d\theta r dr} \quad (7.20)$$

$Z_A(t)$ is plotted in Figure 7-5 as a dotted line. Similarly, the rain gauge data from the gauge cluster is interpolated using Equation (7.32), then averaged over the circle of radius 1 km:

$$R_A(t) \equiv \frac{\int_0^{2\pi} \int_0^{r_0} R(x, y, t) d\theta r dr}{\int_0^{2\pi} \int_0^{r_0} d\theta r dr} \quad (7.21)$$

The average $R_A(t)$ is plotted as open circles in Figure 7-5. Using an iterative numerical procedure, for each Z_A, R_A pair, a W is found by equating Z_A to the right hand side of Equation (7.16) and by equating R_A to the RHS of Equation (7.15a), and eliminating Λ . This can be accomplished using the plot in Figure 7-2 by locating the corresponding W for an R, Z pair. As a check, the resulting W 's are substituted back into Equation (7.15a), and R is plotted as a solid line in Figure 7-5. The subsequent W 's are plotted in Figure 7-6, resulting in a predicted time dependent vertical velocity $W(t)$, averaged over the circle of radius r_0 . The result is a prediction of rainfall rate using the Z - R relation specified by Equations (7.15a) and (7.16). In this way, the predicted radar rainfall rate exactly matches the gauge rainfall rate when averaged over the gauge cluster area.

7.3.2. Measurement of W_Z

The center of the circle surrounding the gauge site is located at $r_0 = \{x_0, y_0\} = \{1.65, 1.65\}$ km, using a Cartesian coordinate system local to the rain gauge site. At several selected points within the circle, $\vec{r}_r = \{x_r, y_r\}$, $Z_k(x_r^-, y_r^-, t)$ and $Z_k(x_r^+, y_r^+, t)$ are calculated from Equation (7.29), where:

$$\vec{r}_r^\pm = \{x_r^\pm, y_r^\pm\} = \vec{r}_r \pm \frac{1}{2} \bar{u} \Delta t \quad (7.22)$$

$Z_k(x_1^-, y_1^-, t)$ and $Z_k(x_1^+, y_1^+, t)$ are plotted for $k = 1 \dots 12$, in Figures 7a and 7b, respectively, where $\vec{r}_1 = \{x_1, y_1\} = \{1.0, 1.0\}$, $\Delta t = 30$ s, and $\bar{u} = \{32, 30^\circ\}$ km/h. Note that $Z \approx 0$ $k > 12$, corresponding to clear air. Figure 7-8a is a plot of $z_{30dBZ}^-(t)$ and

$z_{30dBZ}^+(t)$, corresponding to the altitude of the 30 dBZ reflectivity above points \vec{r}_1^- and \vec{r}_1^+ . The distance from the radar site to the point of interest on the ground S , the scan elevation angle λ , and radar range ρ , determine the height of the beam center above the ground¹ ($R_e \approx 8500$ km is 4/3 average earth radius):

$$\rho \approx \frac{S}{\cos \lambda} \quad (7.23a)$$

$$z \approx S \tan \lambda + \frac{S^2}{2R_e} \quad (7.23b)$$

Beam center height, for an example of $S = 21$ km, has been calculated for all elevations of the volume scan in Table 7-1.

The time derivative of the 30 dBZ level is estimated by:

$$\dot{z}_1(t) \approx \frac{z_{30dBZ}^+(t) - z_{30dBZ}^-(t - \Delta t)}{\Delta t} \quad (7.24)$$

using the re-sampled data shown in Figure 7-8b. The computation of Equation (7.24) is plotted in Figure 7-9, along with $W(t)$ from Figure 7-6. The above procedure is repeated for several points $\vec{r}_r = \{x_r, y_r\}$ within the gauge cluster. The resulting $\dot{z}_r(t)$ are summed and averaged and then plotted in Figure 7-10 as a dotted line. Finally, Equation (7.19) is applied to this result and plotted as a solid line in Figure 7-10, with a scaling factor $\gamma = 0.5$ and delay time $t_0 = 0.06$ h. The estimated vertical velocity from Equation (7.19) is superimposed with the original $W(t)$ from Figure 7-6, showing a reasonable correlation. The delay time can be attributed to an average fall height of 2 km, and average terminal velocity of 9.25 m/s.

Table 7-1. NEXRAD beam center height at $S = 21$ km

Scan Number	Scan Elevation Angle λ degrees	Height of Beam Center Above Ground z km
1	0.5	0.209
2	1.5	0.576
3	2.5	0.943
4	3.4	1.274
5	4.4	1.623
6	5.4	2.011
7	6.2	2.307
8	7.6	2.828
9	8.7	3.239
10	10.1	3.767
11	12.0	4.490
12	14.1	5.301

7.4. Discussion of Results

The results presented in this chapter demonstrate that a $Z-R$ relation appropriate for microscale size areas and short time intervals, must be described by something more than a simple power-law. Alternate $Z-R$ strategies were investigated which rely on the extraction of additional information from the WSR-88D base product. In the first example, rainfall rate was derived in terms of the base scan reflectivity and total time derivative of reflectivity for the start of a rainfall pulse. In the second example, the vertical velocity of a constant 30 dBZ level was extracted from the volume scan. From this, an updraft/downdraft velocity was predicted from an exponential DSD and shown to be about half the time derivative of the 30 dBZ height. An obvious direction for future work is to combine these two cases into a single functional model, thus, incorporating

vertical velocity and rainfall pulse transients into a rainfall rate R which is a function of three radar observables:

$$R = F(Z, \dot{Z}, f(W_z)) \quad (7.25)$$

Once a useable description of R in terms of radar observables is defined, such as Equation (7.25), standard image processing techniques can then be employed, to convert a sequence of radar volume scans into a map depicting rainfall rates over the entire radar service area. Proposed steps in achieving the final rainfall map might be, for example:

- (1) Segment the radar image into regions of rain using edge detection of precipitation clusters (convective cells for example), where a constant advection can be identified for that region.
- (2) Use two-dimensional cross-correlation of adjacent time scans to determine average advection magnitude and direction in each segmented region.
- (3) Calculate total time derivative of the base scan (or vertical composite) reflectivity, \dot{Z} , for each region.
- (4) Calculate the velocity $W_z \equiv \dot{z}$ of the 30 dBZ level in each region.
- (5) Using a model based on Equation (25), estimate instantaneous rainfall rate in each region.
- (6) Combine regions into a single contiguous rainfall map.

By utilizing additional information contained in the WSR-88D base products, as well as two-dimensional algorithms common to image-processing techniques, accurate real-time estimates of rainfall rates may be possible for microscale areas within the radar service area. The two primary difficulties in achieving this goal is the development of a robust model, such as that outlined by Equation (7.25) and examples given in this paper, and most importantly, the computer power necessary to process the segmented radar data

in real-time. However, as computer power increases exponentially with time, this capability may soon be within reach for implementation within the NWS operations. Fortunately for TRMM applications, processing requirements are not real-time so the problem of computer power is less of an issue.

7.5. Interpolation of Z and R

In order to conveniently work with the discrete values of radar reflectivity Z_{ijkn} , it is necessary to interpolate these values, where i and j represent a point on the ground which can be expressed as longitude and latitude, k is a point above the ground at some elevation, and n is a volume scan time index. Based on Shepard's interpolation formula¹³, one method of reflectivity interpolation, is to replace the \vec{r}_{ijk} vector to the ijk location of Z with a location vector that changes with time based on the advection velocity^[42] \vec{u} :

$$\vec{r}_{ijk} \rightarrow \vec{r}_{ijk} + \vec{u} (t - t_{kn}) \quad (7.26)$$

$$t_{kn} = t_n + (t_{n+1} - t_n) \frac{k}{M} \quad (7.27)$$

where t_n is the start time of the n th volume scan, M is the number of elevations scanned, and t_{kn} is simply the start time of the k th elevation sweep. This procedure is independently followed for each elevation k and volume scan n :

$$\begin{aligned} Z_{kn}(\vec{r}) &\equiv Z_{ijkn} \\ &\rightarrow Z_{kn}(x, y, t) \equiv Z_{kn}(\vec{r} + \vec{u} (t - t_{kn})) \end{aligned} \quad (7.28)$$

Temporal interpolation is then performed by summing over all n sweeps:

$$Z_k(x, y, t) = \frac{\sum_n Z_{kn}(x, y, t) |t - t_{kn}|^{-2}}{\sum_n |t - t_{kn}|^{-2}} \quad (7.29)$$

A similar procedure is followed to spatially interpolate the rain gauge data $R_m(t)$ at locations \vec{r}_m , but now the time variable is replaced as follows:

$$t \rightarrow t - \frac{(\vec{r} - \vec{r}_m) \cdot \vec{u}}{|\vec{u}|^2} \quad (7.30)$$

$$R_m(t) \rightarrow R_m(x, y, t) \equiv R_m\left(t - \frac{(\vec{r} - \vec{r}_m) \cdot \vec{u}}{|\vec{u}|^2}\right) \quad (7.31)$$

where \vec{u} is again the advection velocity of the precipitation system. Spatial interpolation is then performed by summing over all m gauges:

$$R(x, y, t) = \frac{\sum_m R_m(x, y, t) |\vec{r} - \vec{r}_m|^{-2}}{\sum_m |\vec{r} - \vec{r}_m|^{-2}} \quad (7.32)$$

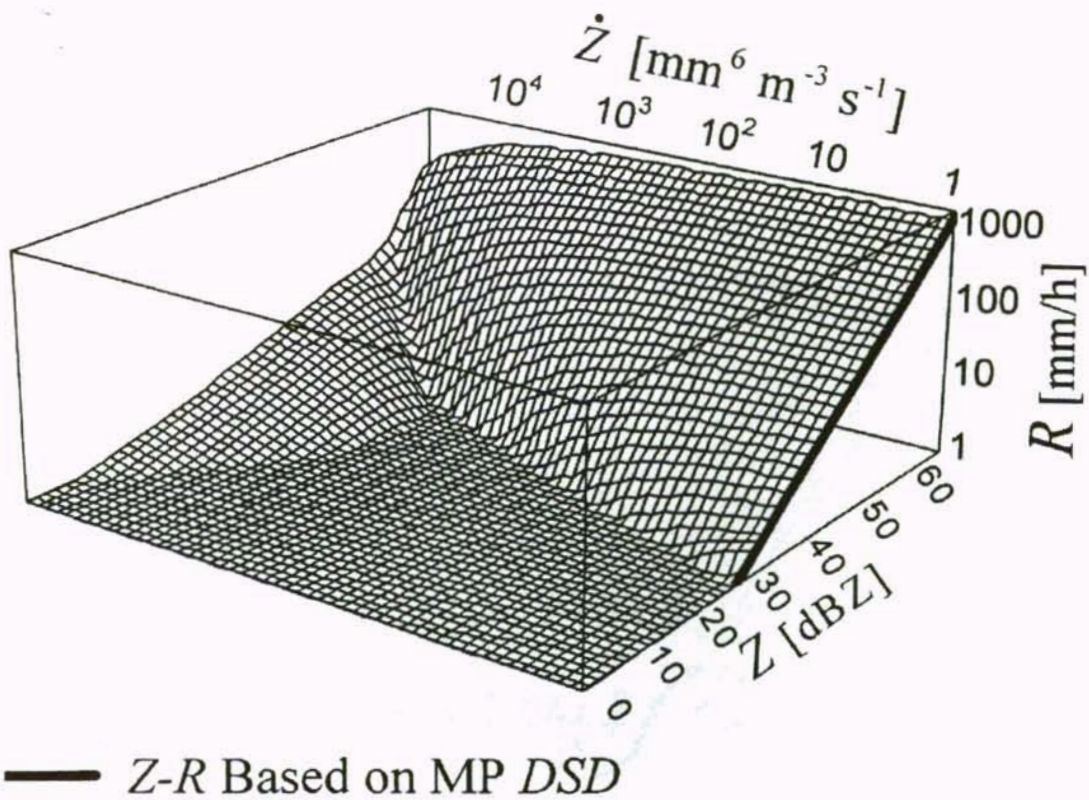
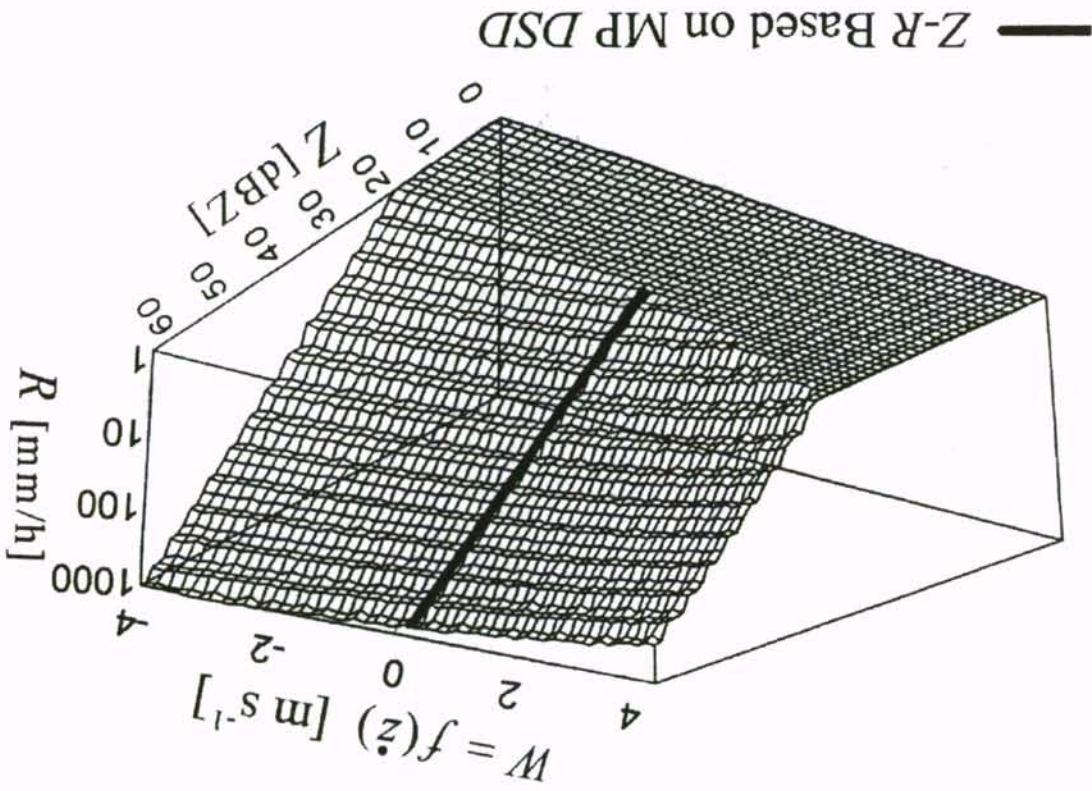


Figure 7-1. \dot{Z} model, $R = R(Z, \dot{Z})$, with $H=3000$ m. Note that plot shows only positive \dot{Z} , corresponding to the onset of a rain pulse. A standard MP Z - R curve results where $\dot{Z} = 0$.

Figure 7-2. W_z model, $R = R(Z, f(W_z))$. A standard MP Z-R curve results where $W = 0$. (The vertical velocity of the 30 dBZ level $W_z \equiv z$).



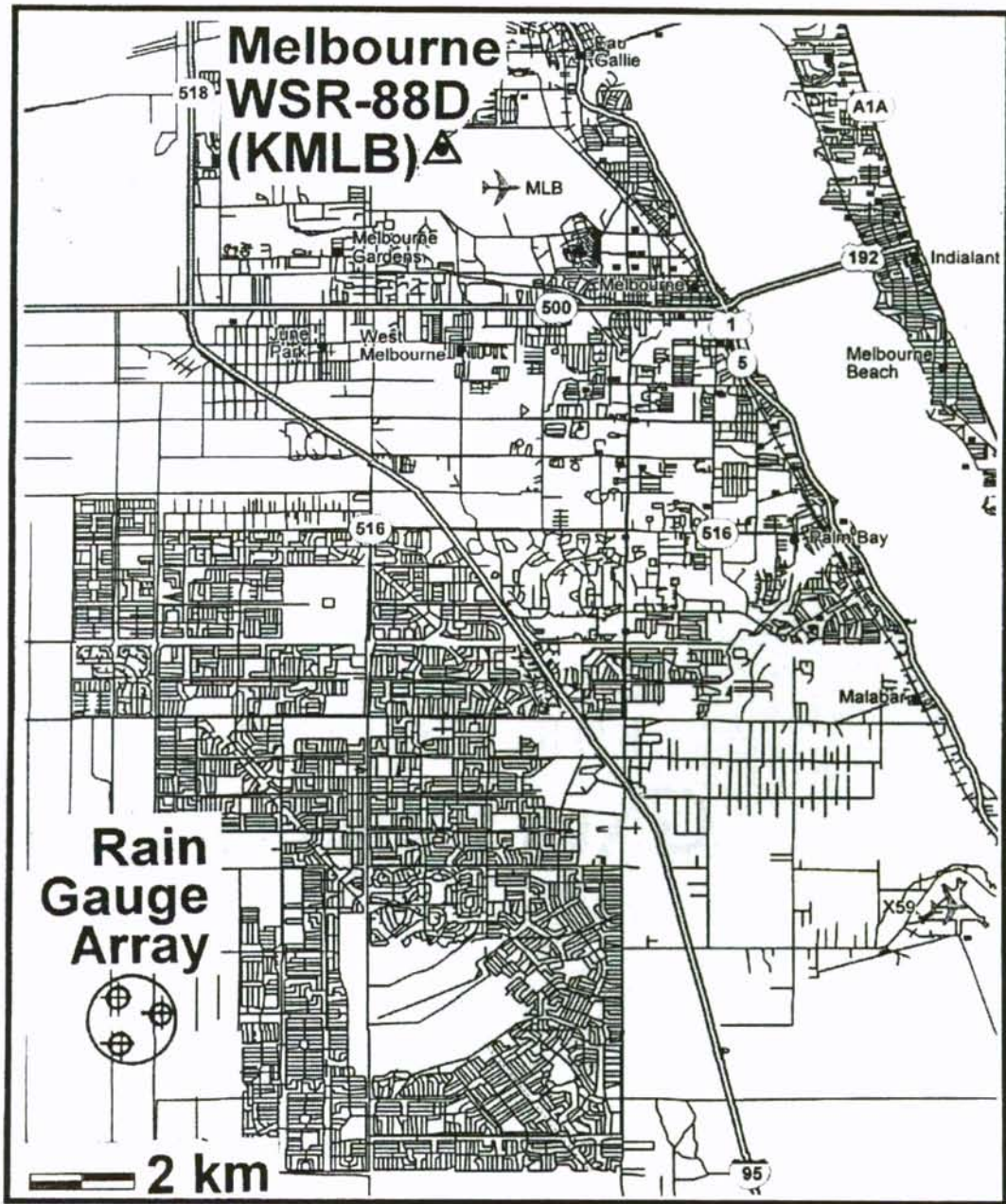


Figure 7-3. Map of rain gauge test site and Melbourne radar. Separation is approximately 21 km.

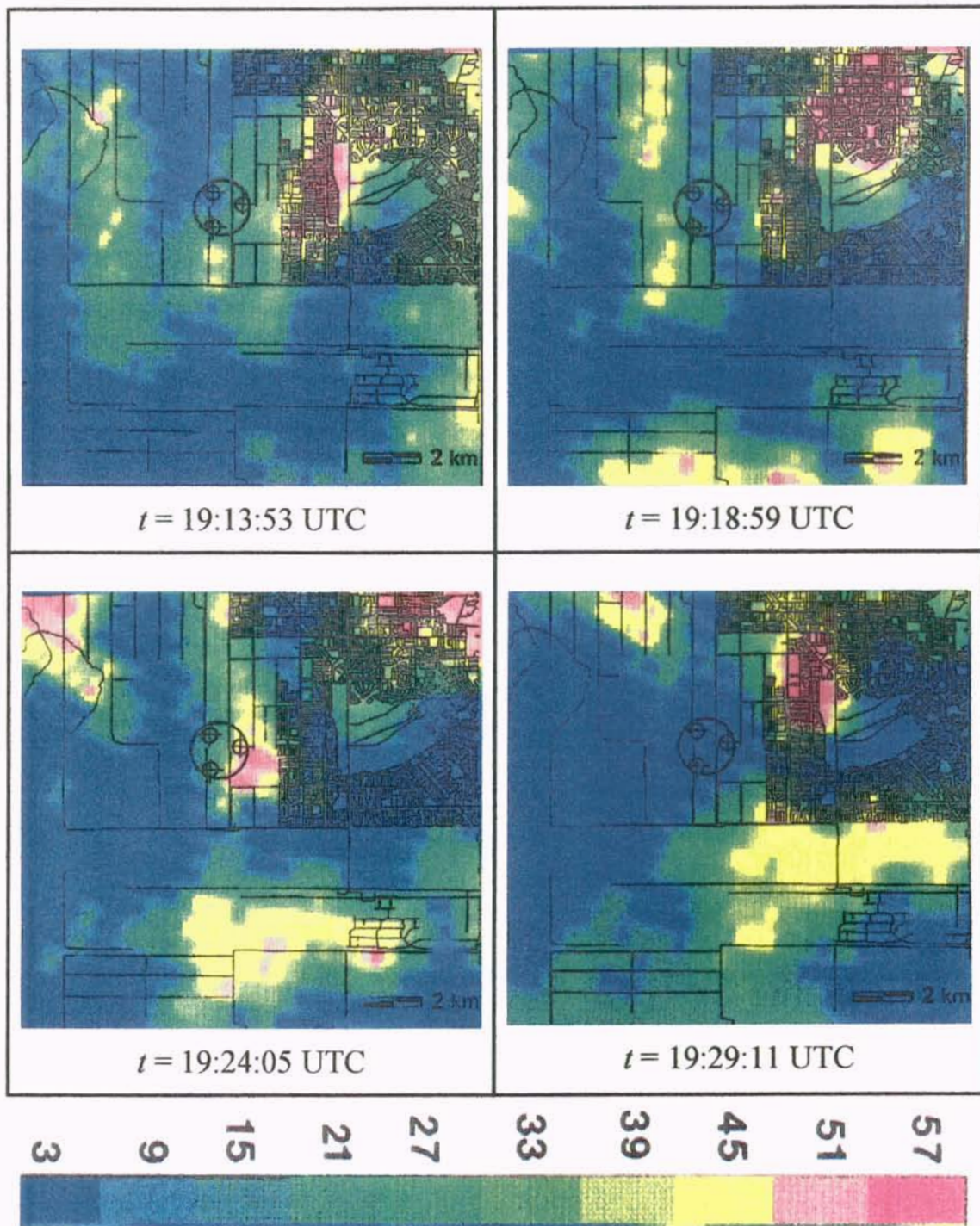


Figure 7-4. Melbourne NEXRAD base scan reflectivity over rain gauge test site, June 1, 1997. Color range is from 3 dBZ (blue) to 57 dBZ (red) in 6 dBZ steps.

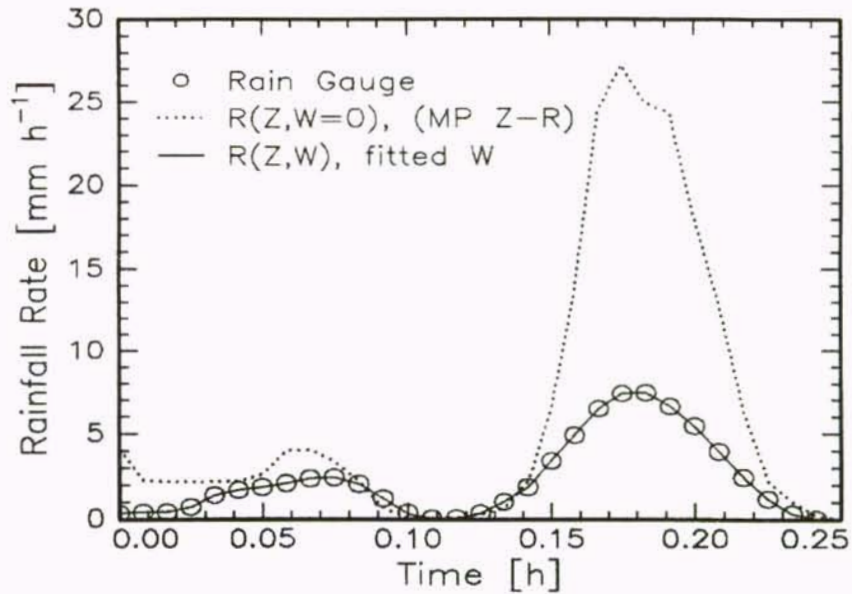


Figure 7-5. Dotted line is spatially interpolated radar rainfall estimate obtained from Figure 7-2 with $W = 0$ (i.e., MP $Z-R$ relation). Open circles are spatially interpolated rain gauge data. Solid line is radar rainfall estimate from Figure 7-2 with appropriate W , forcing an exact fit to rain gauge data.

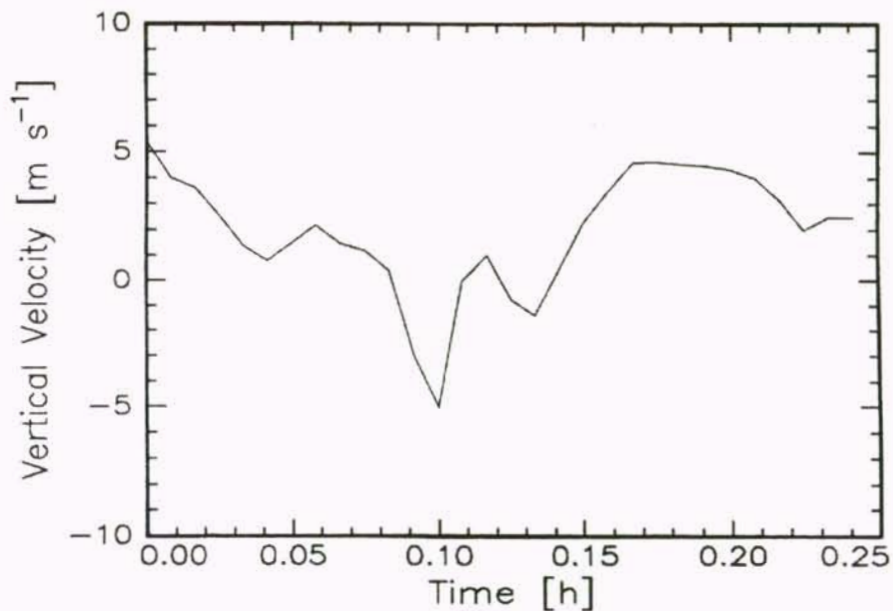


Figure 7-6. Predicted average vertical velocity W over rain gauge test site, based on Figure 7-5, which forces an exact fit of R in Figure 7-2 to the rain gauge data

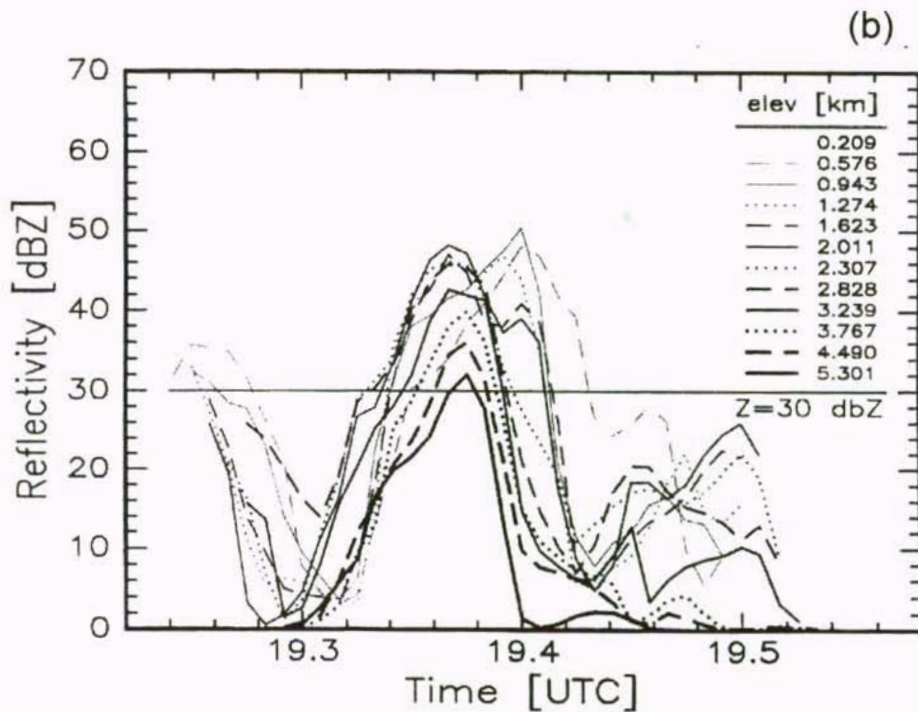
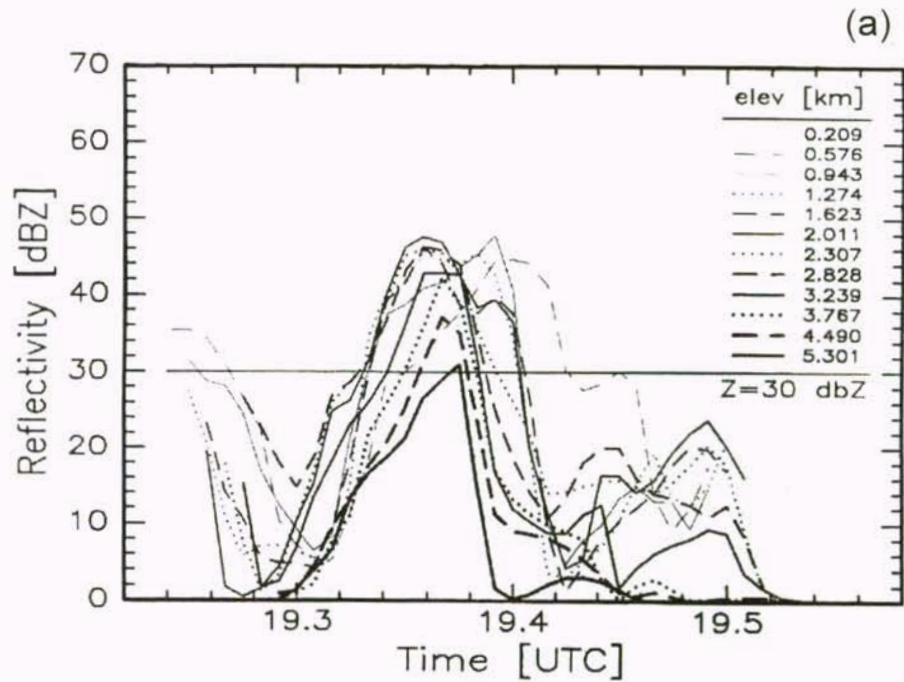


Figure 7-7. Interpolated reflectivity as a function of time above gauge array for complete volume scan. $\vec{r} = \{1.0, 1.0\}$ km, $\vec{u} = \{32, 30\}$ km/h, and $\Delta t = 30$ s; (a) calculated for local gauge point $\vec{r}^- = \vec{r} - \frac{1}{2}\vec{u}\Delta t$, (b) local gauge point $\vec{r}^+ = \vec{r} + \frac{1}{2}\vec{u}\Delta t$.

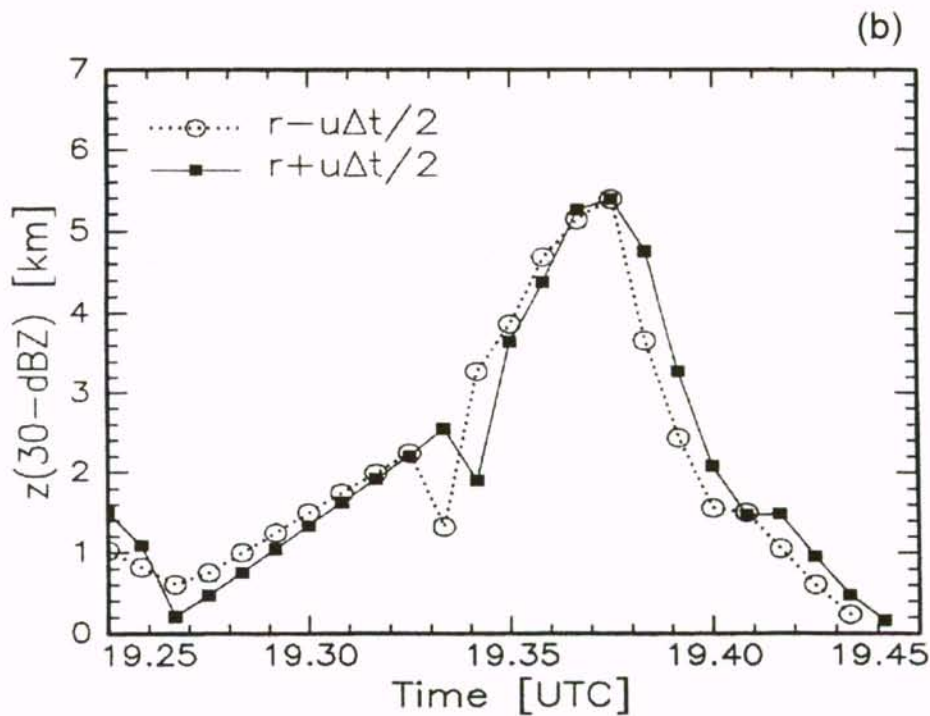
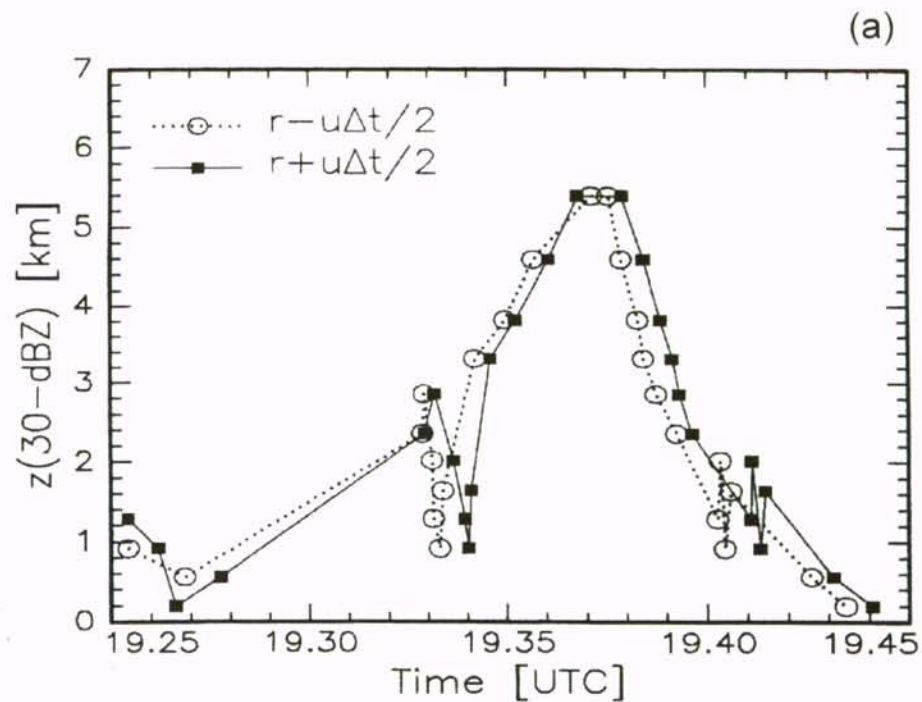


Figure 7- 8. (a) Height of 30 dBZ level as a function of time for \vec{r}^- and \vec{r}^+ , from Equation (7.22), at corresponding local gauge point $\vec{r} = \{1.0, 1.0\}$ km, (b) re-sampled and smoothed height, filling in missing points.

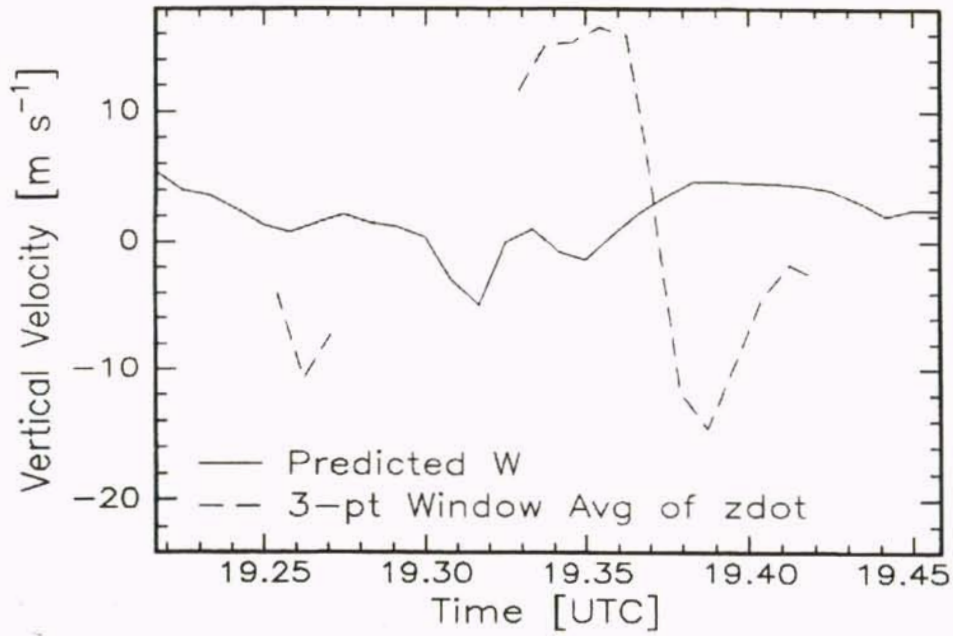


Figure 7-9. Vertical velocity of 30 dBz level above local gauge point $\vec{r} = \{1.0, 1.0\}$ km, using Equation (7.23) and data from Figure 7-8b.

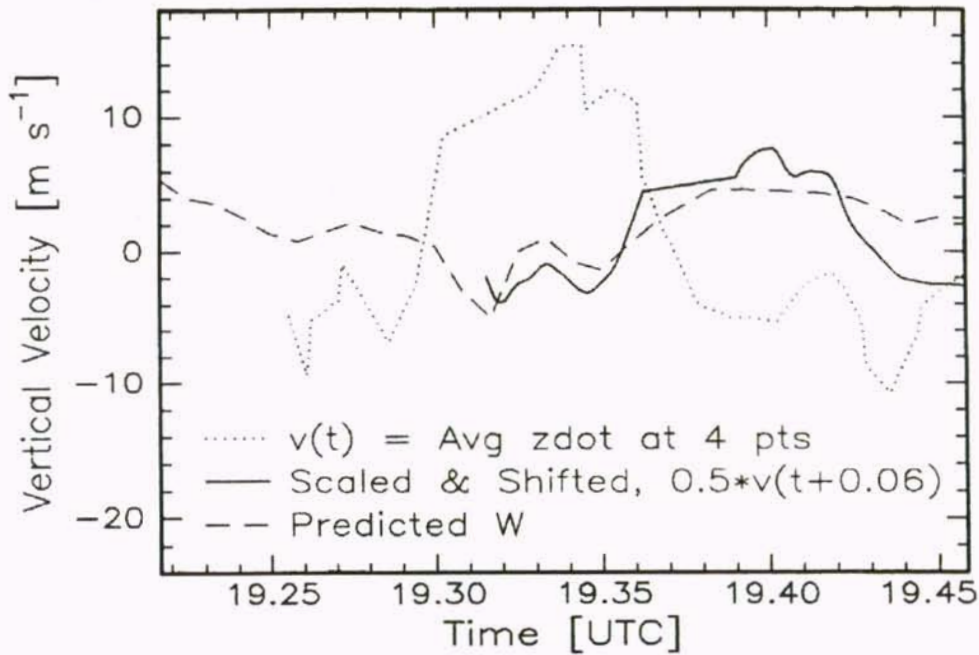


Figure 7-10. Dotted line is average vertical velocity of 30 dBZ level above gauge site; solid line is average velocity shifted by 0.06 h and scaled by 0.5; and dashed line is extracted predicted updraft/downdraft velocity W from Figure 7-6.

CHAPTER 8

CONCLUSIONS

Contributions from this dissertation work are summarized in the following sections, and suggestions for future research are proposed.

8.1 Summary of Contributions

Conventional image and digital signal processing algorithms have been selected, combined, and appropriately modified in order to produce a novel set of numerical techniques useful for solving problems belonging to the fields of radar meteorology, hydrology, and atmospheric science. The specific problems addressed in this research are that of rainfall estimation from rain gauge and weather surveillance radar, and in particular, correlation and interpolation over microscale regions (areas on the order of tens of square kilometers or less). In all cases considered, a prototype algorithm was developed and subsequently tested using data from local rain gauge networks (TRMM/KSC and UCF/ARGA) collocated with Melbourne NWS radar data. In summary, I believe the following contributions have been made:

1. In Section 4.2.4, a rain gauge interpolation algorithm, based on an advection transformation and the gravity formula, was proposed and developed. Several sets of interpolated rain gauge data were compared to collocated interpolated radar data using a time sequence of rainfall measurements and an RMS measure of correlation. In this way, rain gauge data is essentially transformed to a spatial average, similar to the areal average of weather radar measurements. This method of interpolating microscale rain

gauge clusters, or extrapolation of single gauges, shows promise of reducing radar-gauge correlation error, leading directly to the possibility of improved calibration of radar rainfall estimation algorithms. Other benefits of this contribution from Chapter 4 are in rainfall mapping for hydrology applications, where large errors, typically induced by the convective and advective nature of thunderstorms, may be significantly reduced. The result may be enhanced estimates of short-time rainfall accumulations for agriculture, forestry, and river flood warnings.

2. In Section 5.3, adaptive digital signal processing methods were combined with conventional gradient search optimization techniques to develop an algorithm for calibration of impact disdrometers. Real-time and off-line versions were considered, both of which utilize a conventional tipping bucket rain gauge as a reference or "training" signal. The advantages of such a calibration method are improved disdrometer estimates of rainfall rate as a function of time, as well the possibility of eliminating (or at least reducing) the laborious single drop calibration procedure, periodically required in order to safeguard reliable disdrometer operation. The method of Chapter 5 uses naturally occurring rainfall to maintain a constant calibration of the disdrometer, resulting in an "in situ" calibration algorithm.
3. In Section 5.4, an impulse suppression algorithm, previously developed at UCF for the suppression of scratch noise from damaged phonograph records, was modified and applied to the problem of disdrometer data corruption caused by environmental noise. The gated median filter algorithm was used to pre-process the input to the UCF/ARGA acoustic disdrometer. Instead of suppressing the impulses, as in previous applications, the filtered signal was subtracted from the original data, resulting in a processed signal where all data except the impulses are removed. This results in alleviation of the damaging effects of thunder and wind noise on disdrometer measurements.

4. A convolution model of rainfall based on spatial and temporal convolution and atmospheric advection was developed and presented in Chapter 6. The primary goal of this simulation model was to study the effects of advection and gravitational sorting on basic drop dynamics. Simulation results yield some interesting insight into the nature and variation of the Z - R relationship under conditions of advection and large transient conditions of rainfall rate. Based on several simulations of the convolution rainfall model presented in Chapter 6, some very surprising results are seen in the Z - R relationships. Not only does the simulation support the conjecture that the Z - R power-law parameters may vary by significant amounts (over a microscale region), a distinct split in the behavior of the Z - R linear regression fit can be seen, proportional to advection magnitude. This split corresponds to the advective approach and recession of the developing storm cell. Preliminary data analysis suggests that data properly processed (using vigorous statistical methodologies) should at least partially corroborate some of these unanticipated simulation results.

5. In Chapter 7, a DSD model was developed which accounts for the modification of the drop size distribution due to the segregation of drops from vertical wind velocities (updrafts and downdrafts). Making use of the rain gauge spatial interpolation and averaging methods of Chapter 4, careful comparisons were made between radar and gauge averages over a microscale gauge cluster area. From this set of correlated data, a predicted average vertical velocity was extracted. This predicted vertical velocity can then be compared to other vertical profile data such as the movement of echo tops as measured by a NEXRAD volume scan or a radar profiler.

8.2 Suggestions for Future Research

Due to the variety of topics investigated in this work, more questions have been produced than have been answered. For this reason, the possible directions for future research are numerous, some of which will be suggested as follows:

1. The rain gauge spatial interpolation and averaging procedures investigated in Chapter 4 focused on rain gauge clusters at microscale separations, since that would be the ideal configuration for this algorithm. The interpolation algorithm has also been casually tried on single gauge sites, in which case it is actually an extrapolation process. Since nearly all existing gauge sites world-wide are not clustered within microscale separations, the single gauge variation of the algorithm could very well be more significant in its usefulness. This could have the same basic set of benefits as the gauge clustering scheme, but would certainly be more useful. This topic is undoubtedly something to pursue for future research.
2. Recent work on the disdrometer calibration algorithm of Chapter 5 indicates that some amount of single drop calibration data is needed in order to resolve ambiguities in the RMS error surface. Work needs to be performed to determine the extent of single drop calibration needed. For example, is one single, large drop in conjunction with the in situ calibration the best compromise? Alternatively, a complete single drop calibration in collaboration with the in situ calibration may yield the best results. Investigating this question is a good candidate for future work.
3. The impulse suppression algorithm based on the median filter could be evaluated with other disdrometer types in addition to the UCF acoustic (microphone) disdrometer. For example, the Joss disdrometer uses an electro-magnetic transducer for converting drop collisions to equivalent electrical impulses. The APL disdrometer uses piezoelectric ceramic for its mechanical to electrical conversion. It would be

interesting to adjust the median filter parameters (window length, gating threshold, etc.) of Chapter 5 for each of these transducer types and compare the corresponding noise suppression performance as a topic of future research.

4. The rainfall convolution model proposed in Chapter 6 suggests some very interesting results for microscale Z - R relations. The model itself should be closely examined and verified. The predictions made by the model should be carefully compared to experimental data which has been specifically designed to reproduce the simulation conditions. Incorporation of this UCF rainfall model with the National Center for Atmospheric Research (NCAR) rain-shaft model has been discussed. These topics could be very useful and interesting subjects of future research.
5. The vertical velocity predictions of the Z - R model described in Chapter 7 has been compared to NEXRAD volume scan data and echo top evolution. More of these kind of comparisons should be done. Also, and possibly more importantly, the model vertical velocity predictions should be compared to radar profiler data, such as that planned for the TRMM TEFLUN-B campaign from August to September, 1998, west of Melbourne. This too would be a useful and worthwhile direction to follow for future research.

9. REFERENCES

- [1] W. H. Press, B. P. Flannery, S. A. Teukolsky, and W. T. Vetterling, *Numerical Recipes - The Art of Scientific Computing*, Cambridge Press, pp. 274-334, 1989.
- [2] B. Widrow and S. D. Sterns, *Adaptive Signal Processing*, Prentice Hall, Englewood Cliffs, NJ, 1985.
- [3] A. R. Weeks, T. Kasparis, and J. E. Lane, "Image Enhancement Using Linear and Non-Linear Spatial Filtering Techniques", *DSP Applications*, Vol. 2, No. 11, pp. 35-44, November 1993.
- [4] G. D. Hillman and J. E. Lane, "Real-Time Determination of IIR Coefficients for Cascaded Butterworth Filters", *International Conference on Acoustics, Speech, and Signal Processing*, Session D10.10, pp. 1353-1356, 1989.
- [5] J. Lane and G. Hillman, "Implementing IIR/FIR Filters with Motorola's DSP56000/DSP56001", *Motorola Application Note*, APR7/D Rev. 2, 1993.
- [6] F. Pratte, D. Ecoff, and J. VanAndel, "AP Ground Clutter in WSR-88D Base Data and Recommendations for Automatic AP Clutter Mitigation", ERL/FSL and NCAR/ATD, *FY96 Report to the NWS/OSF Engineering Branch*, 15 November 1996.
- [7] T. Kasparis, N. S. Tzannes, and Q. Chen, "Detail Preserving Adaptive Conditional Median Filters", *Journal of Electronic Imaging*, Vol. 1, No. 4, pp. 358-364, 1992.
- [8] T. Kasparis and J. Lane, "Adaptive Scratch Noise Filtering", *IEEE Transactions on Consumer Electronics*, Vol. 39, No. 4, pp. 917-922, November 1993.
- [9] D. A. Shepard, "A Two-Dimensional Interpolation Function for Irregularly-Spaced Data", *23th National Conference of the Association for Computing Machinery*, Brandon/Systems Press, Inc., Princeton, NJ, pp. 133-145, 1968.

- [10] J. Joss and A. Waldvogel, "Ein Spektograph für Niederschlagstopfen mit Automatischer Auswertung", *Pure and Applied Geophysics*, Vol. 68, pp. 240-246, 1967.
- [11] J. R. Rowland, "Comparison of Two Different Raindrop Disdrometers", *17th Radar Meteorology Conference*, American Meteorological Society, Seattle, pp. 398-405, October, 1976.
- [12] J. Lane, T. Kasparis, and G. McFarquhar, "Acoustic Rain Gauge Array Experiment: Phase I", *ERIM 4th International Conference on Remote Sensing for Marine and Coastal Environments*, Orlando, FL, pp. II-311 - II-320, 17-19 March 1997.
- [13] M. Schönhuber, H. E. Urban, J. P. V. Póiares Baptista, W. L. Randeu, and M. Riedler, "Weather Radar Versus 2D-Video-Distrometer Data", *Weather Radar Technology for Water Resources Management*, B. Braga, Jr. and O. Massambani, IRTCUD and IHP-UNESCO, San Paulo, Brazil, Chap. I, Sec. 10, 1997.
- [14] M. Steiner, R. A. Houze Jr., and S. E. Yuter, "Climatological Characterization of Three-Dimensional Storm Structure from Operational Radar and Rain Gauge Data", *Journal of Applied Meteorology*, Vol. 34, pp. 1978-2007, 1995.
- [15] R. J. Doviak and D. S. Zrnic, *Doppler Radar and Weather Observations*, Academic Press, p. 21, 1993.
- [16] J. S. Marshall and W. M. Palmer, "The Distribution of Raindrops With Size", *Journal of Meteorology*, Vol. 9, pp. 327-332, 1948.
- [17] C. W. Ulbrich, "Natural Variations In the Analytical Form of the Raindrop-Size Distribution", *Journal of Climate and Applied Meteorology*, Vol. 22, pp. 1764-1775, 1983.
- [18] J. O. Laws, "Measurements of the Fall-Velocity Of Water-Drops and Raindrops", *Transactions of the American Geophysical Union*, Vol. 22, pp. 709-721, 1941.
- [19] E. K. Edgerton and J. R. Killian, *Flash: Seeing the Unseen by Ultra High Speed Photography*, Hale Publishing Co., 1939.

- [20] H. R. Pruppacher and K. V. Beard, "A Wind Tunnel Investigation of the Internal Circulation and Shape of Water Drops Falling at Terminal Velocity In Air", *Quarterly Journal of the Royal Meteorological Society*, Vol. 96, pp. 247-256, 1970.
- [21] R. Gunn and G. D. Kinzer, "The Terminal Velocity of Fall for Water Droplets In Stagnant Air", *Journal of Applied Meteorology*, Vol. 6, pp. 243-248, 1948.
- [22] A. C. Best, "Empirical Formula for the Terminal Velocity of Water Drops Falling Through the Atmosphere", *Quarterly Journal of the Royal Meteorological Society*, Vol. 75, pp. 302-311, 1950.
- [23] D. Atlas, R. C. Srivastava, and R. S. Sekhon, "Doppler Radar Characteristics of Precipitation at Vertical Incidence", *Review of Geophysics and Space Physics*, Vol. 2, pp. 1-35, 1973.
- [24] D. Atlas, D. Rosenfeld, and A. R. Jameson, "Evolution of Radar Rainfall Measurements: Steps and Mis-Steps", *Weather Radar Technology for Water Resources Management*, B. Braga, Jr. and O. Massambani, IRTCUD and IHP-UNESCO, San Paulo, Brazil, Chap. I, Sec. 1, 1997.
- [25] D. S. Zrnich and A. V. Ryzhkov, "Polarimetric Measurements of Rain", *Weather Radar Technology for Water Resources Management*, B. Braga, Jr. and O. Massambani, IRTCUD and IHP-UNESCO, San Paulo, Brazil, Chap. I, Sec. 3, 1997.
- [26] W. Krajewski, "Rainfall Estimation Using Weather Radar and Ground Stations", *Weather Radar Technology for Water Resources Management*, B. Braga, Jr. and O. Massambani, IRTCUD and IHP-UNESCO, San Paulo, Brazil, Chap. I, Sec. 4, 1997.
- [27] R. A. Houze, "Observed Structure of Mesoscale Convective Systems and Implications for Large Scale Heating", *Quarterly Journal of the Royal Meteorological Society*, Vol. 115, pp. 425-461, 1989.

- [28] G. J. Ciach, W. F. Krajewski, E. N. Anagnostou, M. L. Baeck, J. A. Smith, J. R. McCollum, and A. Kruger, "Radar Rainfall Estimation for Ground Validation Studies of the Tropical Rainfall Measurement Mission", *Journal of Applied Meteorology*, Vol. 36, No. 6, pp. 735-747, June 1997.
- [29] P. Glitto and Lt. B. Choy., "A Comparison of WSR-88D Storm Total Precipitation Performance during Two Tropical Systems following Changes to the Multiplicative Bias and Upper Reflectivity Threshold", *Weather and Forecasting*, Vol. 12, No. 3, Part 1, pp. 459-471, September 1997.
- [30] W. L. Crosson, C. E. Duchon, R. Raghavan, and S. J. Goodman, "Assessment of Rainfall Estimates Using a Standard Z-R Relationship and the Probability Matching Method Applied to Composite Radar Data in Central Florida", *Journal of Applied Meteorology*, Vol. 35, No. 8, pp. 1203-1219, August 1996.
- [31] D. Rosenfeld and E. Amitai, "The Window Probability Matching Method for Rainfall Measurements with Radar", *Journal of Applied Meteorology*, Vol. 33, pp. 682-693, 1994.
- [32] J. Joss and A. Waldvogel, "Comments on 'Some Observation on the Joss-Waldvogel Rainfall Disdrometer'", *Journal of Applied Meteorology*, Vol. 16, pp. 112-113, January 1976.
- [33] R. List and G. M. McFarquhar, "The Evolution of Three-Peak Raindrop Size Distributions In One-Dimensional Shaft Models. Part I: Single-Pulse Rain", *Journal of the Atmospheric Sciences*, Vol. 47, No. 24, pp. 2996-3006, 1990.
- [34] G. M. McFarquhar and R. List, "The Evolution of Three-Peak Raindrop Size Distribution In One-Dimensional Shaft Models. Part II: Multiple Pulse Rain", *Journal of the Atmospheric Sciences*, Vol. 48, No. 13, pp. 1587-1595, 1991.
- [35] G. M. McFarquhar and R. List, "The effect of curve fits for the disdrometer calibration on raindrop spectra, rainfall rate, and radar reflectivity", *Journal of Applied Meteorology*, Vol. 32, No. 4, pp. 774-782, 1993.

- [36] J. A. Nystuen, et. al., "APL Disdrometer Evaluation", *NOAA Technical Memorandum ERL*, No. AOML-83, Atlantic Oceanographic and Meteorological Laboratory, Miami, FL, 1994.
- [37] J. Lane, T. Kasparis, and G. McFarquhar, "Adaptive DSP algorithm for calibrating drop size distribution rain gauges." In *SPIE AeroSense, 11th International Conference*, Orlando, FL, June 1997.
- [38] P. I. A. Kinnell, "Some Observations on the Joss-Waldvogel Rainfall Disdrometer", *Journal of Applied Meteorology*, Vol. 15, pp. 499-502, 1976.
- [39] G. M. McFarquhar, "Flux Measurements of Pulsating Rain With a Disdrometer and Doppler Radar During Phase II of the Joint Tropical Rain Experiment In Malaysia", *Journal of Applied Meteorology*, Vol. 35, No. 6, pp. 859-874, June 1996.
- [40] D. Atlas, P. Willis, and F. Marks, "The Effects of Convective Updrafts and Downdrafts on Reflectivity-Rain Rate Relations and Water Budgets", *27th Conference on Radar Meteorology*, Vail, CO, pp. 19-22, 9-13 October 1995.
- [41] E. Nakakita, S. Ikebuchi, K. Nakagawa, T. Sato, B. E. Vieux, and T. Takasao, "Utilization of Vertical Profile of DSD into Building up an Algorithm for Estimating Ground Rainfall Amount Using Radar", *Weather Radar Technology for Water Resources Management*, B. Braga, Jr. and O. Massambani, IRTCUD and IHP-UNESCO, San Paulo, Brazil, II-20, 1997.
- [42] J. Lane, T. Kasparis, L. Jones, P. Glitto, D. Sharp, F. Merceret, G. McFarquhar, and B. Fisher, "Steps Towards Improved Estimates of Convective Rainfall Using Spatial Averages Obtained from Rain Gauge Clusters", *ERIM 1st International Conference Geospatial Information in Agriculture and Forestry*, Lake Buena Vista, FL, 1-3 June 1998.

